STRUCTURAL AND MECHANICAL CHARACTERIZATION OF SCALE-UP $FeCoCrNi$, $FeCoCrNiCu_x$, AND $FeCoCrNiAl_x$ HIGH ENTROPY ALLOYS (HEAs)

A THESIS SUBMITTED TO
THE GRADUATE SCHOOL OF NATURAL AND APPLIED SCIENCES
OF
MIDDLE EAST TECHNICAL UNIVERSITY

BY

ZİYA ANIL ERDAL

IN PARTIAL FULFILLMENT OF THE REQUIREMENTS
FOR
THE DEGREE OF MASTER OF SCIENCE
IN
METALLURGICAL AND MATERIALS ENGINEERING

JANUARY 2020

Approval of the thesis:

STRUCTURAL AND MECHANICAL CHARACTERIZATION OF SCALE-UP FeCoCrNi, FeCoCrNiCu$_x$, AND FeCoCrNiAl$_x$ HIGH ENTROPY ALLOYS (HEAs)

submitted by **ZİYA ANIL ERDAL** in partial fulfillment of the requirements for the degree of **Master of ScienceMaster of Science** i**n Metalurgical and Materials EngineeringMetalurgical and Materials Engineering, Middle East Technical University** by,

Prof. Dr. Halil Kalıpçılar
Dean, Graduate School of **Natural and Applied Sciences** _____

Prof. Dr. Cemil Hakan Gür
Head of the Department, **Metallurgical and Materials Eng.** _____

Assoc. Prof. Dr. Yunus Eren Kalay
Supervisor, **Metallurgical and Materials Eng. Dept., METU** _____

Examining Committee Members:

Prof. Dr. Rıza Gürbüz
Metallurgical and Materials Eng., METU _____

Assoc. Prof. Dr. Yunus Eren Kalay
Metallurgical and Materials Eng., METU _____

Prof. Dr. Cemil Hakan Gür
Metallurgical and Materials Eng., METU _____

Assist. Prof. Dr. Sezer Özerinç
Mechanical Engineering Dept., METU _____

Assoc. Prof. Dr. Yiğit Karpat
Industrial Engineering Dept., Bilkent University _____

Date: 31.01.2020

I hereby declare that all information in this document has been obtained and presented in accordance with academic rules and ethical conduct. I also declare that, as required by these rules and conduct, I have fully cited and referenced all material and results that are not original to this work.

Name, Last name : Ziya Anıl Erdal

Signature :

ABSTRACT

STRUCTURAL AND MECHANICAL CHARACTERIZATION OF SCALE-UP FeCoCrNi, $FeCoCrNiCu_x$, AND $FeCoCrNiAl_x$ HIGH ENTROPY ALLOYS (HEAs)

Erdal, Ziya Anıl
Master of Science, Metalurgical and Materials Engineering
Supervisor: Assoc. Prof. Dr. Yunus Eren Kalay

January 2020, 99 pages

High entropy alloys (HEAs) have recently attracted much attention due to their unique properties such as high ambient and elevated temperature strengths, hardness, and good structural stability. FeCoCrNi is one of the well-known alloy system with its excellent HEA forming ability. This alloy was previously produced by various methods using high grade pure raw materials. However, there is no scale-up production from industrial raw materials which contain various impurity elements such as Al, Si, and C. In this study, FeCoCrNi, $FeCoCrNiCu_x$, and $FeCoCrNiAl_x$ (x: 0.3, 0.6, 1) HEAs were produced from industrial grade raw materials with impurities using induction casting method. These alloys were produced by using of high purity raw materials to compare microstructural features and mechanical properties, as well. These alloys were modelled through Vienna Ab initio Simulation Package (VASP). Structural characterization were performed with X-ray diffraction (XRD), scanning electron microscopy (SEM) and transmission electron microscopy (TEM). The thermodynamic properties of these alloys were investigated by HEA Calculator and Thermo-Calc software. Hardness, tensile and compression tests were performed to reveal basic mechanical behavior. Cr_7C_3 phases were present in impure FeCoCrNi alloy besides FCC main phase, on the other hand the pure specimen had only FCC

phase. 515 MPa tensile strength with 57 % ductility and 650 MPa tensile strength with no ductility were obtained for pure and impure FeCoCrNi alloys, respectively. The addition of Cu does not cause a significant structural and mechanical difference in HEAs. However, the addition of Al caused the crystal structure to transform from FCC to BCC. Impure $FeCoCrNiAl_{0.6}$ alloy which has 2770 MPa maximum compressive strength with 14% compressive strain at fracture is the strongest one among produced alloys. It also shows better mechanical properties compared to Mg, Al, Ti and most of the Fe, Ni containing alloys.

Keywords: High Entropy Alloys, Scale-Up, Structural and Mechanical Characterization

ÖZ

BÜYÜK ÖLÇEKLİ FeCoCrNi, $FeCoCrNiCu_x$ ve $FeCoCrNiAl_x$ YÜKSEK ENTROPİLİ ALAŞIMLARIN (YEA'LARIN) YAPISAL VE MEKANİK KARAKTERİZASYONU

Erdal, Ziya Anıl
Yüksek Lisans, Metalurji ve Malzeme Mühendisliği
Tez Yöneticisi: Doç. Dr. Yunus Eren Kalay

Ocak 2020, 99 sayfa

Son zamanlarda, yüksek entropi alaşımlar (YEA'lar) ortam ve yüksek sıcaklıklarda yüksek mukavemet, sertlik ve yüksek yapısal kararlılık gibi özgün özelliklerinden dolayı dikkat çekmektedirler. FeCoCrNi mükemmel YEA kabiliyeti ile en yaygın bilinen alaşımdır. Bu alaşım, yüksek saflıktaki elementler kullanılarak çeşitli yöntemlerle üretilmektedirler. Ancak, saf olmayan ve Al, Si ve C gibi katışkı elementleri içeren endüstriyel hammaddeler kullanılarak ölçeği büyütülmüş üretim bulunmamaktadır. Bu çalışmada FeCoCrNi, $FeCoCrNiCu_x$ ve $FeCoCrNiAl_x$ (x : 0.3, 0.6, 1) YEA'ları indüksiyon döküm yöntemi ile saf olmayan elementler kullanılarak üretildi. Aynı zamanda, bu alaşımların içyapılarının ve mekanik özelliklerinin karşılaştırılması için yüksek saflıkta elementler kullanılarak da üretildi. Bu alaşımlar üretilmeden önce Vienna Ab initio Simulation Package (VASP) programı kullanılarak modellendi Alaşımların yapısal karakterizasyonları X-ışını kırınımı (XRD), taramalı elektron mikroskobu ve geçirimli elektron mikroskobu ile incelenmiştir. Bu alaşımların termodinamik özellikleri HEA Calculator ve Thermo-Calc programları kullanılarak incelenmiştir. Mekanik karakterizasyon için ise çekme, sertlik ve basma testleri uygulanmıştır. Saf FeCoCrNi alaşımı sadece yüzey

merkezli kristal (YMK) yapısına sahip iken, saf olmayan FeCoCrNi alaşımı ise YMK yapısına ek olarak Cr_7C_3 fazını da içerdiği gözlemlenmiştir. Saf FeCoCrNi ve saf olmayan FeCoCrNi alaşımlarının çekme testi sonuçlarına göre, saf olan alaşım 515 MPa gerilme dayanımına ve % 57 sünekliğe sahip iken, saf olmayan alaşımın 650 MPa gerilme dayanımına ulaştığı ancak alaşımın sünekliğini kaybettiği belirlenmiştir. Alaşıma Cu eklenmesi YEA'larda önemli bir yapısal ve mekanik değişikliğe neden olmadığı görülmüştür. Ancak, alaşıma Al ilavesi ise kristal yapının yüzey merkezden hacim merkeze doğru dönüşmesine neden olmuştur. % 14 basma gerinimi ile 2770 MPa maksimum basma mukavemetine sahip olan saf olmayan $FeCoCrNiAl_{0.6}$ alaşımının üretilen alaşımlar arasında en yüksek mukavemete sahip olmakla birlikte Mg, Al, Ti alaşımlarına ve birçok Fe, Ni elementleri içeren alaşımlara göre daha iyi mekanik özellik göstermektedir.

Anahtar Kelimeler: Yüksek Entropi Alaşımlar, Ölçek Büyütme, Yapısal ve Mekanik Karakterizasyon

To My Precious Family

ACKNOWLEDGMENTS

Firstly, I would like to thank to my advisor Assoc. Prof. Dr. Y. Eren Kalay for his suggestion and encouragement during my undergraduate and graduate study. He always supported me and helped me with everything. I will always be grateful to him for learning me in academic field. I also would like to thank him for helping and guiding me during my job search.

I would like to thank my my previous and current laboratory mates for their patience and great support; Fatih Sıkan, Bengisu Yaşar, Ayşe Merve Genç Ünalan, Özgün Acar, Koray İroç, Doğuhan Sarıtürk, Emel Erdal, Tolgahan Ulucan, Can Okuyucu and especially Gökhan Polat who is determined and disciplined person I have seen so far. I am very grateful to him for helping me with everything.

I would like to thank the employees of the laboratories in Metallurgical and Materials Engineering. I am especially grateful to Cemal Yanardağ and Arif Atalay Özdemir, who helped in the preparation of the specimens, Önder Şahin and Hüseyin Ceylan, who assisted in the experiments. I would like to thank Serkan Yılmaz for his help during TEM study.

I would like to owe to Berk Aytuna, İbrahim Aydın, Elif Yeşilay, Pelin Gündoğmuş and Seren Özer for their sincere friendship. I also would like to thank Burak Aldoğan, Esra Sütçü and Eda Aysal. I am especially grateful to Alper Çiçek, Arda Alan, Semih Küçükyılmaz and Ozan Acar who are my childhood friends for their support and encouragement.

Finally, I would like to dedicate this study to my family, Muharrem, Vahide and Tuğba Erdal. I will be grateful to my parents for their appreciation, encouragement and love throughout my life.

TABLE OF CONTENTS

LIST OF TABLES

TABLES

LIST OF FIGURES

FIGURES

LIST OF ABBREVIATIONS

ABBREVIATIONS

HEA: High Entropy Alloy

MEA: Medium Entropy Alloy

VEC: Valance Electron Concentration

DFT: Density Functional Theory

GGA: Generalized Gradient Approach

AIMD: Ab-initio Molecular Dynamics

GPa: Giga Pascal

MPa: Mega Pascal

FCC: Face Centered Cubic

BCC: Body Centered Cubic

HCP: Hexagonal Close Packed

HV: Vickers Hardness

XRD: X-ray Diffraction

SEM: Scanning Electron Microscopy

TEM: Transmission Electron Microscopy

AM: Additive Manufacturing

SLM: Selective Laser Melting

CCA: Complex Concentrated Alloy

LIST OF SYMBOLS

SYMBOLS

Å: Angstrom

°C: Degree Celsius

K: Kelvin

Sconf: Configurational Entropy

ΔSmix: Entropy of Mixing

ΔHmix: Enthalpy of Mixing

ΔGmix: Gibbs Free Energy of Mixing

δ: Atomic Size Difference

CHAPTER 1

INTRODUCTION

Recent improvements in engineering, particularly in the aerospace industry, require robust materials with superior properties as compared to traditional engineering materials. These properties can be thought as magnetic, microstructural and mechanical properties and chemical stability. It is very difficult to provide more than one of these properties together in conventional alloy concept. Therefore, studies have recently focused on high entropy alloys (HEAs) which are based on five or more principal elements containing concentrations between 5 and 35 at. %, with the formation of solid solution phases [1]. In fact, this contradicts to well-known Gibbs phase rule. According to this rule, tendency of intermediate phases increases with increasing the number constituents. The reason why these alloys do not comply with the rule is that the resultant mixing entropy is higher than that of conventional alloys. Therefore, this is one of the most important reasons why HEA concept attracts more attention in material research studies. Another reason is that the number of elements in HEAs can be increased and the possibility of changing the atomic proportions of the alloying elements in a wide range allows the availability of countless alloy combinations. As a result, it becomes possible to discover new materials with desired properties. Mechanical properties are generally the most remarkable property among the newly discovered materials. Special alloys such as Ni-based, Co-based and Ti-based are used in applications requiring high strength at room temperature and high temperatures from past to present. However, the production and material cost of such alloys are substantially high. Therefore, the studies are focused on these alloys more and more as the high-strength alloys with cost-effective production techniques are developed. The alloy system first described as HEA is equiatomic FeCoCrNi alloy

[1]. In literature, when this alloy is produced by casting method, FCC solid solution is obtained. In terms of mechanical properties, this alloy has extremely high ductility value on the order of 68% whereas, very low yield strength of 165 MPa and a tensile strength of 400 MPa [2]. Powder metallurgy has been applied to FeCoCrNi alloy system and a yield strength of 359 MPa and tension strength of 712.5 MPa with 56% elongation were measured [3]. This looks significantly better as compared to conventional casting. However, one of the drawbacks of P/M method is the price of the powders since the quality of the powders is directly related to powder processing costs. which include the cost of elemental raw materials and atomization costs. The number of studies on improving the mechanical properties of HEAs by adding different elements to the main FeCoCrNi alloy have been increasing day by day. In the literature, the addition of Al into the main alloy leads to a significant increase in the hardness of the alloy [4]. In another study, Addition of Ti into FeCorCrNiAl alloy in certain proportions enables the yield strength of the alloy to increase up to 2.26 GPa under compression load [5]. As mentioned above, these alloys are produced by various methods from high grade pure raw materials. However, there is no scale-up production from industrial raw materials which contain various impurity elements such as Al, Si and C. Structural, microstructural and mechanical effects of these impurities in HEAs haven't been studied so far. In addition, the use of industrial raw materials is a matter of critical consideration in terms of production cost of HEAs.

The aim of this thesis is to investigate the structural and mechanical properties of FeCoCrNi, $FeCoCrNiCu_x$, and $FeCoCrNiAl_x$ (x: 0.3, 0.6, 1) alloys produced from impure elements and compare with the ones produced from pure elements. In this context, thesis consists of five chapters. In the first chapter, brief introduction of the main aspects of HEAs is mentioned. The second chapter includes the literature review. In the third chapter, the computational methods used to find out the crystal structures and thermodynamic values of the alloys before production step, the production methods of the alloy, the structural and mechanical devices, the test parameters used for the structural and mechanical investigation of the produced

impure and pure alloys are mentioned. Vienna Ab initio Simulation Package (VASP) program for atomic simulations, Thermo-Calc program for the determination of melting temperatures of the alloys required for VASP, and thermodynamic parameters are used. X-ray diffraction (XRD), scanning electron microscopy (SEM) and transmission electron microscopy (TEM) were used for structural characterization of produced alloys. Hardness, tension and compression tests were applied for mechanical characterization. The fourth chapter includes the results, discussions on them and comparison of the raw material costs of pure and impure alloys. The fifth chapter includes conclusion of main points and future recommendations.

CHAPTER 2

LITERATURE REVIEW

2.1 High Entropy Alloys (HEAs)

Designing new structural materials with superior properties has been always had a critical importance in engineering. The alloy design of the used materials depends conventionally on one main element with small amount of alloying elements added to improve the properties such as microstructural, mechanical or thermal and processability of the material. In order to achieve high specific strength and thermal resistance, Ti-Al, Ni-Al, and Fe-Al binary systems that contain intermetallic compounds have drawn much attention in the 1970s [6]. However, brittleness and processing problems have limited the application areas. Technological developments have led to the emergence of different production techniques such as rapid solidification and mechanical alloying [17]. Alloys obtained using these methods have fine microstructure with very high strength. Bulk metallic glasses such as Pd-, Zr-, Fe- or Mg- based alloys have become popular in the last two decades due to their extremely high mechanical properties. Although bulk metallic glasses have high mechanical strength their ductility is very poor and thermal stability is weak above above 673 K [8-14].

As opposed to above mentioned materials, high entropy alloys (HEAs), which contain more than one principal element, have revealed the discovery of the wide range composition about 12 years ago [15]. According to the Gibbs phase rule [16], when the number of main element in an alloy system is increased, the formation of intermetallic compounds and complicated microstructures, which could cause brittleness and processing problems, may occur. However, HEAs proposed by Yeh

et al. [1,17] are based on five or more principal elements that have the concentrations between 5 and 35 at% can be obtained without the formation of intermetallic phases. Simple solid solution phases are easily obtained due to higher mixing entropies of their liquid or random solid solution compared to binary or ternary alloy systems [18]; in other words, solid solutions have usually higher entropy compared to intermetallics that are suppressed during solidification. Consequently, HEAs having solid solution phases have been studied intensely for structural or mechanical applications due to their promising properties.

2.2 History of HEAs

First study for multi-principal element alloys (MPEAs) has been introduced as an undergraduate thesis in the late 1970s [19]. After that, another undergraduate thesis entitled ‘‘A study on multicomponent alloy systems containing equal-mole elements’’ was proposed by Huang et. al. in 1996 [17]. According to this study, 40 equiatomic alloys based on Ti, V, Cr, Fe, Co, Ni, Cu, Mo, Zr, Pd, and Al were produced by arc melting. The effect of B addition has been investigated in terms of microstructure, hardness and corrosion resistance of as-cast and annealed condition. Dendritic microstructure was obtained in the as-cast condition. Hardness of the alloys changed from 590 to 890 HV in accordance with as-cast or annealed condition. %3 addition of B into the alloys has increased the hardness. The first results of multi-principal element alloys (MPEAs) entitled “Microstructural development in equiatomic multicomponent alloys’’ were published in an article by Cantor in 2004 [19]. The results indicated that a five component $Fe_{20}Cr_{20}Mn_{20}Ni_{20}Co_{20}$ alloy was produced by melt spinning method that enables extremely high cooling rates on the order of 10^6 K/s. A single FCC solid solution, which has dendritic microstructure was obtained. Different elements such as Cu, Ti, Nb, V, W, Mo, and Ta were added into the main alloy within a range of six to nine elements. All alloys possessed mainly FCC solid solution phase. However, another alloy including 16 elements with equiatomic ratio showed multiphase structures and brittle behaviour in as-cast

condition. In addition, the total number of phases was acquired below the maximum equilibrium number described by Gibbs phase rule for all produced alloys. However, entropy was not stated in these studies. The concept of high entropy was first mentioned by Yeh in a paper entitled "Nanostructured high-entropy alloys with multiprincipal elements—novel alloy design concepts and outcomes" in 2004 [1]. This study comprised both experimental results and high entropy (HEA) theory. Yeh stated that high mixing entropy affects significantly to decrease the number of phases in such alloys and improve the properties. $CuCoNiCrAl_xFe$ (x in molar ratio from 0 to 3.0) alloys were produced by arc-melting, and microstructural and mechanical characterizations were applied in the as-cast state. All alloys consisted of solid solution phases which are FCC and BCC without intermetallics. The reason for this situation was thought to be high mixing entropy that decreases the possibility of the formation of segregation or intermetallic compound. Since 2004, HEAs have become much more popular due to many unexplored research areas. HEAs have been recently studied intensely in terms of structural and functional properties.

2.3 Definitions of HEAs

HEAs are defined in terms of composition-based and entropy-based. According to composition-based definition, HEAs consist of five or more principal elements. Concentration of each of the principal elements should be in the range of 5 and 35 at.%. In addition, HEAs can include minor elements that should be below 5 at.% [18]. The number of HEAs is increased substantially because of determination of atomic ratios in a wide range. Minor elements are also used to improve the properties of HEAs. It can be concluded that composition based definition only introduce elemental concentration, and it does not give any information about the range of entropy values of the alloys. Therefore, entropy-based definition is described in order to explain much more comprehensive the concept of HEAs. High mixing entropy is directly related to stability of phases and to suppress the formation of intermetallic compounds at high temperatures in particular [18]. High mixing entropy of the alloy

should be identified as a value by means of statistical thermodynamic calculations. It is the fact that Gibbs free energy (G) of a system under isothermal and isobaric states should be minimized in order to attain equilibrium condition. Free energy of the system is calculated by:

$G = H - TS$ Equation 2.1

As shown from Equation 2.1, free energy of the system is directly related to the enthalpy (H) and entropy (S) of the system at a specified temperature. In order to find the equilibrium condition of an alloy system, free energy change should be determined from the elemental state to mixed states. Then, the lowest mixing free energy of the system ($\triangle G_{mix}$) can be calculated. When this situation is also considered for the enthalpy and entropy of the system, the differences in free energy ($\triangle G_{mix}$), enthalpy ($\triangle H_{mix}$) and entropy ($\triangle S_{mix}$) are calculated by:

$\triangle G_{mix} = \triangle H_{mix} - T\triangle S_{mix}$ Equation 2.2

In order to calculate configurational entropy (S_{conf}) of the system, Boltzmann's equation is used [20]:

$$\Delta S_{\text{conf}} = -k \ln w \quad \text{Equation 2.3}$$

where *k* is defined as Boltzmann's constant and *w* is the number of paths of mixing. In addition, it is known as a thermodynamic fact that (S_{conf}) of a binary alloy is calculated by:

$$\Delta S_{\text{conf}} = -R(x_A \ln x_A + x_B \ln x_B) \quad \text{Equation 2.4}$$

where R is the gas constant, 8.314 J/K.mol, x_A and x_B are the mole fraction of A and B elements Therefore, by using above equations, S_{conf} of the alloy that depends on the n elements and x_i mole fraction is:

$$\Delta S_{\text{conf}} = -R \sum_{i=1}^{N} x_i \ln x_i \quad \text{Equation 2.5}$$

When equiatomic alloy with liquid or regular solid solution condition is considered, S_{conf} per mole of the alloy is [1]:

$$\Delta S_{\text{conf}} = -k\ ln\ w = -R\left(\frac{1}{N} ln \frac{1}{N} + \frac{1}{N} ln \frac{1}{N} + \cdots .. + \frac{1}{N} ln \frac{1}{N}\right) = \text{RlnN Equation 2.6}$$

Where N is the number of elements.

Despite the fact that change of total entropy depends on four factors i.e. configurational, vibrational, magnetic dipole, and electronic randomness, S_{conf} affects total entropy much more as compared to other factors [1]. Figure 2.1 shows change in S_{conf} with respect to the number of elements for equiatomic alloys in the random solution state by means of equation 2.6. As an example for binary equimolar alloy, S_{conf} of the alloy is found as 5.76 J/K.mol. Another example for five element equimolar alloy, S_{conf} of that is calculated as 13.37 J/K.mol. Since mixing of ordered solid solutions is limited, S_{conf} of the solutions is smaller [21] .

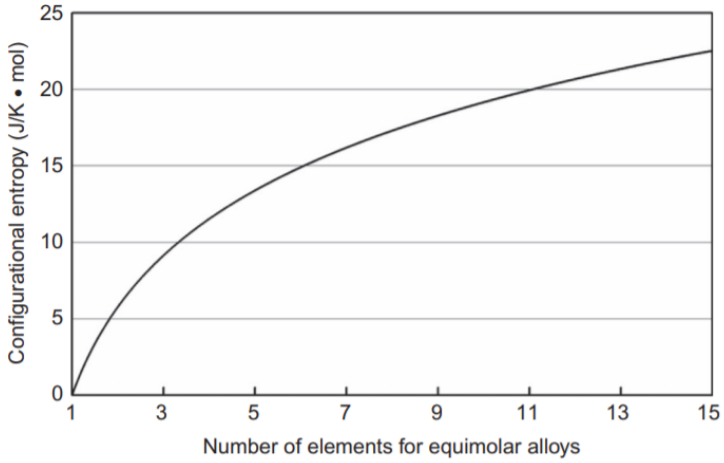

Figure 2. 1 Change in S_{conf} with respect to the number of elements for equiatomic alloys in the random solution state. Adopted from [21]

It is seen from Figure 2.1 that S_{conf} value of ternary equiatomic alloys is 1.1R which is relatively higher than larger than the entropy difference of the melting of a pure metal, R. When the number of component is increased to 5, S_{conf} value is found as 1.61R. NiAl and TiAl is are very stable intermetallic compounds and their configurational entropies are 1.38R and 2.06R, respectively [1]. Therefore, it is recommended and seen in figure 1.2 that ΔS_{conf} of 1.5R is high enough to supress the formation of the strong order atomic pairs, and they are called as high entropy alloys.

It is also seen from Figure 2.2 that if the configurational of the alloy is between R and 1.5R, they are called as medium entropy alloys (MEA) that contains 2 to 4 principal element. The last alloy group is low entropy alloys called as traditional alloys and they include 1 or 2 principal element. Their S_{conf} values are below R that is not enough to prevent the formation of compounds with high binding energy [22].

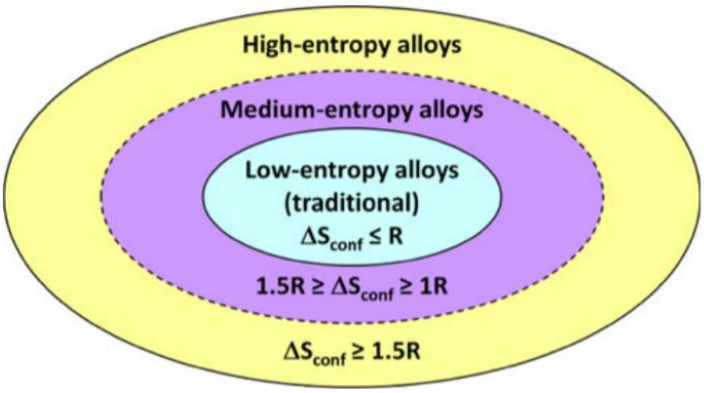

Figure 2. 2 The alloy world separated by S_{conf} of their random solution conditions. Adopted from [22]

The number of elements within the alloy ideally have been selected between 5 and 13. This is mainly because below 5 elements, S_{conf} does not balance the mixing enthalpy of most alloy to constitute the solid solution phases as discussed above. The reason why 13 principal elements are the upper limit is that the configurational entropies of equiatomic alloys containing 13, 14, 15, 20, and 40 elements are 2.57R, 2.64R, 2.71R, 3.0R, and 3.69R, respectively. When the number of elements is increased from 13 to 14, the rate of increase, 2.7%, is quite low. Therefore, increment of the number of elements above 13 is not necessary since this may have negative effects on production and recycling processes [1,22].

In fact, composition range (5-35 %) for HEAs cannot be specified with clear boundaries. Several assumptions are derived. One of them is that an element with concentration of 5 at. % makes a contribution of 0.15R to configurational entropy. This value corresponds to 10 % of the minimum configurational entropy value, 1.5R. Thus, the minimum principal element concentration is supposed to be higher than 5

at.% [22]. Another assumption is that an equiatomic alloy including 25 elements can be thought HEA although the concentration of each element is smaller than 5 at.%. It is well known that low carbon steels may contain alloying elements up to 4 wt.% [23]. When this proportion is increased, different kind of steels is produced. Therefore, the upper limit for these steels constitutes a guide for HEAs [22].

2.4 Four Core Effects

There are several important factors to designate the microstructure and critical properties of HEAs. Among these factors, four core effects, which are high entropy, lattice distortion, sluggish diffusion and cocktail, are thought to be the principal factors [22,24]. High entropy effect is quite critical to ensure simple solid solution phases with FCC, BCC or HCP structures for thermodynamic approach. Mechanical, structural or other properties of HEAs are affected constitutively by lattice distortion. For kinetic approach, sluggish diffusion decreases phase transformation rate that enables to form nanocrystalline or amorphous structures. The last effect is called as cocktail effect that provides the composite effect on properties due to the interaction between the unlike atoms themselves. All of these effects are discussed below in detail.

2.4.1 High Entropy Effect

High entropy effect is the most critical for HEAs in order to constitute simple solid solution phases and to improve the microstructure compared to formerly expected. According to Gibbs phase rule [16], there are several parameters to give the maximum number of expected phases. These are the degrees of freedom (F) a system, number of phases (P), number of components (C), at constant pressure in equilibrium condition. This rule indicates that the number of phase in condensed system and equilibrium condition cannot be higher than C+1 value. In different conditions such as F is equal to zero, the number of phases may decrease.

$P+F=C+1$ Equation 2.7

However, the number of obtained phases from HEAs contradict the maximum number of phases defined by the phase rule due to their high configurational entropy values. Supposing that this high entropy facilitates the solubility of phases within themselves. Therefore, this effect prevents the formation of many undesirable phases. Moreover, the diffusion rate of atoms is low, so the formation of several phases in such alloys is kinetically restricted. As a consequence, not only high configurational entropy but also low diffusion rate in HEAs affects significantly the number of phases to occur [21].

Some HEAs can involve intermetallic phases due to the strong bond between metallic elements. Intermetallic phases are also described as relatively ordered solid solutions [25,26]. In solid state thermodynamic approach, when temperature is increased, vacancy concentration and solubility of solutes in solvent atoms also increase. As a result of this, S_{conf} of the system gradually begins to rise. Furthermore, S_{conf} expands the solubility of elements in intermetallic compounds and these phenomena are also proved by using equation 2.2, i.e. $\triangle G_{mix} = \triangle H_{mix} - T\triangle S_{mix}$ in which mixing entropy affects free energy change much more than mixing enthalpy at higher temperatures. Thus, it is expected that HEAs having substantially higher mixture entropy for the random solid solutions significantly broaden the range of solubility of intermetallic compounds and create simple solid solution phases particularly at high temperatures.

Table 2.1, which shows the comparison of ΔH_{mix}, ΔS_{mix}, and ΔG_{mix} of elemental phases, compounds, intermediate phases and random solid solutions for n-element HEAs that have stronger bonding between atomic pairs, demonstrates in more detail as mentioned above. ΔH_{mix}, ΔS_{mix}, and ΔG_{mix} values of elemental phases are almost zero because they contain only one principal element. However, ΔH_{mix}, and ΔG_{mix} values of compound phases are large negative and ΔS_{mix} value is almost zero due to small mixing entropy in ordered structures. On the other hand, ΔH_{mix}, and ΔS_{mix}

values of random solid solutions described as HEAs are medium negative and highest respectively.

Table 2. 1 ΔH_{mix}, ΔS_{mix}, and ΔG_{mix} of elemental phases, compounds, intermediate phases and random solid solutions for n-element HEAs with strong bond between elements. Adopted from [22]

Comparative States	Elemental Phases	Compounds	Intermediate Phases	Random Solid Solutions
$\triangle H_{mix}$	~ 0	Large negative	Less large negative	Medium negative
$\triangle S_{mix}$	~ 0	~ 0	Medium	$\Delta S_{mix} = -R\sum_{i=1}^{n} X_i \ln X_i$
$\triangle G_{mix}$	~ 0	Large negative	Larger negative	Larger negative

Many studies showing evidence of high entropy effect have been conducted in the literature [2,18,23–27]. Figure 2.3 also shows the relative levels of mixing free energy curves of pure elements, intermetallic compounds and random solution at 1473 K for equimolar HEA containing eight elements to prove high entropy effect. The value of average mixing between two atom pairs is supposed as - 23 kJ/mol at 1473 K [7]. It can be concluded that the free energy of eight element alloys is the lowest value This is an important evidence that why HEAs are thermodynamically stable.

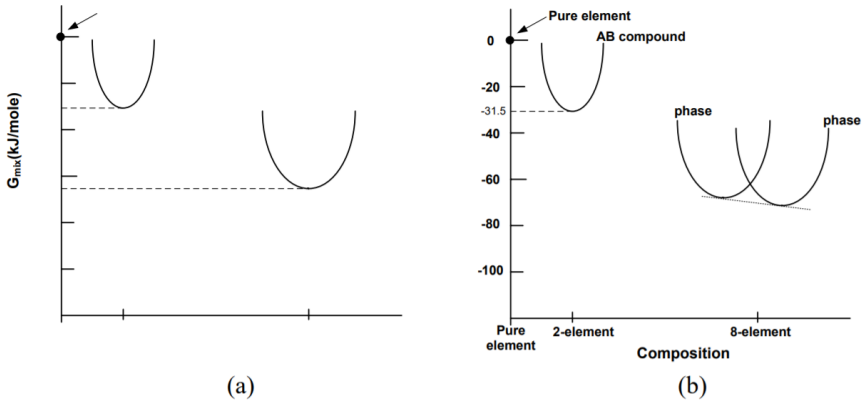

Figure 2. 3 The relative levels of mixing free energy curves of three different condition, i.e. single element, compound and random solution at 1473 K for equimolar HEA containing eight elements. (a) is for single stable phase and (b) is for two coexisting phases. Adopted from [7]

2.4.2 Lattice Distortion Effect

Since each element is completely dissolved in matrix and each atom is surrounded by other different atoms, this leads to lattice strain and stress because of the difference in atomic radius of elements. Figure 2.4 shows distorted lattice of a solid solution with 10 different principal elements with two vacancies. In addition to differences in atomic radius of elements, the diverse binding energy between the constituent elements and the crystal structure between the constituent elements are induced the increment of lattice distortion [28,29] .

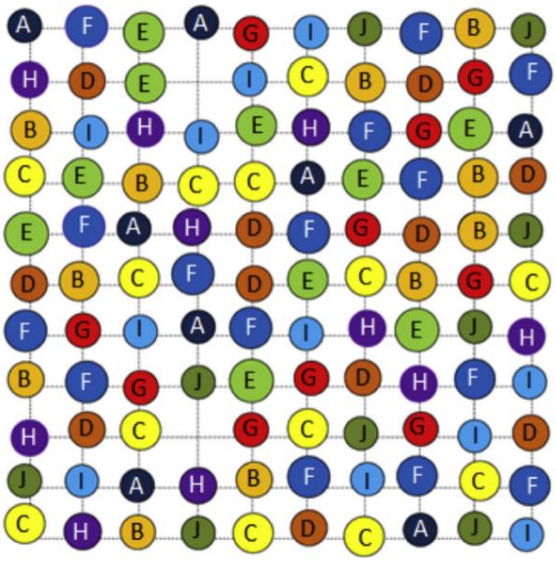

Figure 2. 4 Representation of distorted lattice of a solid solution with 10 different principal elements with two vacancies. Adopted from [21]

A study conducted by Senkov et. al. indicates that FeCoCrNiMn equiatomic HEA has FCC crystal structure and 1192 MPa Vickers hardness in the homogenized condition whereas 864 MPa was calculated by using rule of mixture. In addition, MoNbTaVW equiatomic refractory HEA has BCC crystal structure and 5250 MPa Vickers hardness that is more than three times in comparison with 1596 MPa obtained by the rule of mixture. It is well understood that solid solution hardening in BCC alloys is much higher than FCC alloys [28].

2.4.3 Sluggish Diffusion Effect

The formation of new phases necessitates the diffusion of many different types of atoms together in order to carry out the partition of the composition in HEAs. As discussed in the above section, HEAs may include random or ordered type of solid solutions. The matrices of HEAs can be considered as fully soluble. Consequently, the diffusion of an atom in a completely soluble matrix would not be same with respect to that in the matrix of conventional alloys. A vacancy in the matrix is actually encompassed by atoms of different elements during diffusion. It has been claimed that since the lattice potential energy (LPE) among lattice zones has changed significantly, HEAs have higher activation energy that is directly related to slow diffusion kinetic. The low LPE sites would obstruct the diffusion of atoms in matrix. This condition causes the sluggish diffusion effect [32].

A study, which is related to determine the diffusion rate of different elements in an ideal solid solution system indicates that the lowest and the highest diffusion rates are Mn and Ni respectively. The diffusion coefficient of each element in the FeCoCrNiMn HEA is the lowest values compared to Fe-Cr-Ni, Fe-Cr-Ni-Si and pure Fe, Co, and Ni elements. The activation energy of diffusion normalized by the melting point for Fe, Co, Cr, Ni, and Mn in different matrices: pure metals, stainless steels, and FeCoCrNiMn HEA is shown in Figure 2.5. According to these results, the activation energy normalized by the melting point (Q/T_m) in HEA is the highest value, on the other hand pure metals have the lowest values. This means that when the number of element is increased in an alloy system, diffusion rate begins to slow down [32].

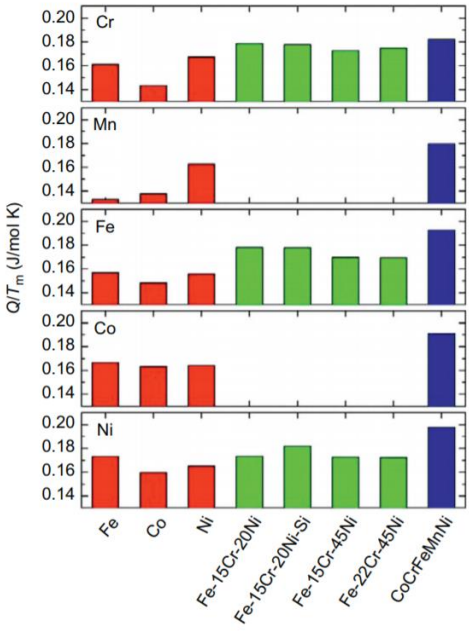

Figure 2. 5 Activation energy of diffusion normalized by the melting point for Fe, Co, Cr, Ni, and Mn in different matrices: pure metals, stainless steels, and FeCoCrNiMn HEA Adopted from [32]

Sluggish diffusion is expected to directly influence nucleation, growth, distribution, and microstructure of the formed phases. Indeed, it improves the properties of the material by changing the microstructure of the material. For example, fine precipitates can be obtained more easily in HEAs [34]. Therefore, the recrystallization temperature of the alloy is increased, grain growth and particle coarsening rates are decreased. As a result, improved creep resistance could extend the service life of parts used at high temperatures.

2.4.4 Cocktail Effect

The cocktail-party effect is often used as a term in the field of acoustics which have been identified the ability of a person to focus his or her attention on a single speaker among a mixture of speeches and background sounds [35]. On the other hand, for HEAs, the cocktail effect states that more than five principal elements can bring

about unexpected properties. This effect was first proposed by Ranganathan in a paper entitled “Alloyed pleasures: multimetallic cocktails” [36]. Since HEAs can have a single phase, or more phases changing with the composition, all constitute phases contribute the properties of them in terms of their sizes, shapes, and distributions. Indeed, the characteristics of these alloys are very similar to composite materials composed of two or more constituent materials with significantly different physical or chemical properties. In other words, each phase can be considered as a member of the composite structure. Composite properties come from both the own properties of the elements by rule of mixture, interaction of the elements with each other and lattice distortion effect. Interaction of the elements and lattice distortion effect are more outstanding contributions compared to the rule of mixture. The effects of this property on different HEAs are indicated in many studies in the literature [20, 30, 33–35].

Figure 2.6, which shows the change of the hardness of the $Al_xCoCrCuFeNi$ alloys as a function of Al content, is an example to describe the cocktail effect much more clearly [24]. This indicates that when the Al amount in HEA is increased, the hardness of the HEAs is changed significantly. In addition, phase transformation from FCC to BCC is observed due to the increase in Al content. This is directly associated with the cocktail effect explained by the interaction of the constituent elements. In other words, increasing the Al content in the HEAs induces the formation of a hard BCC phase due to the strong interaction bond of the Al with other constituent elements.

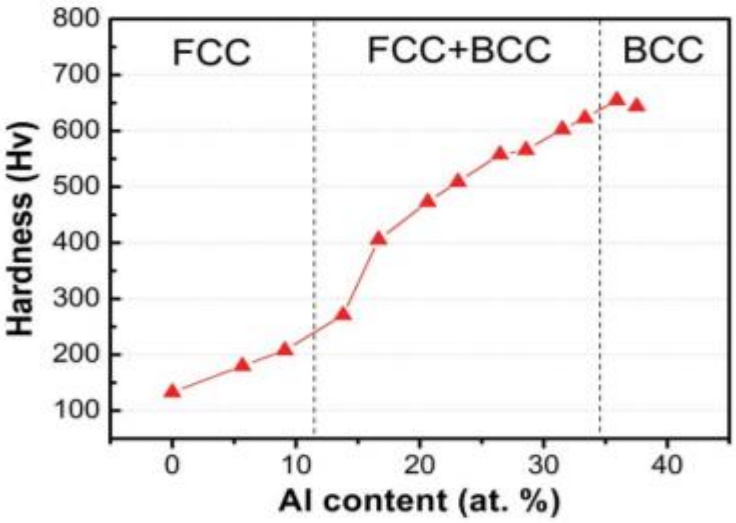

Figure 2. 6 Hardness of the $Al_xCoCrCuFeNi$ alloys as a function of Al content. Adopted from [24]

2.5 Thermodynamic Parameters to Estimate the Formation of Solid Solution Phases

The requirements for the formation of binary solid solutions are identified as Hume-Rothery rules [40]. In 1920s, Hume-Rothery described the factors that affect compound formation and change in behaviour of alloys. These factors are solubility and atomic size, crystal structure, valance electron concentration and electronegativity of the components in an alloy. Although there are other studies on the formation parameters of solid solution phases, Hume-Rothery is significantly important in material science. These rules can be briefly explained as follows [41]:

1. The difference between the radius of solvent atoms should not be greater than 15%, and that should be less than 8% for a complete dissolution.

2. The two elements should have similar crystal structures for the extended solid solubility.

3. The electronegativity values of the two elements should be the same in order to eliminate the formation of intermetallic compounds.

This definition should be revised for HEAs containing multicomponent equiatomic or near equiatomic elements. Therefore, thermodynamics parameters such as enthalpy of mixing (ΔH_{mix}), entropy of mixing (ΔS_{mix}), and topological parameters like atomic size difference (δ) are defined by Zhang et al. [42] in order to understand the concept of formation of these alloys more clearly.

The enthalpy of mixing of the HEA is calculated as [43]:

$$\Delta H_{\text{mix}} = -R \sum_{i=1}^{N} \Omega_{ij} c_i c_j \qquad \text{Equation 2.8}$$

where c is defined as the atomic fraction of element i and j, and $\Omega_{ij} = 4\Delta H_{mix}^{AB}$, ΔH_{mix}^{AB} is the mixing enthalpy of binary liquid AB alloys.

The atomic size difference (δ) of the HEA described as:

$$\delta = 100 \sqrt{\sum_{i=1}^{N} c_i \left(1 - \frac{r_i}{\bar{r}}\right)^2} \qquad \text{Equation 2.9}$$

Where $\bar{r} = \sum_{i=1}^{N} c_i r_i$, c_i and r_i are defined as the atomic percentage and atomic radius of the ith element respectively.

The entropy of mixing of the HEA is also calculated according to Equation 2.6.

Figure 2.7 shows the calculated phases by changing the atomic size difference (δ) and the enthalpy of mixing (ΔH_{mix}). The enthalpy of mixing (ΔH_{mix}) and the atomic size difference (δ) ranges should be $-22 \leq \Delta H_{\text{mix}} \leq 7$ kJ/mol and $\delta \leq 8.5$ respectively in order to form solid solution phases (BCC, FCC, and BCC+FCC) which is shown as S and S' in the figure [42]. Actually, it should not be expected that an alloy present in these regions will form a solid solution phases. However, these ranges are based on quite realistic approaches: if the value of ΔH_{mix} is much higher than 7 kJ/mol, this causes phase separation and if the value of ΔH_{mix} is much lower than -22 kJ/mol, this generally leads to the formation of intermetallic phases [44]. In addition, it is understood from the figure that the increment of δ parameter induces more negative values of ΔH_{mix}. It is also very important that δ parameter is sufficiently small because as the atomic size difference between the alloying

elements increases, the crystal structure of the alloy accumulates excessive strain energy, which leads to the distortion of the crystal structure.

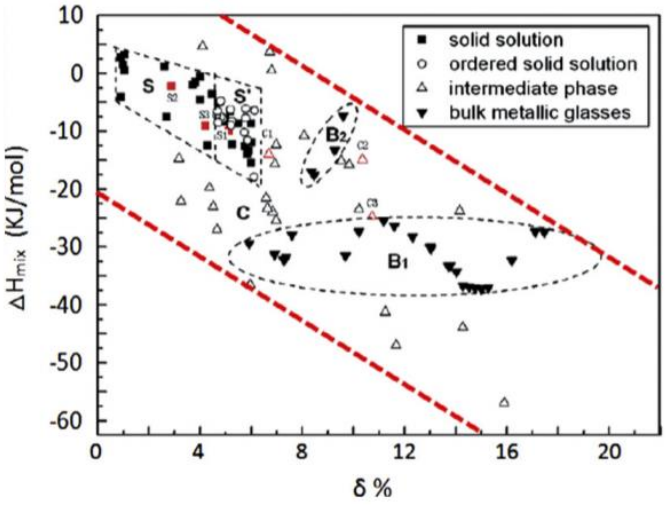

Figure 2. 7 A phase formation map by changing the atomic size difference (δ) and the enthalpy of mixing (ΔH_{mix}). B_1 and B_2 zones indicate the glass formation regions. C is for the intermetallic compounds. Adopted from [42]

When ΔS_{mix} value is considered together with ΔH_{mix}, and δ parameters, ΔS_{mix} range is calculated to form solid solution phases as follows: $11 \leq \Delta S_{mix} \leq 19.5$ J/(K mol) [42]. The fact that ΔS_{mix} of the alloy is sufficiently high to stabilize the simple solid solution phases have to be considered. However, when simple disordered phase (SDP) is taken into account, all of the parameters mentioned above are considerably limited: $-15 \leq \Delta H_{\mathrm{mix}} \leq 5$ kJ/mol, $\delta \leq 4.3$ and $12 \leq \Delta S_{mix} \leq 17.5$ J/(K mol) [45].

As none of the above-mentioned parameters gives any information about the Bravais lattice of the crystal structure, the valence electron concentration (VEC) was proposed by Guo et al. [46] to identify the BCC and FCC phase formation in HEAs. This value is calculated by Equation 2.10. If VEC is higher than 8, the FCC phase becomes stable, if VEC is smaller than 6.87, the crystal structure of the alloy is BCC and if VEC is between 6.87 and 8, the alloy comprises of both the FCC and BCC. As shown in the figure, Co and Ni elements with VEC of 9 and 10 respectively ensure

the stability of the FCC phase whereas Al and Ti elements with VEC of 3 and 4 respectively stabilize the BCC phase. Some of HEAs remain stable at intermediate temperatures. In other words, while single phases are obtained in HEAs produced at high cooling rates, intermediate temperature phases are seen in the alloys that have been annealed. η phase [47] and σ phase [25,47,48] have been observed in the literature. As a result of these phases, the properties of HEAs are affected adversely.

$$VEC = \sum_{i=1}^{N} c_i \, (VEC)_i \qquad \text{Equation 2.10}$$

However, as a result of researches conducted so far, these VEC ranges have been still discussed in the literature and the mechanism behind the effect of VEC on phase formation has not been fully comprehended [49-52].

2.6 Computational Methods in HEAs

2.6.1 Ab Initio Molecular Dynamics (AIMD) Simulations

Ab-initio Molecular Dynamics (AIMD) is a method based on Density Functional Theory (DFT) to combine molecular dynamics simulations and electronic structure calculations. This method was developed by Hohenberg and Kohn in 1964 during the calculation of the energy of a solid or molecule with the help of DFT [54]. They have found the use of electron density as a function of time and place. Since AIMD simulations calculate easily and quickly instantaneous forces on atoms, in contrast to the classical MD simulations which require experimental data AIMD simulations are very effective to estimate the individual atomic orbits of solids or liquids held at elevated temperatures. AIMD simulations have been commonly used to have knowledge about the structural, dynamic, thermodynamic properties, optimized geometries, electron band structures, total energies and magnetization properties of materials at different temperatures [54-56]. The calculations of all mentioned properties can be carried out by Vienna Ab initio Simulation Package (VASP) computer program. In addition, different approaches and functions are used in

performing these calculations. One of the most widely used approaches is Generalized Gradient Approach (GGA) which is related to DFT. This approach enables to find the correlation energy of the system. According to this approach, the electron at each point in the system has the same interaction and density as the other electrons around each point in the system. In complex systems with more than one atom, this approach gives quite accurate results. These approaches generally are divided into different types of function classes. One of the most widely used function is Perdew-Burke-Ernzerhof (PBE) which calculates the electronic exchange correlation potential of the system [58]. This function is preferred because it facilitates GGA and many of the mathematical and physical calculations that DFT needs.

As mentioned before, AIMD simulations are frequently used before conducting the experiments. HEAs implemented in AIMD simulations allow a wide range of composition to be investigated. For example, AIMD simulations of the selected HEAs were conducted by Gao et al [59]. In this study, the microstructure changes of $Al_xCoCrCuFeNi$ HEA (x: 0,0.5,1,1.3) during solidification were observed at constant volume, zero pressure and the change of structure during solidification of $Al_xCoCrCuFeNi$ HEA at different temperatures (T: 2273, 2073, 1873, 1673, 1523, 1273, and 1023 K). The results indicate that Cu was strongly clustered compared to other elements in different regions of $Al_{1.3}CoCrCuFeNi$ HEA in liquid state. The data obtained by AIMD simulations were very similar compared to those obtained experimentally [59,60]. In another example Calvo-Dahlborg et. al. [62] has carried out AIMD simulations in the framework of DFT and VASP on $CoCrFeNiPd_x$ (x: 0, 0.255, 0.545, 1.0, and 1.5) in an attempt to compare experimental results and calculations of lattice constants. Both studies give similar results which shows that the structure of the HEAs was calculated as FCC. In this study, crystal structure of the selected HEAs are investigated in terms of simulation and experimental method and the differences between the crystal structures obtained from the methods are compared.

2.6.2 Thermo-Calc Software

Thermo-Calc software based on CALPHAD technique is a computational method that is used in the estimation of the composition, structure and properties of the material**.** The calculation is made with the combination of thermodynamics and kinetics concepts. The database of Thermo-Calc are developed by material engineers who are experts in their fields as a result of the combination of extensive scientific researches, experimental and theoretical data.

This method is widely used in different thermochemical calculations such as calculations of stable and semi-stable heterogeneous phase equations, phase ratios and composition amounts, thermochemical calculations such as enthalpy, heat capacity and thermal transformations, phase diagrams containing binary, triple and multiple components thermodynamic properties of chemical reactions.

In this study, Thermo-Calc software as used to determine the melting temperatures of the alloys required for VASP simulation.

2.7 Production Methods of HEAs

2.7.1 Production from the Liquid State

Arc furnace and induction furnace are the most common methods to prepare the alloy from the molten state. However, the working principles of these two types of melting methods are different. Arc melting method is described as the result of the formation of the arc between the charged material and the electrode to melt raw materials. On the other hand, induction melting method is based on the formation of the eddy current in the metal (usually conductive material) which causes the heating of the metal to its melting temperature. The induction furnace is much more suitable for the elements with low melting temperature, such as Mg, Mn or Zn compared to the arc furnace. Singh et. al [63] has studied about the change of microstructures of HEAs

according to the cooling rate shown in Figure 2.8 which describes the phase segregation during solidification of AlCoCrCuFeNi HEA by splat quenching process (cooling rate:10^6 –10^7 K s^{-1}) and casting process (cooling rate 10–20 K s^{-1}). This study indicates that dendritic microstructures are observed because of elemental segregation at low cooling rates. On the other hand, high cooling rate leads to the formation of polycrystallite phases with nanometers in size.

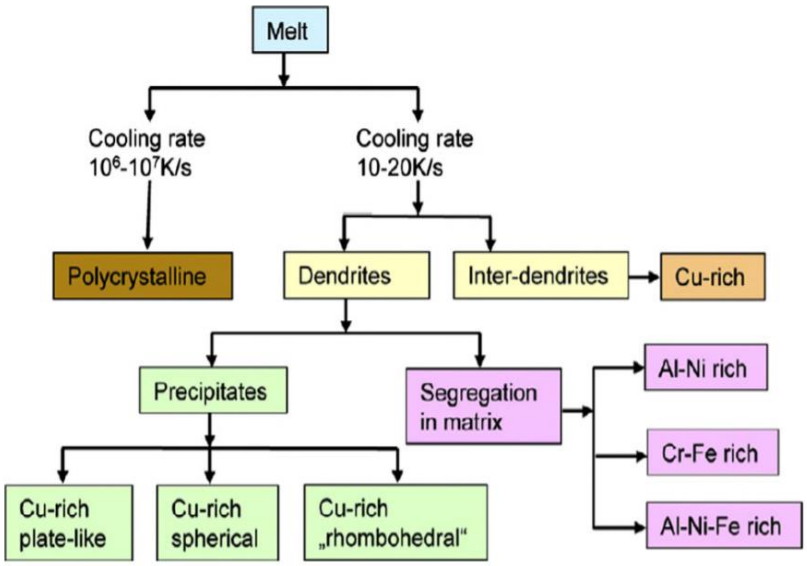

Figure 2. 8 Schematic demonstration of the phase segregation during solidification of AlCoCrCuFeNi HEA by splat quenching process (cooling rate:10^6 –10^7 K s^{-1}) and casting process (cooling rate 10–20 K s^{-1}). Adopted from [63]

2.7.2 Production from the Solid State

The most commonly used production method from the solid state is mechanical alloying (MA). This method can be defined as a process which involves powdering the materials by repeated cold welding and fracturing with high energy ball mill and then re-welding of them [21,64]. Nowadays, MA method is generally used to obtain alloys in equilibrium and non-equilibrium states by combining powder of elements. The mechanical alloying process which consists of 3 steps. First of all, alloy materials are turned into fine powders by the help of the ball milling. Then, powders

are compressed and sintered simultaneously which is known as hot-isostatic-pressing (HIP) process. Finally, a heat treatment is applied to remove internal stresses during alloying process.

2.7.3 Production from the Gas State

Sputter deposition which surface coating method is frequently used to produce HEAs from the gaseous state. This method can be defined as a second surface forming process on the target material by ion bombardment. Chang et al. [65] has performed HEA coatings for tribological applications on (AlCrTaTiZr)N_x alloy by using sputtering deposition method. The effect of the change in N contents on the mechanical properties, creep behaviour, deformation mechanisms and interface adhesion of the coatings was investigated. The structure of the (AlCrTaTiZr)N_x coatings has changed from amorphous, nanocomposite and crystalline nitride respectively due to the increment of the flow ratio (R_N). According to the mechanical testing results, the hardness of the coating surfaces substantially increased from 13 GPa to 30 GPa [65].

2.8 Mechanical Properties of HEAs

Hardness, elastic modulus, yield strength, tensile strength, elongation, fatigue and creep properties are among the most important mechanical properties of the material. The mechanical properties of HEAs are expected to perform better than other conventional alloys for critical applications since they contain multi-principal elements and have noticeable core effects as discussed before. As seen from Figure 2.9, HEAs have the highest strength and specific strength among the materials. The mechanical properties of HEAs at room temperature and high temperatures are described in more detail in the following sections.

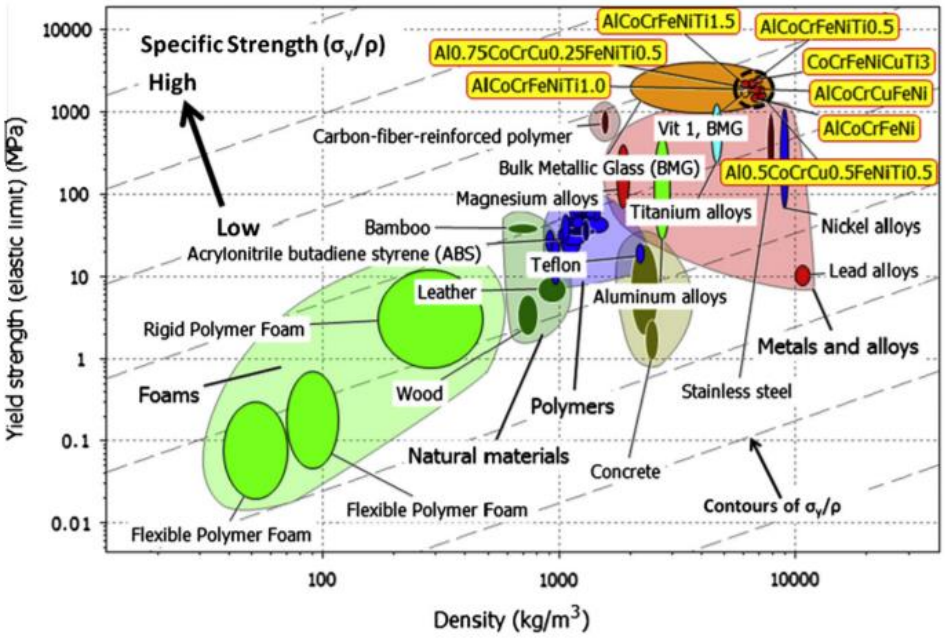

Figure 2. 9 Yield strength vs. density diagram of HEAs compared with other materials. Adopted from [16]

2.8.1 Room Temperature Mechanical Properties

This section describes the hardness, compression and tensile properties of HEAs obtained by using different production methods such as cast, wrought and mechanical alloying processes. Many studies have been investigated on the mechanical properties of FeCoCrNi HEA. One of the study conducted by He et al. [2] show that FeCoCrNi has FCC solid solution and 165 MPa yield strength, 400 MPa tensile strength with 68% elongation by using drop casting method.

Other HEAs used widely for the investigation of their mechanical properties is AlxCoCrCuFeNi alloys [4,6,69]. Study conducted by Tong et al.[6] indicates that when the Al ratio (x) in the alloy was changed from 0 to 0.5, the hardness of the alloy increases significantly from 133 HV to 655 HV as shown in Figure 2.10. it is a known fact that the atomic size of Al is the highest among the other elements of the alloy so lattice distortion increases with the increment of Al content. In this alloy, crystal

structure transforms from FCC to BCC (disordered and ordered BCC). The BCC phases are harder than the FCC phase. Increasing the amount of Al also provides solid solution strengthening in the alloy. In addition, nanoprecipitates formed by sluggish diffusion kinetics enhance significantly the hardness of the alloy.

Figure 2.10 demonstrates the total crack length indicated toughness of the alloy around with different aluminum contents. The crack formation does not be observed in FCC region. However, the crack begins to form with the occurrence of BCC phase. As BCC phase becomes more dominant, the crack length increases, which indicates that the material becomes more brittle structure.

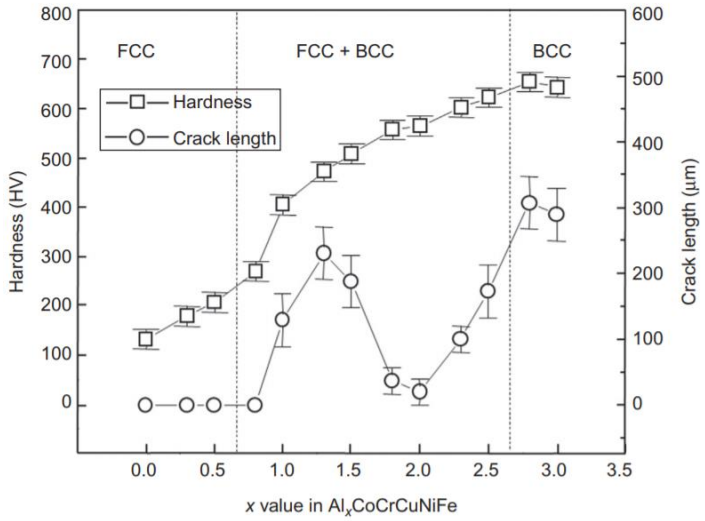

Figure 2. 10 The change in the hardness of $Al_xCoCrCuFeNi$ alloy and total crack length around the hardness indent with different aluminum contents (x values). Adopted from [6]

It has been understood that HEAs containing Ti exhibit very good mechanical properties under compression loads. As an example study, Zhou et al. [5] has made investigation about the mechanical properties of $AlCoCrFeNiTi_x$ (x: molar ratio; x: 0, 0.5, 1, 1.5) in compression load. The most suitable mechanical properties among HEAs with different atomic ratios were found as $AlCoCrFeNiTi_{0.5}$ alloy. This alloy has BCC structure and yield strength, fracture strength and plastic strain were obtained as 2.26 GPa, 3.14 GPa and 23.3%, respectively. These values are

considerably higher as compared to high strength alloys, even BMGs. The reasons behind this high strength are based on BCC-structured precipitates resulting from spinodal decomposition in addition to solid solution strengthening.

Compression test have been generally studied in the literature due to the fact that the produced alloys are laboratory-scale. However, the investigations of the behavior of HEAs under tensile load have been increasing progressively. Tsai et al. [66] has studied the tensile behavior of the cold rolled $Al_{0.5}CoCrCuFeNi$ HEA with 80% reduction. The yield strength, tensile strength and plastic strain of the alloy was 1292 MPa, 1406 MPa and 6%, respectively at room temperature. When annealing process was applied to cold rolled specimens at 1173 K, the yield strength and tensile strength of the material become 656 MPa and 796 MPa, respectively. The strength of the alloy decreased significantly but the ductility of the material increased up to 29%.

2.8.2 High Temperature Mechanical Properties

HEAs can be good candidate materials that are used at elevated temperatures due to their slow diffusion kinetics. Several studies have been carried out to investigate the properties of these alloys under high temperatures. One of them conducted by Hsu et al. [67] is related to investigation of mechanical properties of $AlCo_xCrFeMo_{0.5}Ni$ HEA under elevated temperatures. Experimental results indicate that $AlCoCrFeMo_{0.5}Ni$ alloy has hardness of 347 at 1273 K, which is higher than 220 HV of Ni based superalloys IN 718/IN 718H. Another study carried out by Juan et al. [68] indicates that the hot hardness value of $AlCoCrFeMo_{0.5}Ni_x$ (x: 0-1.5) alloys were found to be higher compared to Ni based and Co based alloys up to 1273 K as shown in Figure 2.11.

MoNbTaW and MoNbTaVW refractory HEAs introduce high yield strength under compression load at 1873 K which is higher than the melting point of Ni and Co base superalloys [28]. Another refractory HEAs containing NbTiVZr, $NbTiV_2Zr$,

CrNbTiZr, and CrNbTiVZr attained 50% strain without fracture at 1273 K. Although HEAs including Cr exhibit low ductility values at room temperature, significant ductility at high temperatures is obtained. The specific strength of CrNbTiVZr alloy is much better than the other 3 HEAs and IN 718 and Haynes 230 superalloys [28]. Therefore, the high strength of this alloy with low density is one of the most remarkable property at elevated temperatures. As a result, HEAs with low density, high strength and ductility can be produced, by means of the adjustments in the microstructure and composition.

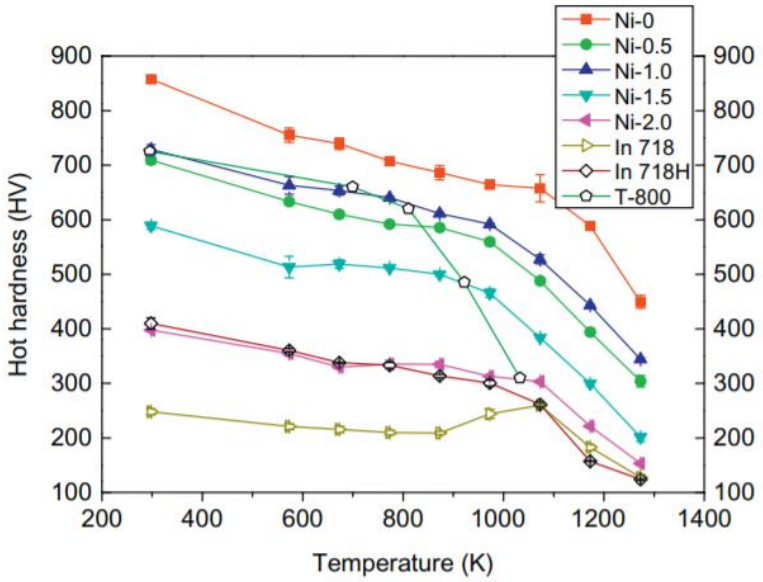

Figure 2. 11 The change in the hot hardness with temperature for Ni based superalloys IN 718/IN 718H, and Co-based superalloy of Tribaloy T-800 and $AlCoCrFeMo_{0.5}Ni_x$ alloys with varying Ni content. Adopted from [68]

CHAPTER 3

EXPERIMENTAL PROCEDURE

3.1 Computational Methods

3.1.1 Vienna Ab initio Simulation Package (VASP)

Estimated crystal structures of FeCoCrNi, FeCoCrNiCu and FeCoCrNiAl alloys were simulated using VASP before performing structural characterization. Molecular dynamics with Generalized Gradient Approach (GGA) based on DFT was used as the calculation method. Perdew-Burke-Ernzerhof (PBE) function, which is a class of GGA, was used as the correlation potential of electronic change. The temperature scale is defined as the cooling of the alloys from their molten states to room temperature. The melting temperatures of FeCoCrNi, FeCoCrNiCu and FeCoCrNiAl alloys obtained by Thermo-Calc software were chosen as 1900K, 1800K and 1700K respectively. The effects of the magnetic moments of the elements used in the simulation on the crystal structure were ignored. The simulation time interval for both alloys was chosen as 4.0 femtoseconds. When the selected time is below 4.0 femtosecond, it is difficult to find the equilibrium phase of the material correctly. Another important parameter used in the calculations is the plane wave cut-off energy. As atoms get closer to each other, the energy increases. if this energy is lowered, it extends the calculation time considerably. On the other hand, in case where this value is too high, results are obtained incorrectly. The plane wave cut-off energy of the alloys was taken as default values given by the program for the applied simulations. Each atom has a certain minimum and maximum cut-off energy. The default values are derived from the average of these two energies. Particularly in systems with more than one type of atom, the accuracy of the results obtained by using this average is quite high. The purpose of this simulation is to determine the

crystal structures of the alloys and compare with to the ones predicted by VEC value of the alloys.

3.1.2 Thermo-Calc Software

Phase diagrams of the alloys were plotted with Thermo-Calc program in order to determine the melting temperatures of FeCoCrNi, FeCoCrNiCu and FeCoCrNiAl alloys used in VASP program. In the first step of creating phase diagrams, the mass percent of all alloys were defined as input to the program. After that, the possible phases were selected. Then, the system condition was defined as temperature, pressure and system size. Temperature was set to highest possible value of 2500 K. 1 atm was selected as the pressure. Finally, the calculation was started and the mass percentage of one of the constituent elements of the alloy with respect to the temperature was plotted.

3.1.3 HEA Calculator

δ, ΔH_{mix}, ΔS_{mix}, VEC values of the all alloys were calculated by HEA calculator program. The software calculates ΔH_{mix} value according to the equation 2.6, ΔS_{mix} value according to the equation 2.7, δ value according to the equation 2.8 and VEC according to the equation 2.9. The expected crystal structure of the alloys was also determined from calculated VEC values which are defined in accordance with certain thermodynamic rules.

3.2 Production of Alloys

Commercial grade raw materials were used to produce impure FeCoCrNi, $FeCoNiCu_x$, and $FeCoNiAl_x$ (x: 0.3, 0.6, 1) HEAs. Chemical compositions of raw materials are shown in Table 3.1. Composition analyses of the materials were done by FEI Nova NanoSEM 430 EDS (Electron Dispersive Spectroscopy). Chemical

composition of the elements used in the experiments is shown in 3.1. Equiatomic amount of raw materials are weighted to produce the alloy. FeCr was used as Fe and Cr source. Additional low carbon steel (99.8 Fe wt. %) was used to balance atomic ratio of Fe and Cr in FeCr. The other raw materials were used as received.

Table 3. 1 Chemical compositions of the raw materials

Raw Materials	Composition (wt.%)							
	Fe	**Cr**	**Co**	**Ni**	**Al**	**Si**	**Cu**	**C**
FeCr	25.5	72	-	-	0.5	2		-
Fe (Low Carbon Steel 0.20 % C)	Balance	-	-	-	-	-	-	0.18-0.23
Ni	-	-	-	98.7	1.3	-	-	-
Co	-	-	98.7	-	0.5	0.8		-
Cu	0.9	-	-	-	-	0	99.1	-
1050 Al	0-0.4%	-	-	-	Balance	0-0.25%	0-0.05	-

All impure specimens were produced by using Indutherm MC+15 induction casting machine as shown Figure 3.1. Argon was blown into the chamber, and then vacuum process was applied via vacuum pump shown in Figure 3.1 (a). This cycle was repeated 3 times to prevent production problems such as oxidation. The casting process was carried out under vacuum sealing to 10^{-1}-10^{-2} mbar. All raw materials were put into the ceramic crucible shown in Figure 3.1 (b) Then, the crucible was placed in the induction coil. Magnetic field is created by passing current through the coil. Energy is transferred to electrically conductive materials by electromagnetic induction. Variable magnetic field is the field of induced electrical currents, called eddy currents, which result in joule heating. After the melting process was completed, the molten alloy was poured into the cylindrical copper mold with 5 mm diameter shown in Figure 3.1 (c). In addition, copper mold with 10 mm diameter shown in Figure 3.1 (d). was used to prepare ASTM tensile test specimens.

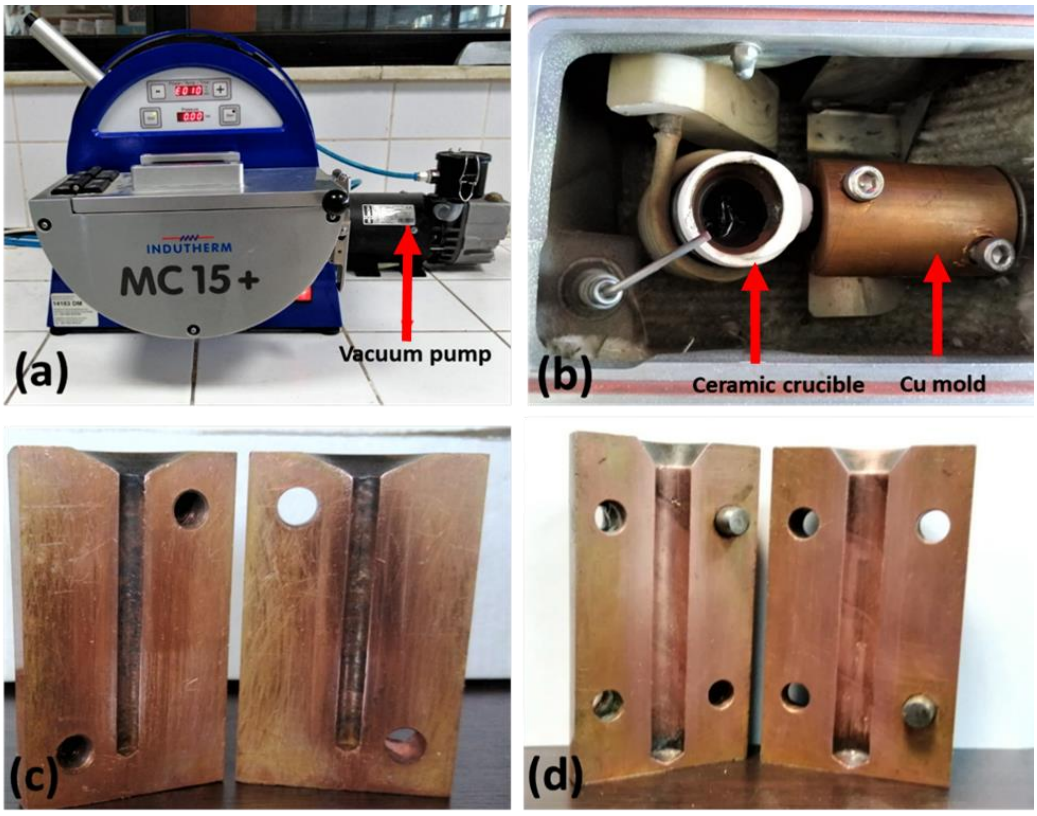

Figure 3. 1 a) Indutherm MC+15 Induction Casting Machine, b) important parts of the machine, (c) 5 mm diameter Cu mold, (d) 10 mm diameter Cu mold

Induction casting device requires minimum 20 grams of alloy. This situation brings about the very high pure material cost. Therefore, all pure specimens were produced by using Edmund Buhler MAM-1 arc melting device shown in Figure 3.2. The induction furnace was used only to perform tensile testing of pure FeCoNiCu HEA. Specimens were placed on copper mold shown in Figure 3.2 (b) in the arc melting. Ar was blown into the chamber in order to remove O_2. Then, the chamber is sealed with a vacuum value of approximately 10^{-3}-10^{-4} mbar. The specimens were re-melted three times at 5-8 mbar pressure to obtain better chemical homogeneity. After each melting process, the specimens were flipped upside down to improve homogeneity. Ingots were casted into 4 mm diameter copper mold shown in Figure 3.2 (c) by suction casting. In order to cast the molten alloy into the mold, the vacuum reservoir shown in Figure 3.2 (a) must firstly be vacuumed. There is also a vacuum reservoir

junction pipe shown in Figure 3.2 (a) which provides connection between the vacuum reservoir and the copper stage. As the melting process is carried out under positive pressure, a pressure difference occurs between the vacuum reservoir and the chamber. This pressure difference is controlled by a valve shown in Fig. 3.2 (a). The molten alloy is drawn into the cylindrical mold very rapidly under the influence of vacuum.

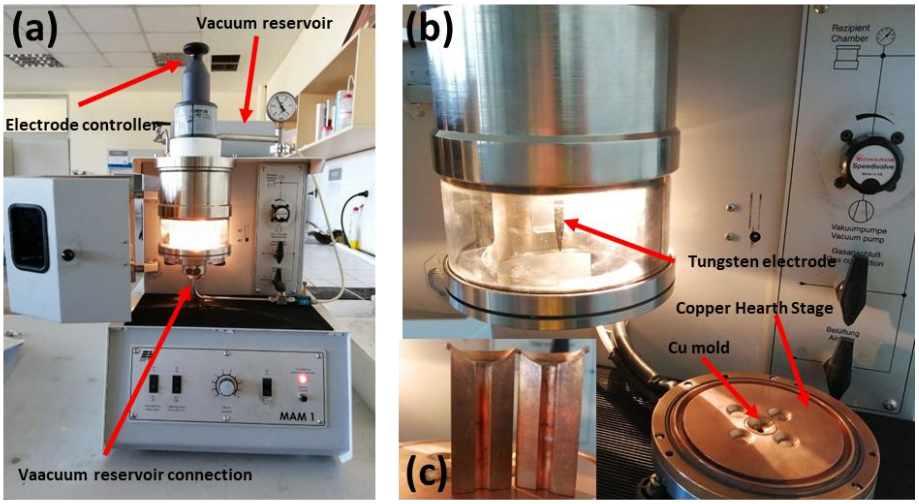

Figure 3. 2 Edmund Bühler MAM-1 arc melting device with important features labeled

3.3 Ambient and High Temperature X-ray Diffraction Analysis

The crystal structure of the rod specimens was investigated by X-ray diffraction (XRD). XRD measurements were performed by the help of D8 Advance Bruker X-ray Diffractometer shown in Figure 3.3 (a). Before XRD measurement, all specimens were grinded to eliminate possible contamination on the surface of the specimens. Figure 3.3 (b) shows X-ray tube of the diffractometer, which consists of a Cu Kα (λ = 1.5406 Å) anode and Ni filters. X-ray measurement was operated 40 kV voltage and 30 mA current. Data were collected between 20º and 100º at a scan rate of 2.0°/min.

In situ XRD measurement was also applied to observe the change in crystal structure of FeCoCrNi HEA at high temperatures. High temperature measurements were

performed by D8 Advance Bruker X-ray Diffractometer with in situ apparatus shown in Figure 3.3 (c) and (d). Data were collected between 20º and 100º at a scan rate of 2.0°/min. Heating was done by the resistance heater with heating rate of 10 ºC / min. In the first stage of the measurement, room temperature X-ray diffraction profile of the specimen was taken. After that, specimen was heated to 373 K and waited at this temperature for 10 minutes to ensure exactly the desired temperature value of the alloy and X-ray diffraction profile of the specimen was taken. The specimen was heated up to 1273 K by this method to collect data for every increment. The alloy heated to 1273 K was brought to room temperature (298 K) very quickly, and the final X-ray profile was obtained.

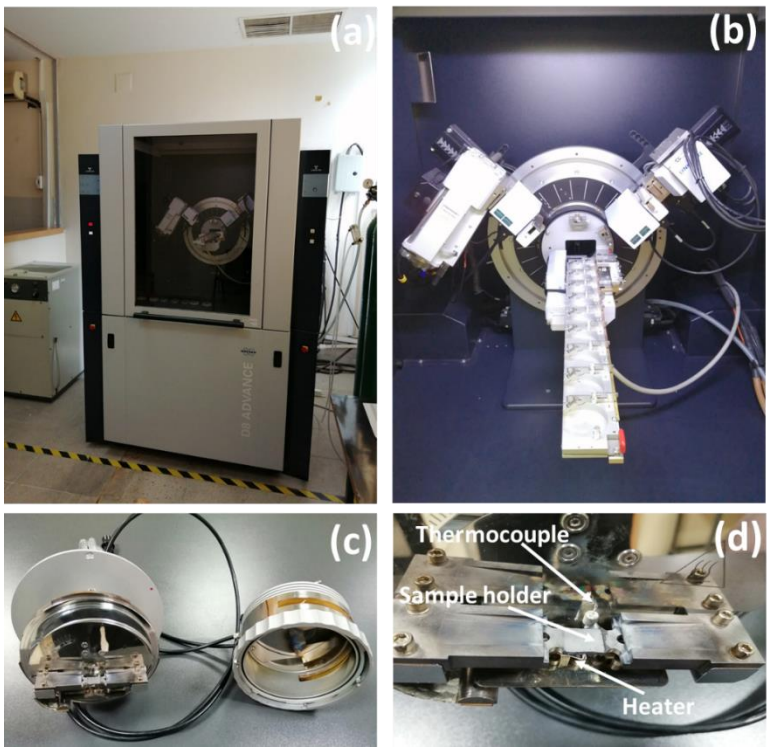

Figure 3. 3 Photographs of (a) D8 Advance Bruker X-ray Diffractometer Device (b) goniometer, X-ray tube, X-ray detector and specimen holders (c) high temperature XRD equipment and (d) heater, thermocouple and specimen holder of high temperature equipment.

3.4 Heat Treatment Process

The homogenization process of pure and impure FeCoCrNi HEAs was performed by using PROTHERM Tube Furnace shown in Figure 3.4. Firstly, the tube was taken into vacuum of approximately 10^{-3} mbar in order to prevent oxidation of the specimens. In order to determine the homogenization temperature of this alloy, 2/3 of the melting temperature of the alloy obtained from Thermo-Calc 2018b program, was found as approximately 1267 K. However, as a result of the conducted experiments, the dendritic structure of the impure FeCoCrNi alloy was not disrupted at this temperature. Hence, 1273 K was chosen as homogenization temperature which has been reported in many studies in the literature [68,70]. After the homogenization temperature was determined, the furnace was brought to 1373 K at a heating rate of 12.48 K / min. Specimens were kept at this temperature for 24 hours. After that, the furnace was turned off and the specimens were allowed to cool to room temperature.

Figure 3. 4 PROTHERM Tube Furnace used in this study

3.5 Scanning Electron Microscopy (SEM) Analysis

FEI Nova NanoSEM 430 scanning electron microscope (SEM) seen in Figure 3.5 was used in order to perform microstructural characterization of the produced alloys. Before the microstructural observation, metallographic preparation was applied. As a first step, small parts were cut from the produced specimens with the help of precision cutter. Then, these pieces were mounted into a bakelite holder to prepare the specimens properly. Afterwards, the surfaces of the specimens were grinded with sand papers from coarse 220 to fine 2000. After this step, the specimens were polished with 6 μm and 1 μm diamond pastes respectively to form a smooth and shiny surface. As it was frequently stated in the literature, HEAs are very stable and cannot be etched with weak acids. Therefore, aqua regia, a very strong acid, was used to etch specimens.

Figure 3. 5 Photography of FEI Nova NanoSEM 430 scanning electron microscope used in this study

3.6 Transmission Electron Microscopy (TEM) Analysis

Transmission Electron Microscopy (TEM) was utilized for further investigation of impure FeCoCrNi HEA. JEOL JEM2100F field-emission gun scanning/transmission electron microscope operated at 200 keV voltage shown in Figure 3.6 was used in this thesis. The specimen for TEM were prepared using Focused Ion Beam (FIB) microscope in Sabancı University.

Figure 3. 6 JEOL JEM2100F field-emission gun scanning/transmission electron microscope used in this thesis

3.7 Mechanical Tests and Fracture Analysis

Vickers test was done by using HMV Micro Vickers Hardness testing machine shown in Figure 3.7 (a) with a diamond pyramid indenter under 4.903 N (0.5 kgf) force to investigate hardness of the specimens. Hardness of the specimens was

scanned from one side to the other side and 6 measurements were done on polished specimens. Tensile test specimens were prepared according to ASTM E8/E8M. Tensile test specimens were prepared for pure and impure FeCoNiCr HEAs from cleaned specimens and each side of the tensile test specimens were grinded and polished to avoid stress concentration regions. Extensometer was used during the experiment. Cylindrical compression test specimens were also prepared for all specimens according to ASTM E9-19, with the dimensions of 4.0 ± 0.04 mm in diameter and 8.0 ± 0.08 mm in length (with an aspect ratio of 2:1) for pure specimens produced in arc melting and the dimensions of 5.0 ± 0.05 mm in diameter and 10.0 ± 0.1 mm in length (with an aspect ratio of 2:1) for impure specimens produced in induction melting. The surfaces of the cylindrical specimens were polished in order to increase the surface quality and to be perpendicular to the loading axis. Both of the tests were performed with Instron 5582 mechanical testing equipment with max. 100 kN shown in Figure 3.7 with (b) tension apparatus, (c) compression apparatus and (d) high temperature tension test furnace and related apparatus. Strain rate for tension test was 1 mm /min, and for compression test the rate is 10^{-4} s^{-1}. The extensometer could not be used because it was not suitable for compression test experiment and there is a friction between the contact surfaces of the compression sample and the anvils. The fracture surfaces of specimens were investigated by the help of FEI Nova NanoSEM 430 scanning electron microscope (SEM) seen in Figure 3.5.

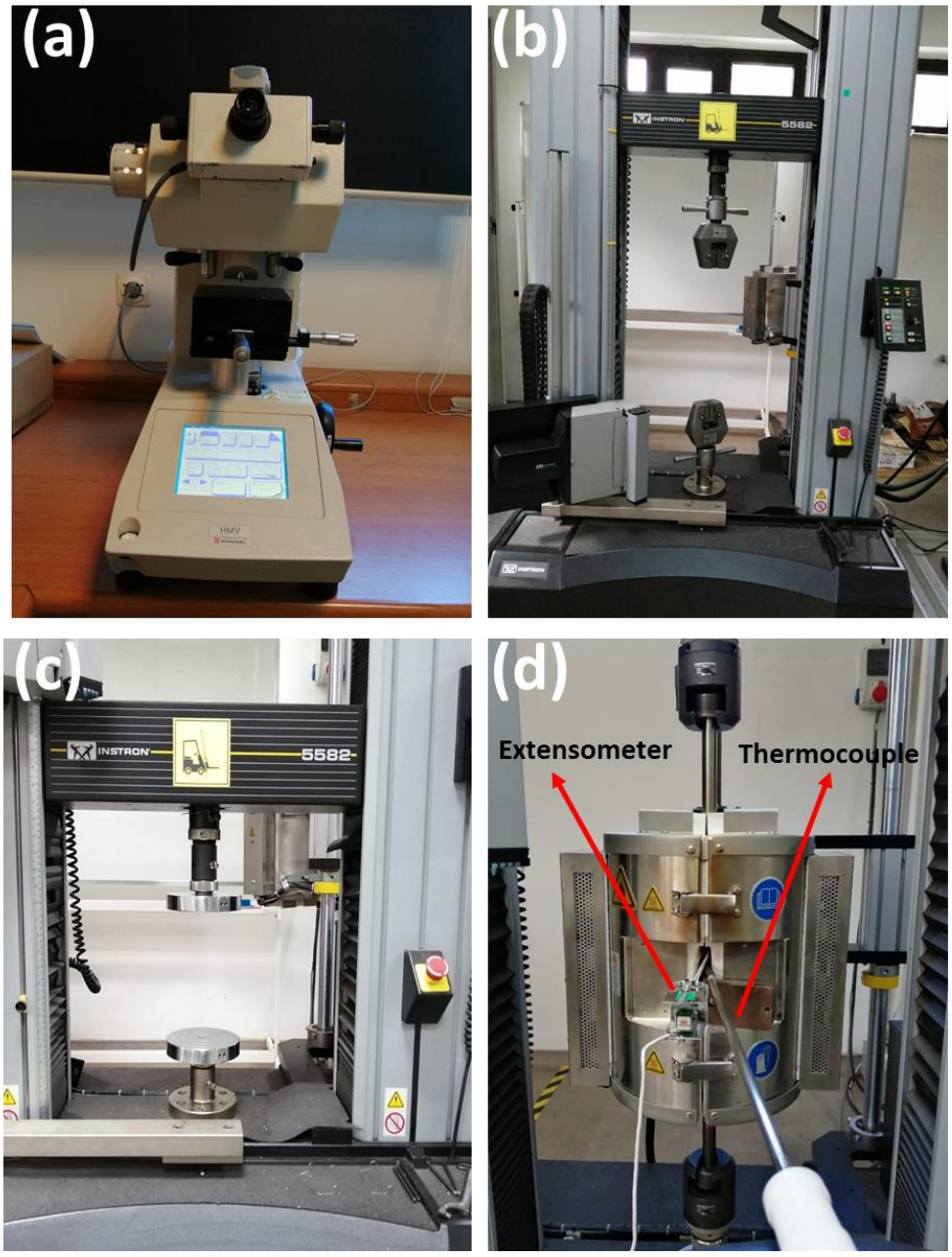

Figure 3. 7 Photographs of (a) HMV Micro Vickers Hardness testing machine, (b) Instron 5582 mechanical testing machine with (b) tension apparatus, (c) compression apparatus, (d) high temperature tension test furnace and related apparatus

CHAPTER 4

RESULTS AND DISCUSSION

4.1 Thermodynamic Calculation Results

The thermodynamic parameters of the FeCoCrNi HEA alloys were determined with respect to Al and Cu content and they are shown in Table 4.1. As it is indicated in the figure, increment of the ratio of Cu in the alloy does not significantly change δ (%). Since ΔH_{mix} of the alloy also increases, the probability of the formation of intermetallic phases decreases. In addition, ΔS_{mix} value increases in the defined value range with the additional Cu. This condition makes the possibility of simple solid solution formation more possible. As mentioned before, it is seen that VEC used to determine the crystal structure of the alloy increases with the increase of Cu. In other words, the alloy moves away from the BCC region and the possibility of forming a FCC structure is further enhanced.

The addition of Al into the main alloy has the opposite effect on thermodynamic parameters compared to that of Cu. In more detail, VEC parameter value increases considerably when the amount of Al is increased in the alloy. This is due to the significant difference between the atomic radius of Al and other alloying elements. As a result, the excess strain energy accumulated in the crystal structure causes deterioration. Moreover, the increment of Al amount gives rise to remarkable decrease in ΔH_{mix} value. As a result, the formation of intermetallic phases can be observed. As shown in the table, Al does not affect significantly ΔS_{mix} of the alloy systems. It can be interpreted by looking at the change in VEC value that the addition of Al can lead to change in the crystal structure of the alloy. As shown in the table, the formation of BCC phase is also expected in addition to FCC phase according to VEC value of the equiatomic FeCoCrNiAl alloy.

Table 4. 1 The thermodynamic parameters and estimated crystal structures of FeCoCrNi, $FeCoNiCu_x$, and $FeCoNiAl_x$ (x: 0.3, 0.6, 1) HEAs

Alloy System	δ (%)	ΔH_{mix} (kJ mol^{-1})	ΔS_{mix} (J K^{-1}mol^{-1})	VEC	Estimated Crystal Structure
FeCoCrNi	1.80	-3.75	11.53	8.25	FCC
$FeCoCrNiCu_{0.3}$	1.77	2.81	12.83	8.44	FCC
$FeCoCrNiCu_{0.6}$	1.74	3.02	13.24	8.61	FCC
FeCoCrNiCu	1.70	3.20	13.38	8.80	FCC
$FeCoCrNiAl_{0.3}$	3.77	-10.60	12.83	7.88	FCC+BCC
$FeCoCrNiAl_{0.6}$	4.69	-11.53	13.24	7.57	FCC+BCC
FeCoCrNiAl	5.40	-12.32	13.38	7.20	FCC+BCC

4.2 VASP Simulation Results

4.2.1 FeCoCrNi HEA

The initial temperature of FeCoCrNi alloy was chosen as 1900 K. Ni element having FCC structure was chosen as the initial crystal structure for this simulation. 3x3x3 supercell, consisting of a total of 108 atoms, was created. 27 atoms of Fe, 27 atoms of Co, 27 atoms of Cr and 27 atoms of Ni are placed by random substitution into the supercell to ensure atomic equality. The default value of plane wave cut-off energy is 269.532 eV. The supercell of FeCoCrNi HEA obtained after the simulation is shown in Figure 4.1 (a) and the XRD pattern of the final structure calculated by the positions of the atoms in the supercell is shown in Figure 4.1 (b). It is seen in the XRD pattern that the crystal structure of the alloy remained as FCC after simulation. The lattice parameter of the alloy was found as 3.534 Å.

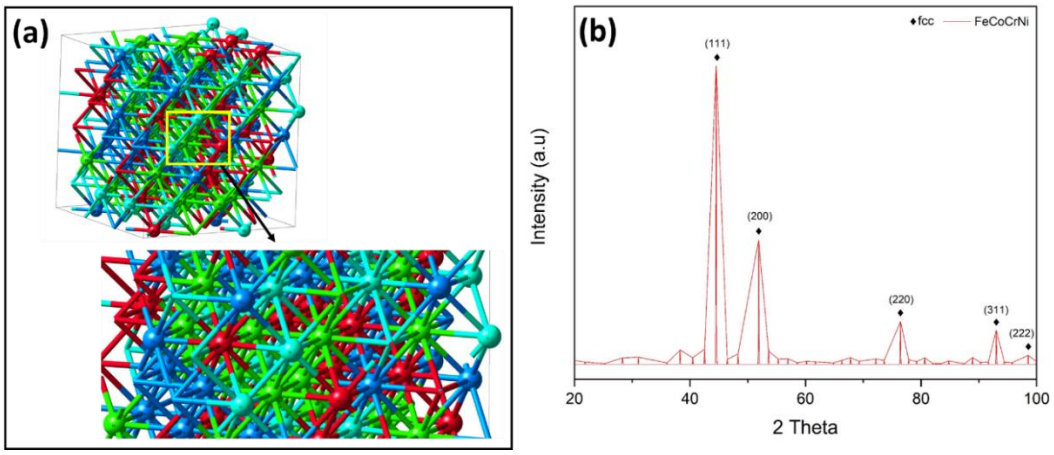

Figure 4. 1 a) The supercell of FeCoCrNi HEA with zoomed region (light blue: Cr, blue: Co, red: Fe and green: Ni) and b) XRD pattern of the alloy after VASP simulation.

4.2.2 FeCoCrNiCu HEA

The initial temperature of FeCoCrNiCu alloy was chosen as 1800 K. Ni element having FCC structure was chosen as the initial crystal structure for this simulation. 5x5x5 supercell, consisting of a total of 500 atoms, was created. 100 atoms of Fe, 100 atoms of Co, 100 atoms of Cr, 100 atoms of Ni and 100 atoms of Cu are placed by random substitution into the supercell to ensure atomic equality. The default value of planewave cut-off energy is 295.446 eV. The supercell of FeCoCrNiCu HEA obtained after the simulation is shown in Figure 4.2 (a) and the XRD pattern of the final structure calculated by the positions of the atoms in the supercell is shown in Figure 4.2 (b). When the XRD graph obtained from simulation is examined, it is seen that peaks belong to FCC diffraction pattern. However, a reflection could not be obtained in (311) plane at $2\theta=91^{o}$ and (222) plane at $2\theta= 96^{o}$. The reason for this situation can be related to insufficient run time of the simulation. Therefore, the simulation time is not long enough to find the exact position of atoms in the crystal structure. However, it can be concluded from the XRD result that the initial crystal structure of the alloy does not be disrupted and the lattice parameter of the alloy was found as 3.522 Å.

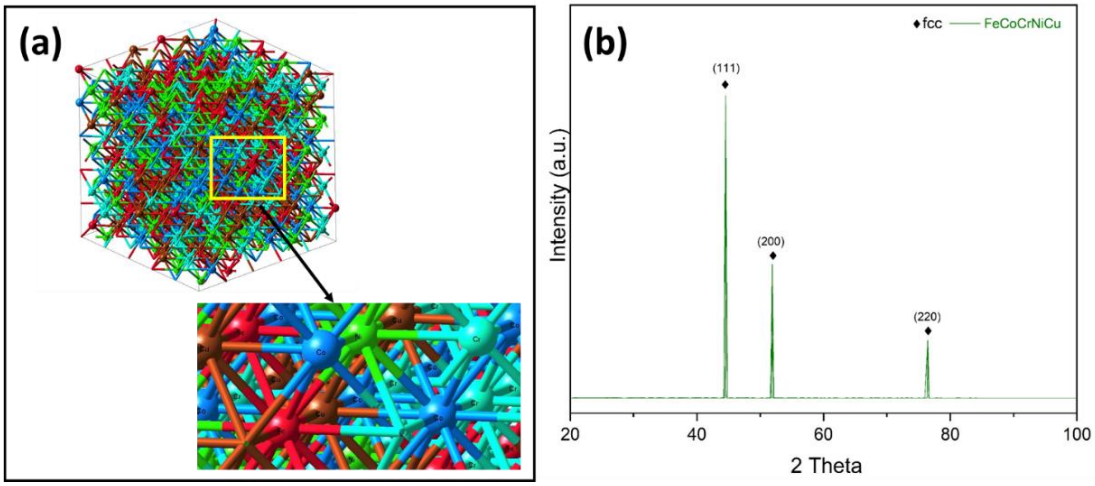

Figure 4. 2 a) The supercell of FeCoCrNiCu HEA with zoomed region (light blue: Cr, blue: Co, red: Fe and green: Ni and brown: Cu) and b) XRD pattern of the alloy after VASP simulation

4.2.3 FeCoCrNiAl HEA

As seen in the previous section, thermodynamic calculations, equiatomic FeCoCrNiAl alloy is expected to contain both FCC and BCC phases. Since the single phase is given as input to the simulation program, the simulation of the binary phases is unfortunately not possible. However, as the amount of Al is increased, VEC value of the alloy is very close to the single-phase BCC region. Therefore, the crystal structure of the alloy is assumed to be BCC and Cr element having BCC structure was chosen as the initial crystal structure for this simulation. The initial temperature of FeCoCrNiAl alloy was chosen as 1700 K. 5x5x5 supercell, consisting of a total of 250 atoms, was created. 50 atoms of Fe, 50 atoms of Co, 50 atoms of Cr, 50 atoms of Ni and 50 atoms of Al are placed by random substitution into the supercell to ensure atomic equality. The default value of planewave cut-off energy is 269.532 eV. The supercell of FeCoCrNiAl HEA obtained after the simulation is shown in Figure 4.3 (a) and the XRD pattern of the final structure calculated by the positions of the atoms in the supercell is shown in Figure 4.3 (b). It is seen in the XRD pattern

that the crystal structure of the alloy remained as BCC after simulation. The lattice parameter of the alloy was found as 2.881 Å.

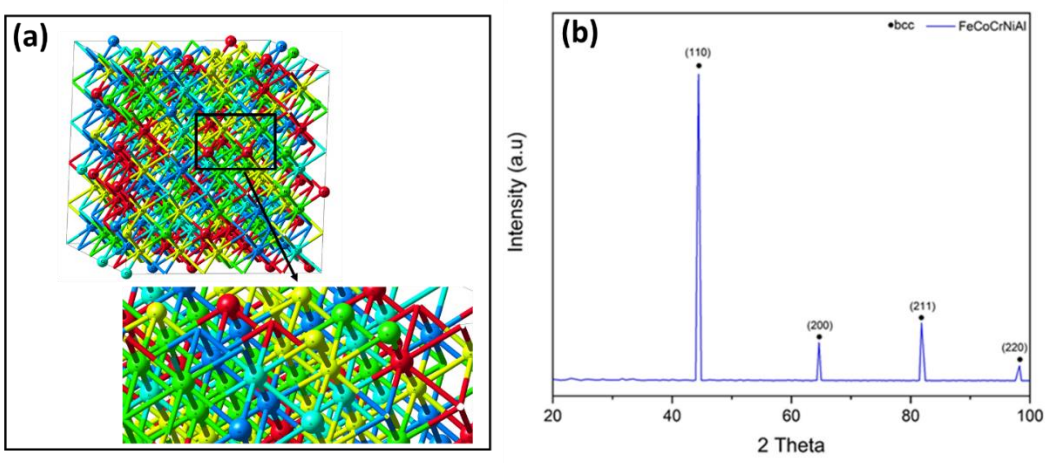

Figure 4. 3 a) The supercell of FeCoCrNiAl HEA with zoomed region (light blue: Cr, blue: Co, red: Fe, green: Ni and yellow: Al) and b) XRD pattern of the alloy after VASP simulation

4.3 Ambient and High Temperature X-ray Diffraction Results

Figures 4. 4 (a) and (b) show the XRD profiles of as-cast impure $FeCoCrNiCu_x$ and pure $FeCoCrNiCu_x$ (x: 0,0.3,0,6 and 1) alloys. According to the results, the main alloy, pure FeCoCrNi HEA, has FCC crystal structure. The result is consistent with the results of other researchers [2-3]. On the other hand, impure FeCoCrNi HEA includes Cr_7C_3 phase with FCC phase. This is due to the fact that carbon (C) impurities originated from FeCr. Moreover, low alloy carbon steel that we used for the production of this alloy promotes the formation of Cr_7C_3 phases. The addition of Cu in different proportions to the main alloy has no effect on the change of crystal structure for both pure and impure alloys. The reason is that atomic radius of Fe, Co, Cr, Ni and Cu (1.411Å, 1.385Å, 1.423Å, 1.377 Å and 1.413 Å, respectively) is pretty close to each other [69].

This is also introduced by Hume-Rothery rules described in Section 2.5. When the difference in atomic diameters of the elements is less than 15 percent, formation of

a solid solution is promoted. Figure 4.5 (a) shows XRD peak shift of the (200) reflections for pure Cu_0-$Cu_{1.0}$ alloys. As seen that increasing Cu in the main alloy did not cause a serious shift in (200) reflection peaks. It can be said that the addition of Cu element does not have a significant effect on the crystal structures of the HEAs.

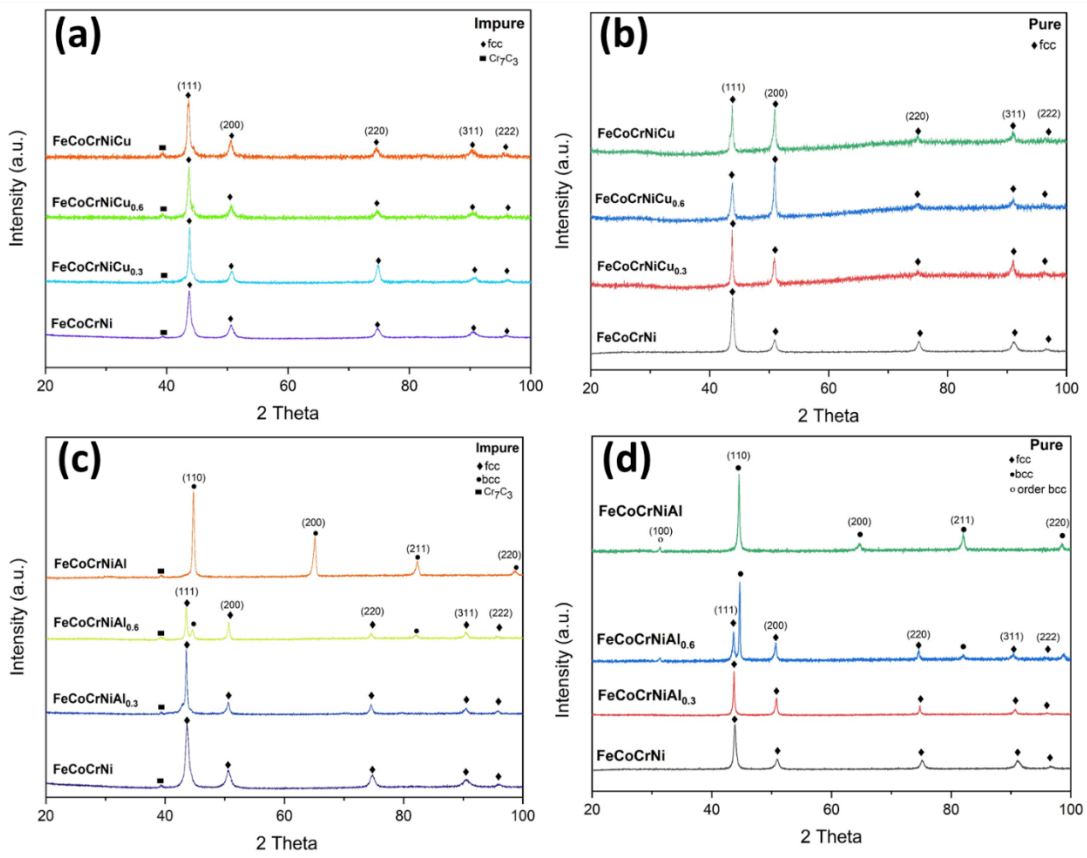

Figure 4. 4 XRD patterns of as-cast (a) impure, (b) pure $FeCoCrNiCu_x$ (c) impure and (d) pure $FeCoCrNiAl_x$ (x:0,0.3,0,6 and 1) alloys

Figure 4.4 (c) and (d) show the XRD profiles of as-cast impure $FeCoCrNiAl_x$ and pure $FeCoCrNiAl_x$ (x: 0,0.3,0,6 and 1) alloys. When the XRD profiles of pure alloys are examined, $Al_{0.3}$ alloy has FCC crystal structure as in the main alloy. However, (110) and (211) reflection BCC peaks and (100) reflection minor ordered BCC starts to form in the $Al_{0.6}$ alloy. In pure $Al_{1.0}$ alloy, it is seen that FCC peak reflections disappeared completely. In addition, ordered BCC of $(100)_{BCC\text{-}ordered}$ reflection peak

is observed at approximately 25°. A study conducted by Wang et al. [4] has similar conclusions that equiatomic FeCoCrNiAl contains disordered BCC phase plus B2 phase. The fact that the crystal structure of the material transforms from FCC to BCC is valid for impure $Al_{(0.3\text{-}1.0)}$ alloys. The formation of Cr_7C_3 phase was also observed in these alloys. Fig. 4.5 (b) shows XRD peak shift of the (200) reflections for pure Al_0- $Al_{0.6}$ alloys. The peak position shifts to lower angles by increasing the ratio of Al in the alloy. This is due to the fact that the atomic radius of Al in 1.582 Å is substantially larger than the other elements in the alloy. When Al atom is embedded in the FCC crystal structure of the main alloy, it causes the formation of excess strain energy in the crystal structure. Al also makes a strong cohesive bond with other elements [18]. The shift of the peaks to the left causes the increment of interplanar spacing which enables to annihilate excess strain energy in the crystal structure. Consequently, the crystal structure of the alloy transforms into BCC that is more open than the FCC structure [71]. In addition, the formation of ordered BCC phase occurred in pure $Al_{0.6}$ and $Al_{1.0}$ alloys. This is due to the spinodal decomposition of the BCC phase into disordered BCC (A2) and ordered BCC (B2) phases at high temperatures [72]. On the contrary, in impure $Al_{1.0}$ alloy, it can be interpreted that the solidification temperature is not below the critical temperature of the spinodal decomposition. At the same time, Guo et al. [72] and Wang et al. [4] confirm that the formation of ordered BCC in the alloys obtained by melting with arc furnace is related to the VEC value. However, it can be speculated that Cr_7C_3 may suppress the formation of ordered BCC in impure alloys. In conclusion, as understood from all

the data, increasing the amount of Al in the main alloy causes significant changes in the crystal structure of the alloys.

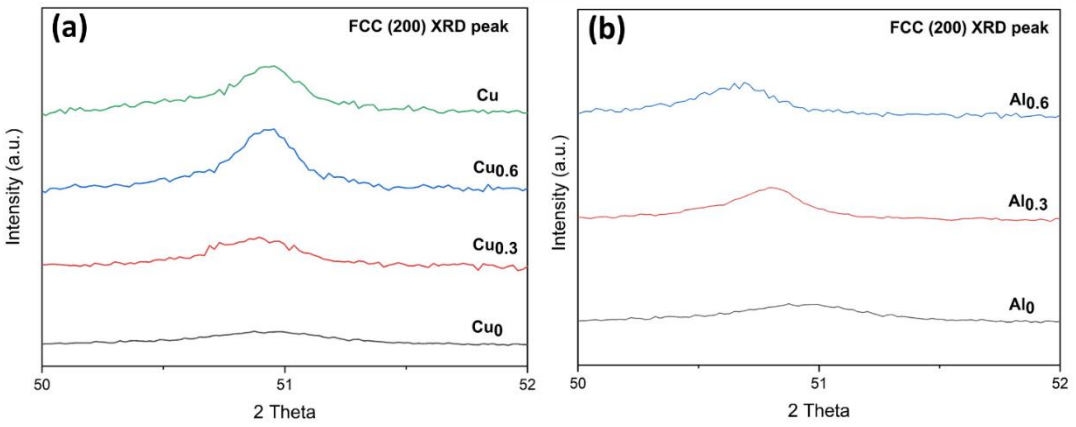

Figure 4. 5 Shift of the XRD peaks in pure FeCoCrNiCu and FeCoCrNiAl alloys: (a) (200) reflections of Cu_0-$Cu_{1.0}$ alloys and (b) (200) reflections of Al_0 - $Al_{0.6}$ alloys.

Table 4.2 shows the lattice parameters and phases of the alloys obtained from VASP simulation and experimental method. VASP simulations were applied for the equiatomic alloys, FeCoCrNi, FeCoCrNiCu and FeCoCrNiAl. Since the initial crystal structure was defined in the initial stage of the simulation program, it was unfortunately not possible to simulate two-phase alloys. The main purpose of the simulation is to determine whether the expected crystal structure is destroyed or not at the end of the simulation. The lattice parameter values of FeCoCrNi and FeCoCrNiCu calculated from VASP simulations are smaller than those calculated experimentally. The reason is that atomic simulation is performed on a perfect crystal structure on the other hand experimentally produced alloys most probably contain impurities. Although these impurity atoms entering the crystal structure do not cause the deterioration of the crystal structure, they can lead to lattice distortion at a certain degree. Therefore, the lattice parameter values obtained experimentally are higher than the values obtained by atomic simulation. As seen in the table, the lattice parameter values of the impure alloys are higher than those of pure alloys. It can be concluded that although the amounts of Al and Si elements are very small in the alloys their atoms cause a lattice strain effect in the crystal structure.

As the amount of copper element was added into FeCoCrNi HEA, the lattice parameter was decreased gradually. The change of Cu amount in the alloy also causes the change in peak densities due to the lattice distortion which is related to their atomic size [73]. However, since the lattice distortion is not high, the crystal structure remains FCC.

The effect of Al on the lattice parameter seen in the table is that the lattice parameter of the pure and impure alloys is increased with the addition of Al. As discussed above, the atomic radius of the Al is larger than the other alloy elements, so the crystal structure accumulates significant amount of strain energy. Solute atoms with higher atomic radius such as Al can enter BCC structure more easily due to its lower atomic packing density (68%) compared to FCC and hexagonal close packed (HCP) structures (both 74%). As a conclusion, Al induces the transformation of the alloy from FCC structure to BCC structure in HEAs in order to eliminate lattice distortion energy [4].

Table 4. 2 The lattice parameters and phases of the alloys obtained from VASP simulation and experimental method.

Alloy System	Simulation		Experimental	
	Lattice Parameter (Å)	*Phase(s)*	*Lattice Parameter (Å)*	*Phase(s)*
FeCoCrNi-Pure	3.534	FCC	3.586	FCC
FeCoCrNi-Impure	-	-	3.589	FCC+ Cr_7C_3
FeCoCrNiCu$_{0.3}$-Pure	-	-	3.585	FCC
FeCoCrNiCu$_{0.3}$-Impure	-	-	3.588	FCC+ Cr_7C_3
FeCoCrNiCu$_{0.6}$-Pure	-	-	3.583	FCC
FeCoCrNiCu$_{0.6}$-Impure	-	-	3.586	FCC+ Cr_7C_3
FeCoCrNiCu-Pure	3.522	FCC	3.581	FCC
FeCoCrNiCu-Impure	-	-	3.583	FCC+ Cr_7C_3
FeCoCrNiAl$_{0.3}$-Pure	-		3.593	FCC
FeCoCrNiAl$_{0.3}$-Impure	-	-	3.597	FCC+ Cr_7C_3
FeCoCrNiAl$_{0.6}$-Pure	-		3.599(FCC) 2.868(BCC)	FCC+BCC+ordered BCC
FeCoCrNiAl$_{0.6}$-Impure	-	-	3.600 (FCC) 2.872 (BCC)	FCC+ Cr_7C_3
FeCoCrNiAl-Pure	2.881	BCC	2.861	BCC+ordered BCC
FeCoCrNiAl-Impure	-	-	2.865	BCC + Cr_7C_3

Figure 4.6 shows the change in VEC calculated using equation 2.9 relative to Al and Cu in $(FeCoCrNi)_{100-x}Al_x$ and $(FeCoCrNi)_{100-x}Cu_x$ alloys. According to this graph,

the addition of Cu element increased gradually VEC value and kept the material in FCC region. This situation has been proved by experimental and simulation methods. On the other hand, increasing the amount of Al in the alloy decreases linearly VEC value. As seen in the figure, the alloy containing approximately 5 at. % Al is located in FCC region, and the alloy containing between 5 to 26 at. % Al is located in FCC and BCC region and also the alloy containing above 26 at. % is observed in BCC region. This decrease can be interpreted as strengthening of cohesive bonding between Al and other elements. Although VEC criterion provides a wider boundary condition to obtain single FCC and BCC solid solution phases, the pure FeCoCrNiAl HEA containing 20 at. % Al has BCC and ordered BCC crystal structure in the experimental results. The reason for the difference is that in addition to atomic bond between elements, other parameters are also important in the phase formation of HEAs including Al. Therefore, a more detailed description of VEC especially for the HEA containing Al is necessary to better estimate the phase formation.

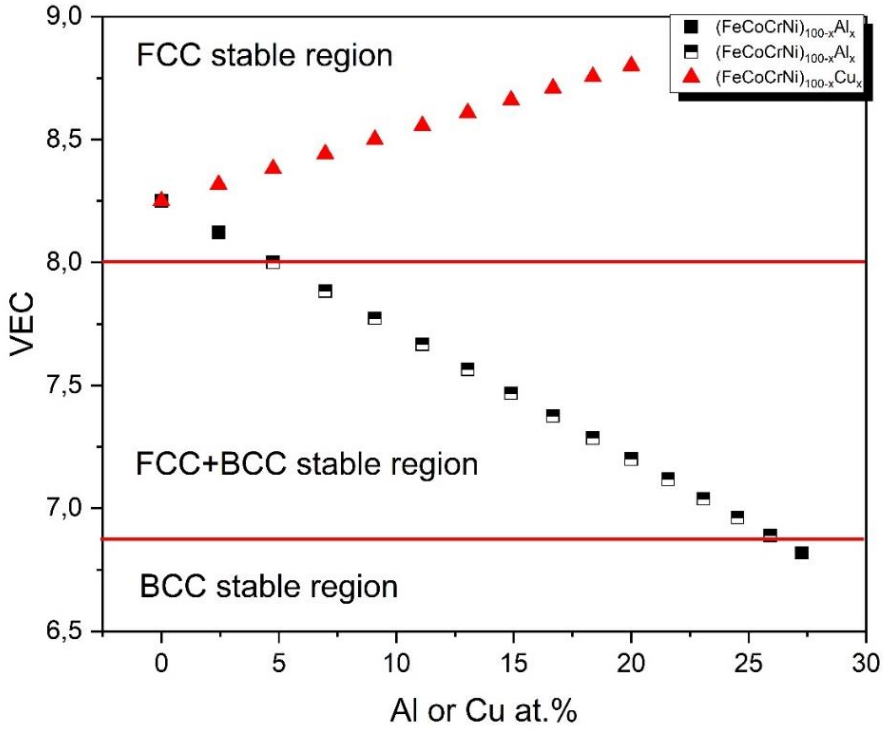

Figure 4. 6 The value of VEC as a function of Al and Cu content in (FeCoCrNi)100-xAlx and (FeCoCrNi)100-xCux alloys.

Figure 4.7 shows high temperature XRD graph of impure FeCoCrNi HEA. Data were collected from room temperature (298 K) to 1373 K under protective atmosphere. The graph indicates that the crystal structure of the alloy does not change with the temperature change. It is also observed that Cr_7C_3 intermetallic maintains its stability in every temperature range. These results actually prove the concept of HEAs. As it is known, the crystal structure of many materials is destroyed and intermediate phases are formed at high temperatures. However, there have been changes in peak width. As the temperature increases, the peak with decreases gradually and takes a sharp shape. The decrease in peak width can be interpreted as increment in crystallite size [74].

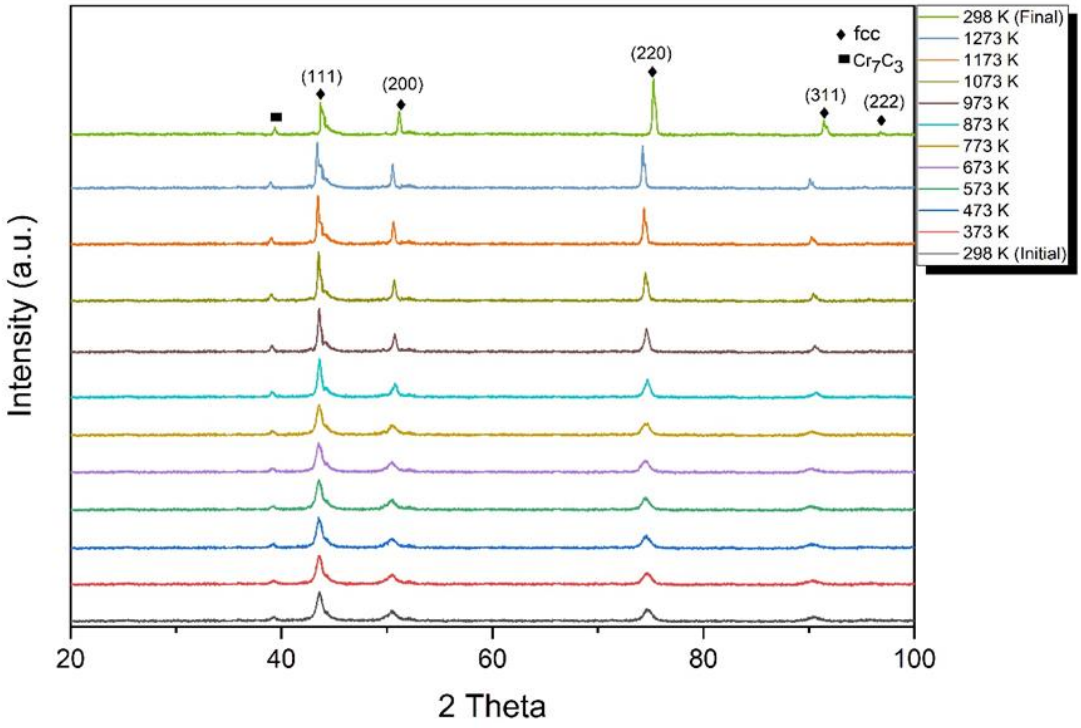

Figure 4. 7 High temperature XRD graph of impure FeCoCrNi HEA

4.4 Scanning Electron Microscopy Analyses

The chemical compositions of all pure and impure alloys are given in Table 4.3. Figure 4.8 shows the microstructures of impure and pure FeCoCrNi alloys under SEM. Impure FeCoCrNi alloy shown in Figure 4.8 (a) and (b) has columnar dendrite structure. The microstructure of pure FeCoCrNi alloy with FCC structure shown in Figure 4.8 (c) and (d) is composed of columnar grains. It is known that industrial raw materials contain Al, Si and C impurities in addition to desired elements. Although, quantitative observation of C by EDS is not possible due to its low atomic number, high intensity C peaks are observed in the raw materials.

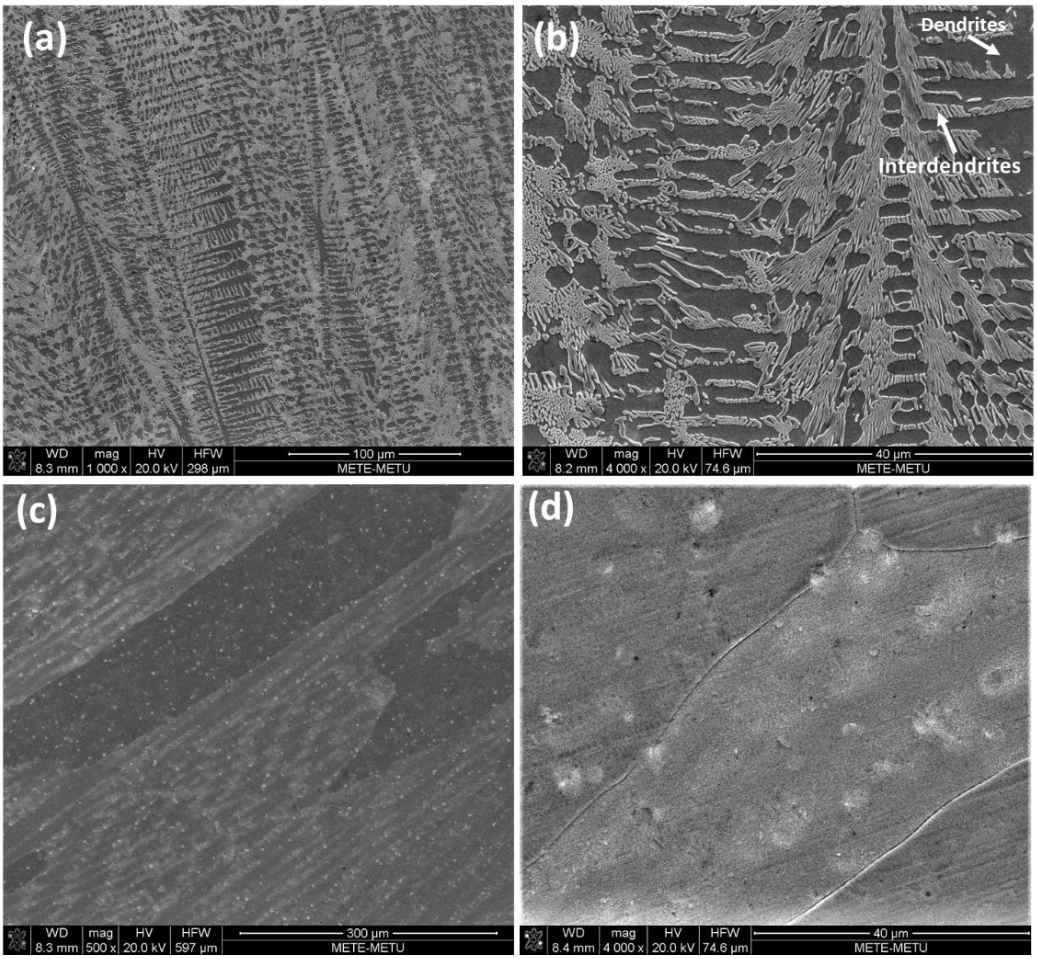

Figure 4. 8 SEM images of (a) the impure FeCoCrNi (1000x), (b) the impure FeCoCrNi, (4000x), (c) the pure FeCoCrNi (500x), (d) the pure FeCoCrNi (4000x)

As shown in Figure 4.8 (b), the interdendrite region, which consists of fine-size structure, appears as bright, while the dendrite region appears as dark. It is shown in Table 4.3 that bright fields have 36.6 (at %) Cr, although there are 12.3 (at %) Cr and. It proves that Cr reacts with C to form Cr_7C_3 secondary phases. Therefore, bright fields of impure FeCoCrNi alloy consist of Cr_7C_3 phases.

Table 4.3 EDS analysis of produ[c]ed as-cast impure and pure $FeCoCrNiCu_x$ and $FeCoCrNiAl_x$ (x: 0, 0.3, 0.6 and 1) alloys

		Chemical composition /at. %						
		Fe	**Co**	**Cr**	**Ni**	**Cu**	**Al**	**Si**
Impure	**FeCoCrNi**	24.51	24.59	24.22	25.00	-	0.56	1.12
	$FeCoCrNiCu_{0.3}$	22.74	23.07	21.26	22.90	8.65	0.64	0.73
	$FeCoCrNiCu_{0.6}$	20.8	20.83	21.80	21.10	14.01	0.77	0.78
	FeCoCrNiCu	19.12	19.94	20.20	19.51	19.50	0.94	0.80
	$FeCoCrNiAl_{0.3}$	22.93	22.74	22.46	22.84	-	7.73	1.30
	$FeCoCrNiAl_{0.6}$	22.02	21.61	22.02	21.12	-	12.49	0.75
	FeCoCrNiAl	19.75	19.4	19.94	19.60	-	20.44	0.86
Pure	**FeCoCrNi**	25.34	24.71	24.37	25.58	-	-	-
	$FeCoCrNiCu_{0.3}$	23.48	23.12	23.19	23.30	6.91	-	-
	$FeCoCrNiCu_{0.6}$	21.38	21.63	21.67	22.17	13.15	-	-
	FeCoCrNiCu	19.92	19.88	19.74	20.4	20.07	-	-
	$FeCoCrNiAl_{0.3}$	23.27	23.38	23.06	23.25	-	7.05	-
	$FeCoCrNiAl_{0.6}$	21.59	21.25	21.75	21.25	-	13.96	-
	FeCoCrNiAl	20.2	20.1	20.03	19.92	-	19.75	-

As seen from Figure 4. 9 and Figure 4. 10, the microstructures of pure and impure $Cu_{0.3}$, $Cu_{0.6}$ and $Cu_{1.0}$ have dendrite and interdendrite structure. The overall chemical compositions of $Cu_{0.3}$, $Cu_{0.6}$ and $Cu_{1.0}$ alloys are very close to the expected nominal compositions as shown in Table 4.3. This means that the elements in the alloy constitute substitutional solid solutions.

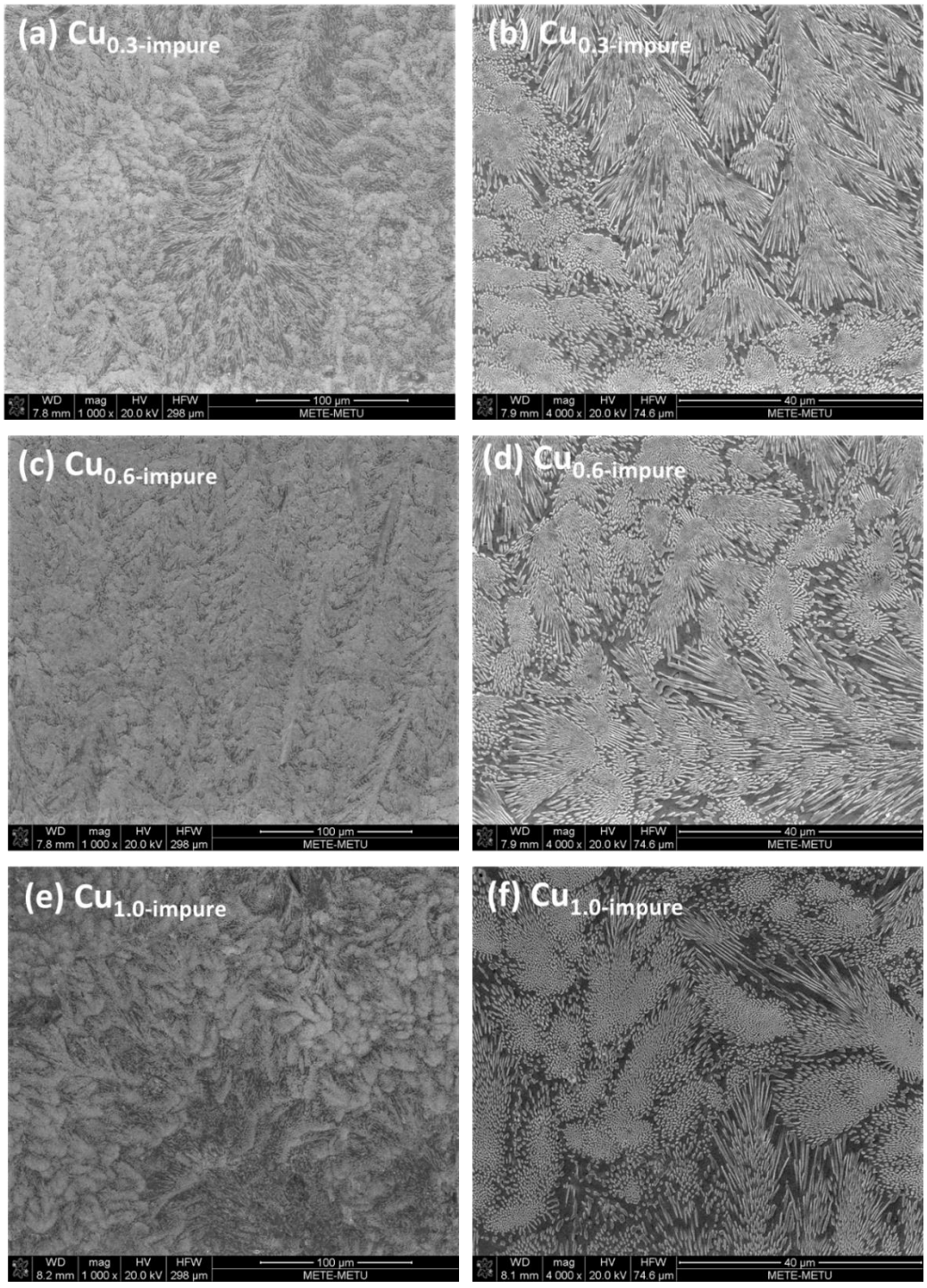

Figure 4. 9 SEM images of (a) the impure $FeCoCrNiCu_{0.3}$ (1000x), (b) the impure $FeCoCrNiCu_{0.3}$ (4000x), (c) the impure $FeCoCrNiCu_{0.6}$ (1000x), (d) the impure $FeCoCrNiCu_{0.6}$ (4000x), (e) the impure $FeCoCrNiCu_{1.0}$ (1000x), (f) the impure $FeCoCrNiCu_{1.0}$ (4000x)

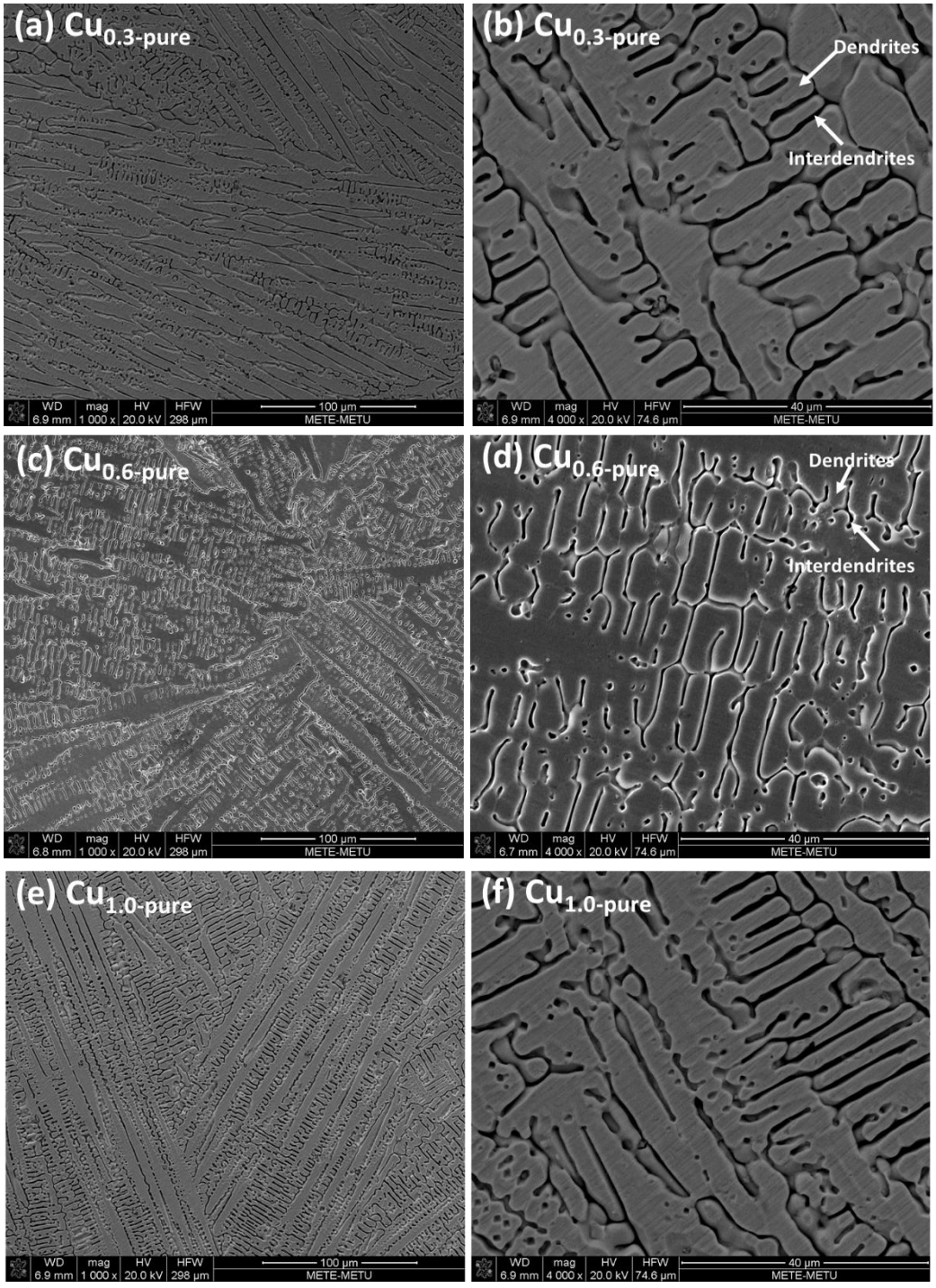

Figure 4. 10 SEM images of (a) the pure $FeCoCrNiCu_{0.3}$ (1000x), (b) the pure $FeCoCrNiCu_{0.3}$ (4000x), (c) the pure $FeCoCrNiCu_{0.6}$ (1000x), (d) the pure $FeCoCrNiCu_{0.6}$ (4000x), (e) the pure $FeCoCrNiCu_{1.0}$ (1000x) (f) the pure $FeCoCrNiCu_{1.0}$ (4000x)

Table 4. 4 EDS analysis (at.%) of the dendrite and interdendrite structure of as-cast impure and pure $FeCoCrNiCu_x$ (x: 0, 0.3, 0.6 and 1) alloys

	Impure								**Pure**					
	FeCoCrNi		**$Cu_{0.3}$**		**$Cu_{0.6}$**		**$Cu_{1.0}$**		**$Cu_{0.3}$**		**$Cu_{0.6}$**		**$Cu_{1.0}$**	
	ID	**D**	**ID**	**D**	**ID**	**D**	**ID**	**D**	**ID**	**D**	**ID**	**D**	**ID**	**D**
Fe	24.9	27.7	7.8	20.9	8.4	20.1	8.4	20.9	7.9	22.9	9.2	21.9	7.7	22.5
Co	21.9	28.3	8.6	19.7	6.50	18.6	9.8	19.7	11.2	21.1	7.6	22.0	10.1	22.6
Cr	36.6	12.3	3.4	37.9	2.9	41.5	2.4	27.9	1.9	22.1	2.3	23.5	2.5	23.3
Ni	16.4	30.6	22.7	14.4	23.1	12.0	16.8	23.1	20.9	23.0	19.6	21.6	17.5	21.2
Cu			57.0	6.9	57.6	7.0	62.5	7.91	57.4	11.7	61.6	9.8	66.2	10.3
Si		0.90	0.49		1.31		0.11							

D: dendrite, ID: interdendrite

The chemical compositions of dendrite (D) and interdendrite (ID) regions of $FeCoCrNiCu_x$ alloys are given in Table 4.4. Homogeneous chemical distribution of other constituent elements, Fe, Co, Cr and Ni in the dendrite regions was observed for pure $Cu_{0.3}$, $Cu_{0.6}$ and $Cu_{1.0}$ alloys. However, there is no homogeneous chemical distribution in the interdendrite regions and Cu is very rich in these regions. When the impure $Cu_{0.3}$, $Cu_{0.6}$ and $Cu_{1.0}$ alloys are examined, the dendrite and interdendrite structures became different from the pure ones. The majority of the structure consists of interdendritic structure. In impure $FeCoCrNiCu_x$ alloys, Cu is rich in interdendrite regions in contrast to the main alloy. It is seen that the field density of the interdendrite regions (bright fields for impure alloys, dark fields for pure alloys) significantly increased with the addition of Cu. Since the amount of Cu increases in the alloy, the amount of Cu precipitation increases gradually. The reason for this case is that, the bonding force described as mixing enthalpy ΔH^{mix} (kj mol^{-1}) of Cu with other constituent elements is weaker than the other Fe, Co, Ni and Cr as indicated in Table 4.5 [75]. In other words, if ΔH^{mix} value of atomic pairs of elements are more negative, these elements are likely to form intermediate phase. Conversely, in positive ΔH^{mix} values, precipitation in the alloy which is related to phase separation is observed.

Table 4. 5 Mixing enthalpy ΔH^{mix} (kj mol^{-1}) of atomic pairs. Adopted from [75]

	ΔH^{mix} (kj mol^{-1})
Cu-Fe	13
Cu-Co	10
Cu-Ni	4
Co-Ni	0
Cu-Cr	-1
Fe-Co	-1
Fe-Cr	-1
Fe-Ni	-2
Co-Cr	-4
Ni-Cr	-7

The addition of Al into FeCoCrNi alloy shows the evolution of the microstructures of both impure and pure alloys as seen in Figure 4.11 and Figure 4.12 respectively. As a result of the addition of Al into the main alloy, it was observed that the dendrite structure changed as a certain extent. The impure $Al_{0.3}$ alloy has dendritic structure, but the interdendrities have become more plate-like structure as shown in Figure 4.11 (a) and (b). The pure $Al_{0.3}$ alloy is composed of columnar grains as shown in Figure 4.12 (a) and (b). According to the EDS results of the pure $Al_{0.3}$ alloy shown in Table 4.3 , elements were homogeneously dispersed in the structure. However, when the chemical composition distribution of the impure $Al_{0.3}$ alloy shown in Table 4.6 is examined, it is understood that dendrite regions are rich in Cr, so Cr_7C_3 phase is present in the dendrite region.

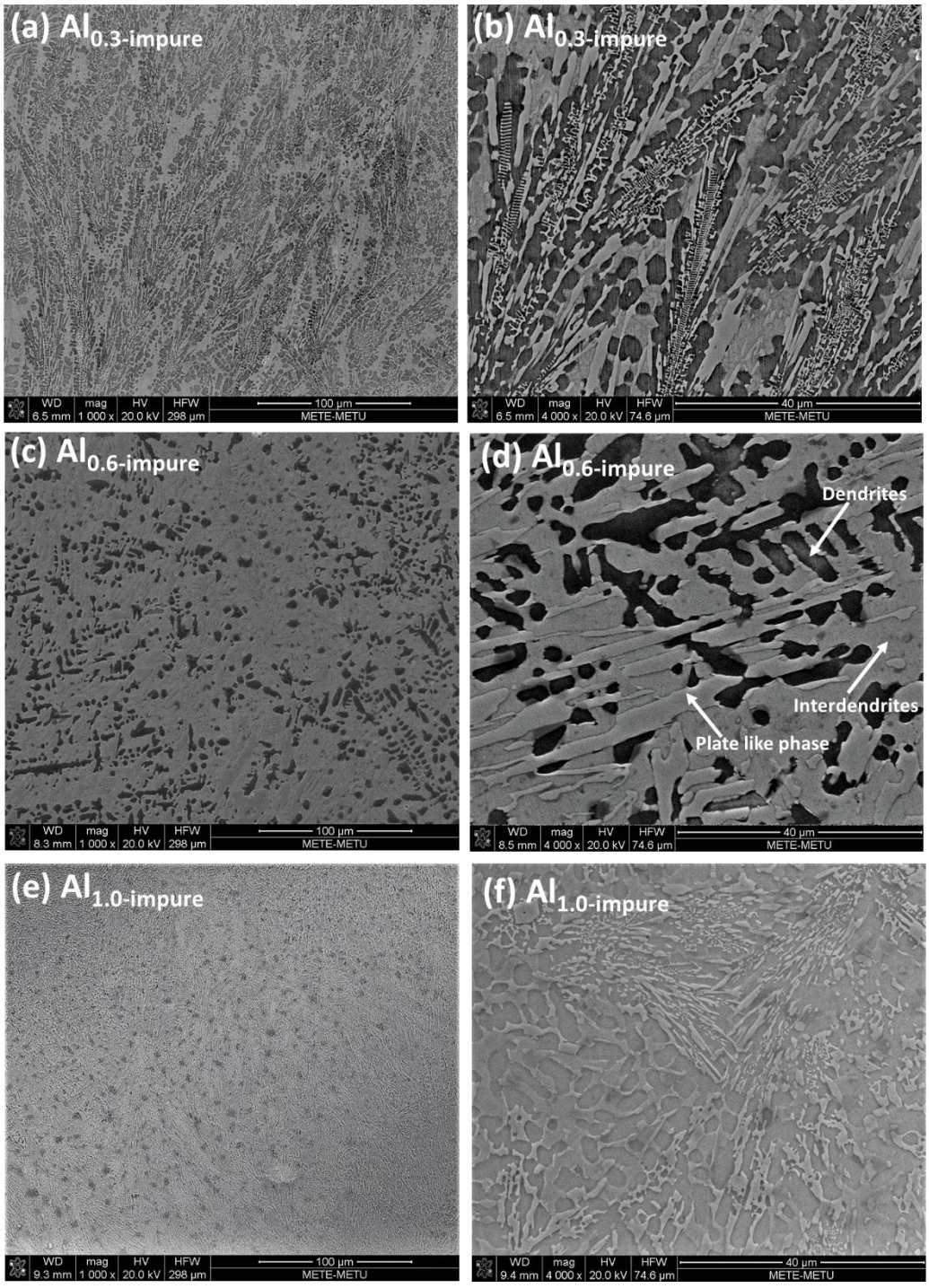

Figure 4. 11 SEM images of (a) the impure $FeCoCrNiAl_{0.3}$ (1000x), (b) the impure $FeCoCrNiAl_{0.3}$ (4000x), (c) the impure $FeCoCrNiAl_{0.6}$ (1000x), (d) the impure $FeCoCrNiAl_{0.6}$ (4000x), (e) the impure $FeCoCrNiAl_{1.0}$ (1000x), (f) the impure $FeCoCrNiAl_{1.0}$ (4000x)

Table 4. 6 EDS analysis (at.%) of different regions of as-cast impure and pure $FeCoCrNiAl_x$ alloys

	Impure							Pure				
	$Al_{0.3}$		$Al_{0.6}$			$Al_{1.0}$		$Al_{0.6}$			$Al_{1.0}$	
	ID	**D**	**ID**	**D**	**PP**	**ID**	**D**	**ISP**	**SP**	**B**	**ID**	**D**
Fe	17.8	23.0	15.6	24.8	23.5	17.8	20.5	19.7	22.1	13.8	21.6	15.6
Co	25.0	19.7	22.4	26.6	20.0	19.4	18.1	21.3	23.8	15.4	19.9	21.0
Cr	10.7	39.5	2.6	8.9	32.1	3.8	38.3	23.7	22.3	14.3	22.5	12.7
Ni	27.3	13.8	32.6	26.4	16.5	27.6	11.6	18.9	20.6	27.6	17.9	24.3
Al	15.0	3.7	26.4	13.4	7.8	30.9	9.5	16.4	11.2	28.9	18.0	26.4
Si	1.76	0.25	1.35									

D: dendrite, ID: interdendrite, PP: plate like phase, SP: side plate, ISP: inter-side plate, B: boundary between SP and ISP.

The microstructure of the impure $Al_{0.6}$ alloys shown in Figure 4.11 (c) and (d) consists of both dendrites, interdendrites and plate like structures. As shown in Table 4.6, the amount of Cr is more and Al and Ni are less than the expected composition of the alloy in the plate like region. It can be concluded that Cr_7C_3 phase is present in this region. On the other hand, interdendritic regions contain high amount of Al and Ni. Compared to the microstructure of the impure $Al_{0.3}$ alloy, Cr is concentrated in the plate like regions as opposed to dendritic regions.

The microstructures of the pure $Al_{0.6}$ alloys shown in Figure 4.12 (c) and (d) have non-dendrite structure. This shows that the solidification temperature range is quite narrow. In the microstructure of pure $Al_{0.6}$ alloy, long Widmanstatten side plates (bright region) formed along grain boundary regions were observed. The EDS result of pure $Al_{0.6}$ alloy in the side plate region is almost close to the expected composition. However, in the inter-side region, the amount of Al increased by a certain amount as in the case of the impure $Al_{0.6}$ alloy. Particularly in EDS taken from grain boundary, the proportions of Ni and Al have increased significantly. Al containing FeCoCrNi alloy has been widely studied in the literature. One of them which is related to the effect of Al addition into FeCoCrNi alloy on microstructural and mechanical properties, carried out by Wang et al. [4]. In this study, the crystal structures of the

phases in the microstructure were determined by using TEM. According to this study, FCC phase is formed in the side-plate region, while spinodal decomposition occurred in the inter-sideplate regions induces the formation of disordered BCC (A2) and ordered BCC (B2) phases. The higher atomic amounts of Al and Ni in the grain boundaries indicate that the spinodal decomposition temperature is further decreased. The atoms of these elements pushed further by the side-plate area, result in the formation of grain boundaries with disordered BCC (A2) phase.

The microstructure of the impure $Al_{1.0}$ alloy shown in Figure 4.11 (e) and (f) consists of both equiaxed dendritic and plate like interdendritic structures. Compared to the microstructure of the impure $Al_{0.3}$ alloy, dendrite region area was increased. As in the impure $Al_{0.3}$ alloy, interdendrite regions have higher atomic percentages of Al and Ni and dendrite region is rich in Cr.

The solidification structure of the pure $Al_{1.0}$ alloy includes flower like dendritic and interdendrite regions as shown in Figure 4.12 (e) and (f). It can be inferred from the microstructure that the solidification temperature range of the alloy is larger on the contrary to that of the pure $Al_{0.6}$ alloy. As given in Table 4.6, the amount of Al and Ni in the dendrite regions (dark fields) of the pure $Al_{1.0}$ alloy is higher than the interdendrite region (bright fields). According to literature, both dendrites and interdendrites have BCC and ordered BCC (B2) phases [4].

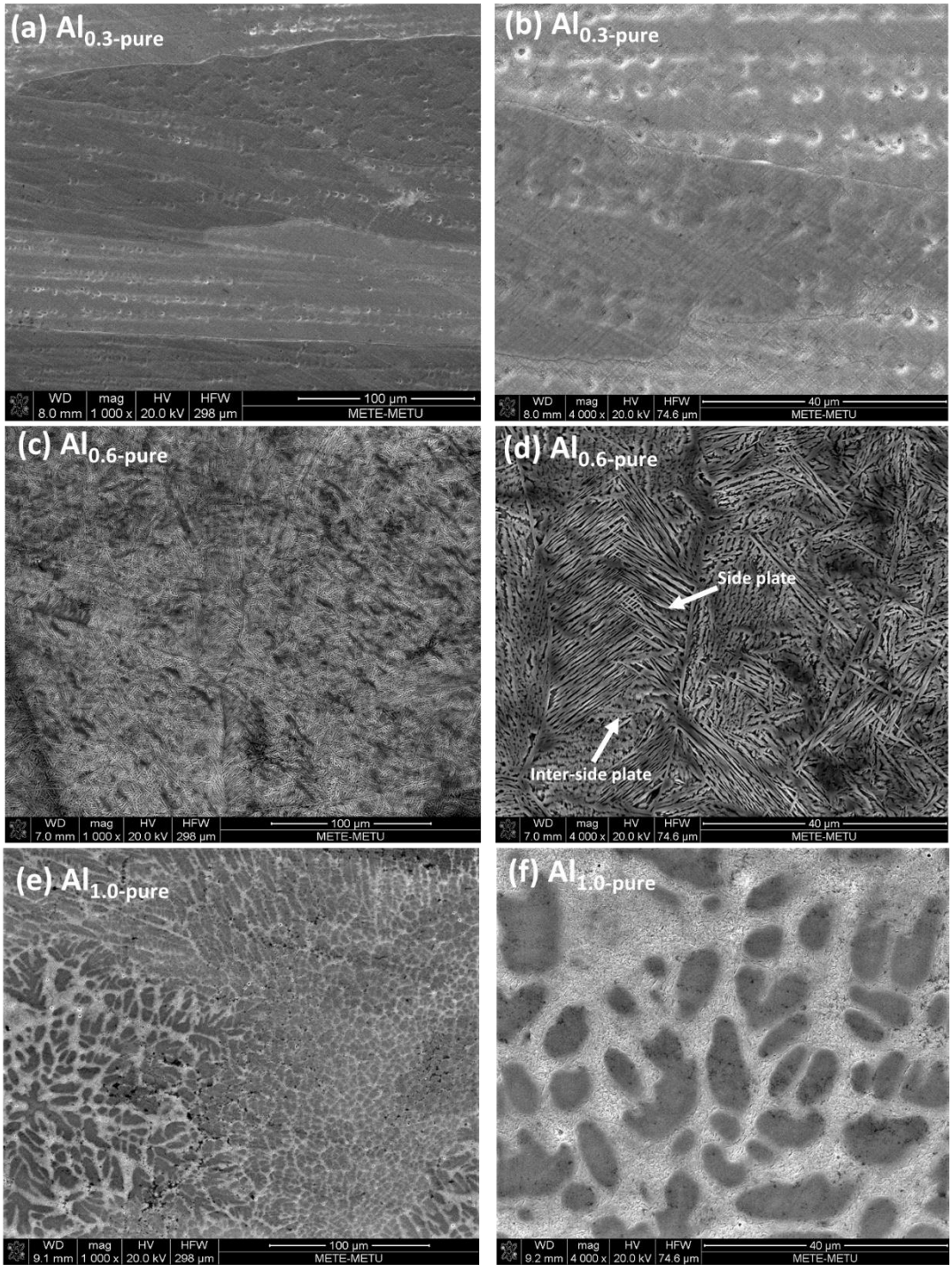

Figure 4. 12 SEM images of (a) the pure $FeCoCrNiAl_{0.3}$ (1000x), (b) the pure $FeCoCrNiAl_{0.3}$ (4000x), (c) the pure $FeCoCrNiAl_{0.6}$ (1000x), (d) the pure $FeCoCrNiAl_{0.6}$ (4000x), (e) the pure $FeCoCrNiAl_{1.0}$ (1000x), (f) the pure $FeCoCrNiAl_{1.0}$ (4000x)

4.5 Transmission Electron Microscopy (TEM) Analyses

It is not possible to collect the real composition of the phase in EDS due to additional elemental EDS spectrums coming from the dendrite region. Therefore, TEM technique is used to investigate the specific composition. As shown in Figure 4.13, bright field images of impure FeCoCrNi HEA consist of two main regions; Region A and Region B. The elemental analyses show that Region A contains approximately 70 % at Cr (a band region composed of Cr_7C_3 intermetallic). This is additional information to prove the presence of the Cr_7C_3 intermetallic phase besides XRD. Elemental analysis of Region B shows that the atomic distribution of each element is in the limit of ability of HEA. In the light of the XRD and EDS analysis by TEM, the Region B is the field of impure FeCoCrNi HEA.

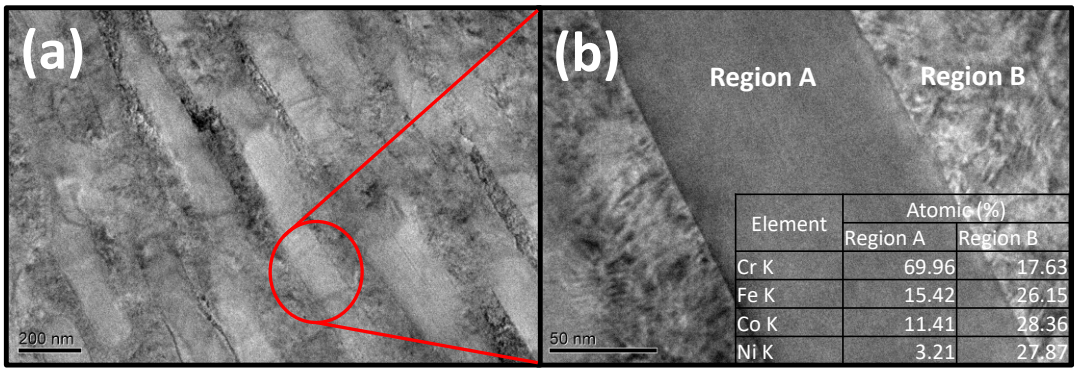

Figure 4. 13 TEM images of impure FeCoCrNi HEA a) Overall image, b) Image of focused on a specific region and EDS analysis

The proof of the formation of Cr_7C_3 can also be explained using the Ellingham diagram that shows the stability of the oxide or carbide as a function of temperature according to the position of the line for a given reaction. [76]. Figure 4.14 indicates the Ellingham diagram for the first transition series carbides. In the upper region of this diagram, carbides of the elements are unstable and easily reduced. The tendency of the elements to form carbides with C increases considerably as it goes to the bottom of the graph. According to the graph, Cr forms more stable carbide than the other elements in the alloy.

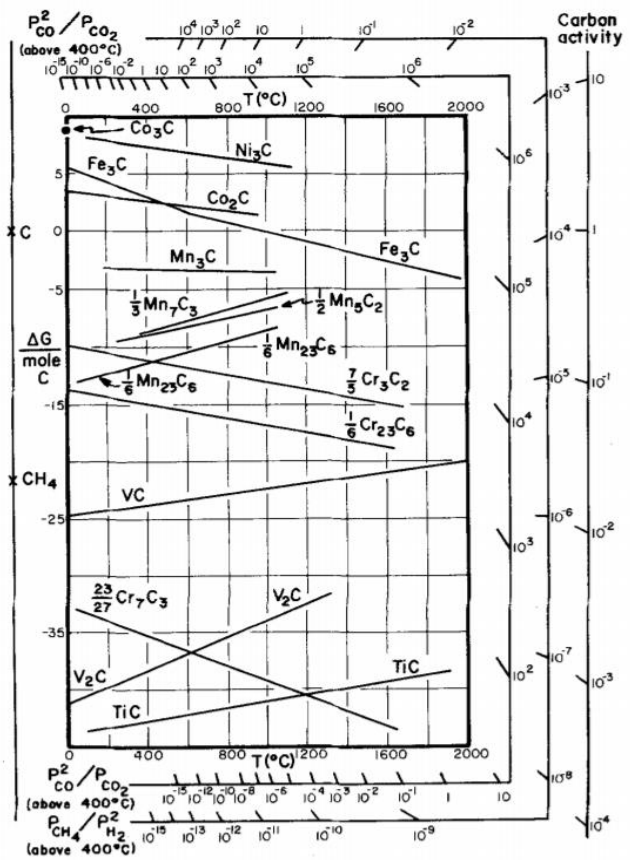

Figure 4. 14 Ellingham diagram for the first transition series carbides. The formation of the lowest compound is indicated by M_xC. Adopted from [76]

4.6 Heat Treatment Results for Impure FeCoCrNi HEA

It is not possible to prevent the formation of the Cr_7C_3 with slow cooling process temperatures as previously discussed in high temperature XRD results of section 4.3. However, in order to determine whether this phase was formed by rapid cooling process, the impure FeCoCrNi alloy was heated at 1373 K and kept for 24 hours. Then, the alloy was taken from the furnace and quenched rapidly. The XRD result and microstructure of the alloy under SEM and EDS analysis of selected region is given in Figure 4.15. As seen from XRD result, the phases formed in the quenched alloy are the same as the phases in the as-cast alloy. This means that high cooling

rate did not suppress the formation Cr_7C_3 phase. It can be concluded that this phase is very stable at room and high temperatures. According to the SEM image of the quenched alloy, the size of the dendrite zones is considerably shorter than those of the as-cast alloy. This is due to the fact that the high cooling rate does not allow sufficient diffusion of atoms. EDS results shown in Figure 4.15 (c) and (d) indicates that dendritic arms are rich in Cr and deprived in Ni as in the case of as-cast alloy.

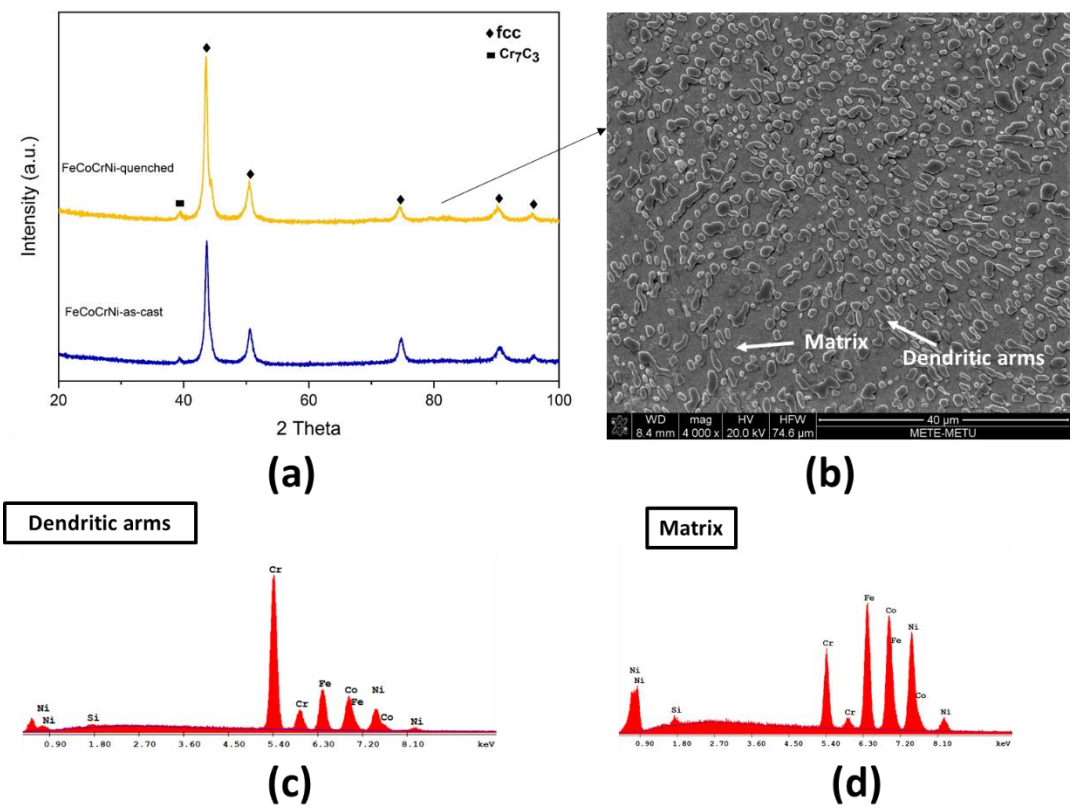

Figure 4. 15 (a) XRD graph of quenched and as-cast impure specimens, (b) SEM image of quenched specimen**,** EDS analysis (at. %) of (c) dendritic arms and (d) matrix

4.7 Mechanical Test Results

4.7.1 Tension Test Results of Impure FeCoCrNi HEA at 298 K and 773 K

The cylindrical rods shown in Figure 4.16 (a) and (b) obtained by induction melting were homogenized at 1373 K for 24 hours in order to eliminate segregation introduced by the casting operation. The dendrite structure of the impure alloy was broken down and became a non-equiaxed grain structure shown in Figure 4.16 (c). After homogenization of the pure alloy, columnar grain structure shown in Figure 4.16 (d) did not change.

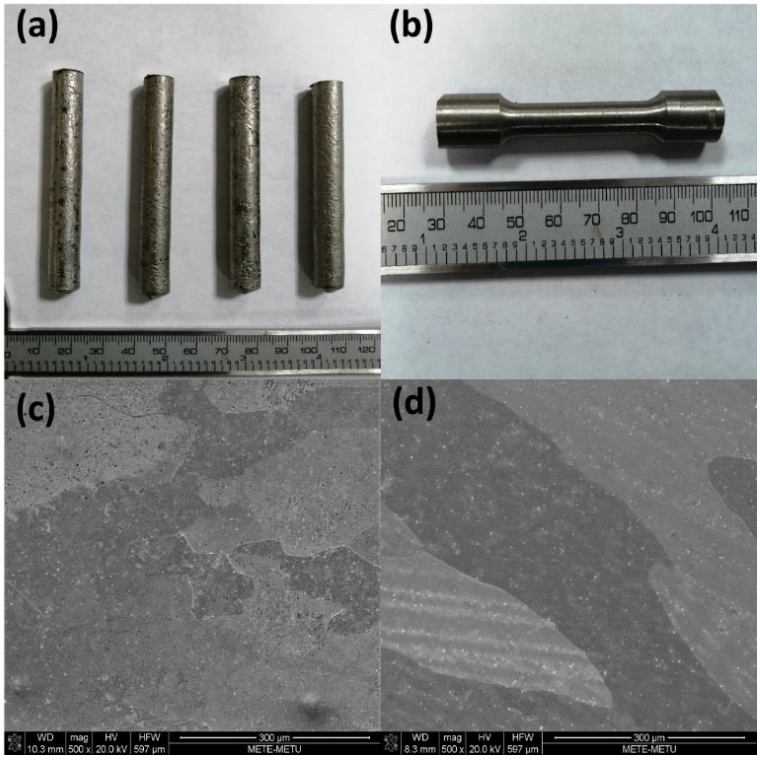

Figure 4. 16 (a) Pure and impure as-cast specimens, (b) tensile test specimen processed according to ASTM standard, (c) SEM images of homogenized impure specimen, (d) SEM images of homogenized pure specimen

Figure 4.17 (a) shows the tension test result of the impure FeCoCrNi HEA. In order to compare the results of the tensile test result at 298 K, tensile test specimens were also produced for pure FeCoCrNi HEA. The tension test results of both alloys are also shown in Figure 4.17 (b). Yield strength, $\sigma_{y,}$ and ultimate tensile strength, σ_{UTS}, of the pure FeCoCrNi HEA are approximately 245 MPa and 515 MPa respectively. Total elongation of high purity FeCoCrNi HEA is 57 %. On the other hand, since the elongation of the impure alloy is almost negligible, only the tensile strength of the alloy which is approximately 750 MPa could be measured. When Elastic modulus (E) of pure and impure alloys was calculated, the impure alloy which is approximately 162 GPa is considerably higher than the pure one which is approximately 104 GPa. When the fracture surface of pure alloy shown in Figure 4.18 (a) and (b) is examined, ductile type fracture is observed. That is, atomic bonds are broken across slip plane. This type of fracture is also called dimpled rupture. On the other hand, brittle fracture is observed in low purity FeCoCrNi HEA as shown in the Figure 4.18 (c) and (d). As the reason for this case is that in order to occur plastic deformation in the alloy, dislocation motion must take place. However, Cr_7C_3 is ceramic-based material and due to its lack of accessible slip system, dislocation movements are strictly restricted. Therefore, Cr_7C_3 significantly decreases the ductility of the alloy.

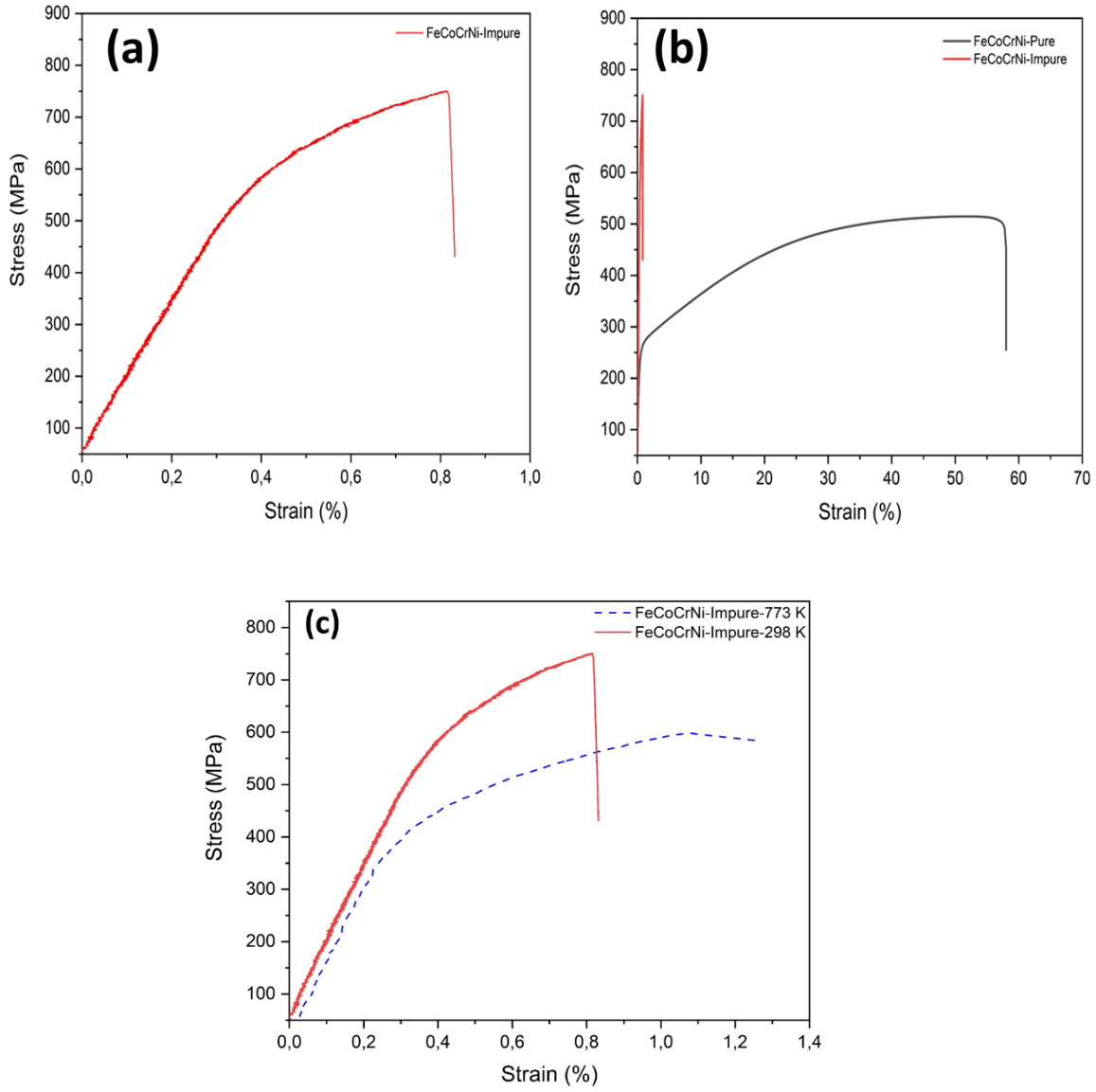

Figure 4. 17 Uniaxial tension test of (a) impure FeCoCrNi HEA, (b) comparison of pure and impure FeCoCrNi HEA tension test and (c) tension test of impure FeCoCrNi at 298 K and 773 K

Figure 4.17 (c) shows the tensile test results of the impure FeCoCrNi alloy at room temperature (298 K) and 773 K. The high temperature did not cause a significant increase in elongation while the tensile strength of the alloy, that is approximately 600 MPa, is decreased. As shown in Figure 4.18 (e) and (f), the specimen shows the

characteristic properties of brittle fracture which are flat facets, angular faceted steps, and river-patterns.

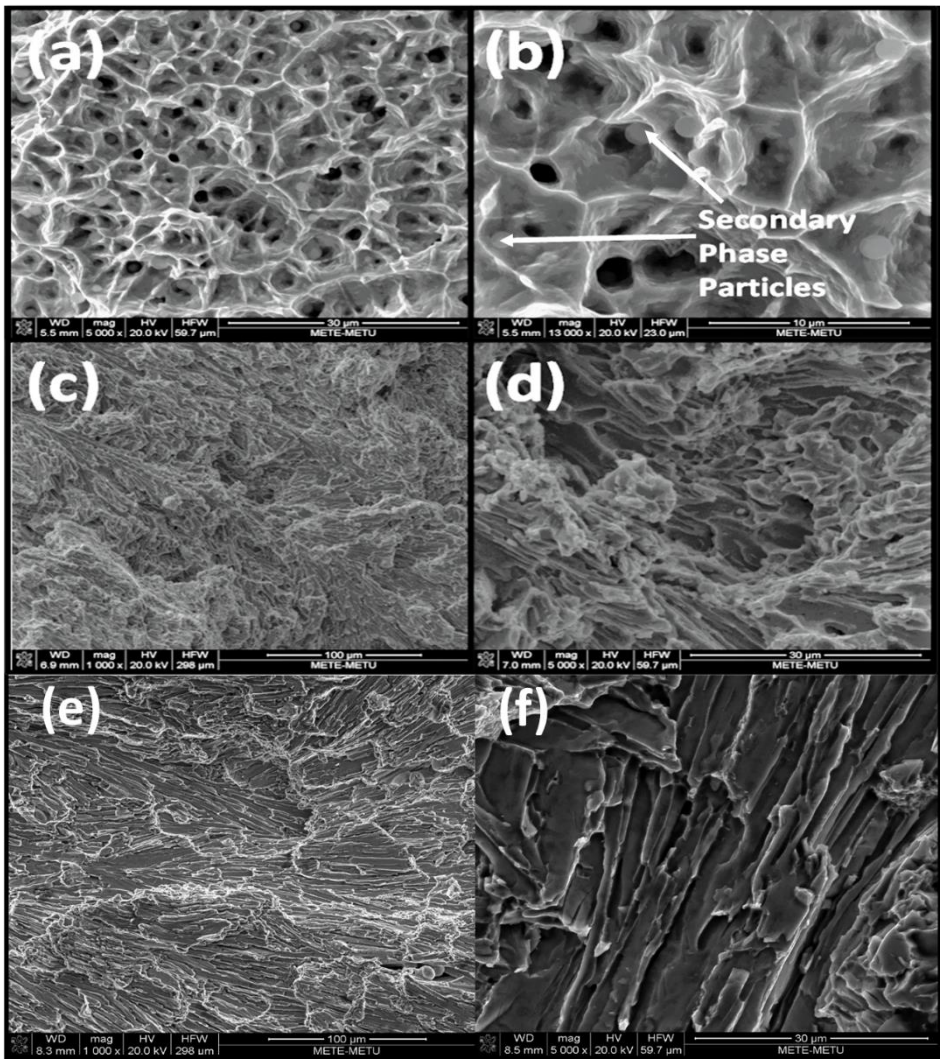

Figure 4. 18 SEM fracture surface analyses of a) the pure FeCoCrNi (5000x), b) the pure FeCoCrNi (13000x), c) the impure FeCoCrNi (1000x) at 298 K, d) the impure FeCoCrNi (5000x) at 298 K, e) the impure FeCoCrNi (1000x) at 773 K, f) the impure FeCoCrNi (5000x) at 773 K

4.7.2 Hardness Test Results of Pure and Impure $FeCoCrNiCu_x$, $FeCoCrNiAl_x$ (x: 0, 0.3, 0.6 and 1) alloys HEAs

Figure 4.19 shows the change in Vickers hardness value of pure and impure alloys as a function of Al and Cu content. The hardness of the pure FeCoCrNi alloy is 166 (±7) HV. However, the hardness value of the impure alloy is increased to 379 (±6) HV due to the reinforcement effect of Cr_7C_3 secondary phase. The addition of Cu into the main alloy did not cause a significant change in the hardness of the alloys as it did not affect the crystal structure. The hardness values of the pure $Cu_{0.3}$, $Cu_{0.6}$, and $Cu_{1.0}$ alloys are 160 (±3), 158 (±4) and 164 (±2) HV, respectively. The hardness values of the impure alloys are 376 (±8), 377.(±6) and 382 (± 6) HV, respectively.

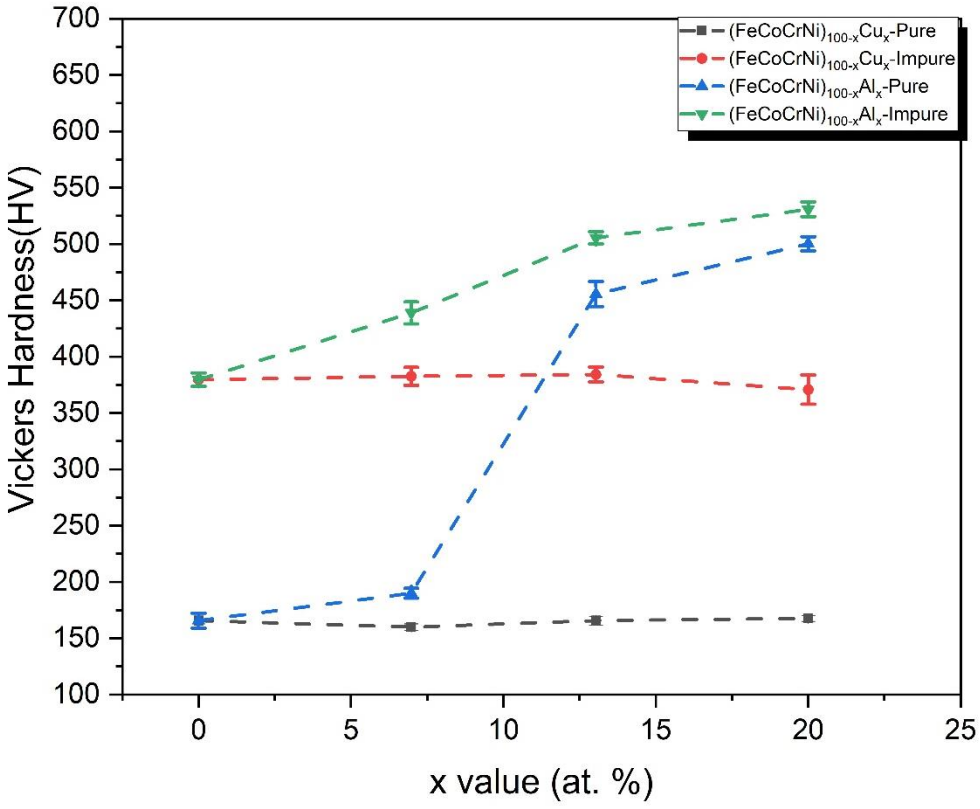

Figure 4. 19 Vickers hardness results of pure and impure $FeCoCrNiCu_x$, $FeCoCrNiAl_x$ (x: 0, 0.3, 0.6 and 1) alloys as a function of Al and Cu content (Dashed lines are drawn for eye tracking)

The addition of Al into the impure alloy induce a certain increase in the hardness value. The hardness values of the impure $Al_{0.3}$, $Al_{0.6}$ and $Al_{1.0}$ alloys are 439 (±10), 506 (±3) and 531 (±6) HV, respectively. The transformation of the crystal structure from FCC main phase to BCC main phase with minor secondary phase, Cr_7C_3, can be stated as the main evidence for increasing the hardness value. The reason of this phenomenon can be explained as it is much easier to move atoms along the slip planes in the closely packaged FCC structure compared to BCC which is slightly less closely packaged structure. The increment of Al in the pure main alloy caused significant changes in the hardness values. The hardness values of the pure $Al_{0.3}$, $Al_{0.6}$ and $Al_{1.0}$ alloys are 190 (±4) ,446 (±11), 500 (±6) HV, respectively. One of the most important reasons for substantial hardness difference between pure $Al_{0.3}$ and $Al_{0.6}$ alloys is that the higher Al ratio in the alloy enables stronger covalent bonds with other constituent elements. Phase transformation and microstructure differences are other important factors. In other words, the pure $Al_{0.3}$ alloy has FCC solid solution, while the pure $Al_{0.6}$ alloy has FCC+BCC phases with a small proportion of ordered BCC structure. In addition to the effect of BCC structure on the hardness, existence of ordered BCC structure, in which the diffusion of the atoms is much more difficult, is also effective in increasing the hardness value.

4.7.3 Compression Test Results of Pure and Impure $FeCoCrNiCu_x$, $FeCoCrNiAl_x$ (x: 0, 0.3, 0.6 and 1) alloys HEAs

The 4 mm diameter for as-cast pure alloys and 5mm diameter for impure as-cast alloys specimens shown in Figure 4.20 (a) and (b) were cut to the aspect ratio and grinded to obtain parallel surfaces.

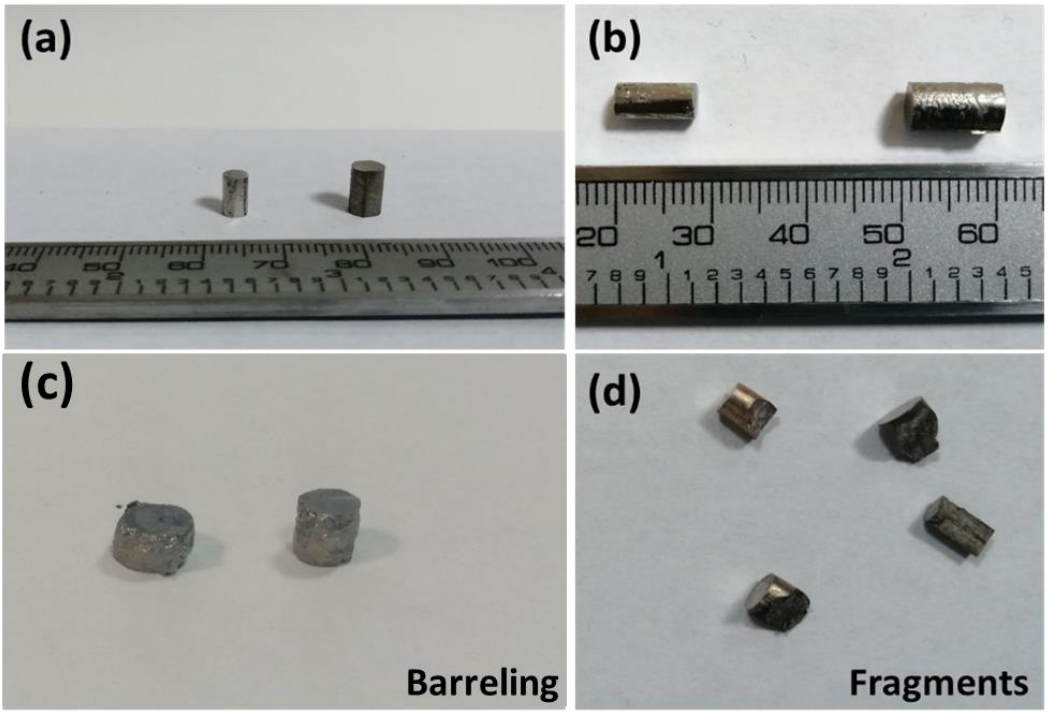

Figure 4. 20 The 4 mm and 5 mm compression test specimens of pure and impure cylindrical as-cast alloys with an aspect ratio of 2 a) vertical view, b) horizontal view, c) barreling of specimens and d) small fragments after the compression test

The pure main alloy, $Cu_{0.3}$, $Cu_{0.6}$, $Cu_{1.0}$ and $Al_{0.3}$ alloys are started to undergo strain hardening, which is defined as the increment of stress level to produce additional plastic deformation after a certain stress level since they are quite ductile materials. The specimens of these alloys did not fracture after the test. Barreling that is the formation of a convex surface on the outside of the specimen occurs as seen in Figure 4.20 (c). The reason of the barreling is due to the friction between the contact surfaces of the compression sample and the anvils. This deformation behavior shows that the applied stress is not uniaxial compression. Therefore, the results which are not realistic the results are not introduced in this study. However, it can be interpreted that the barreled alloys shows similar mechanical properties

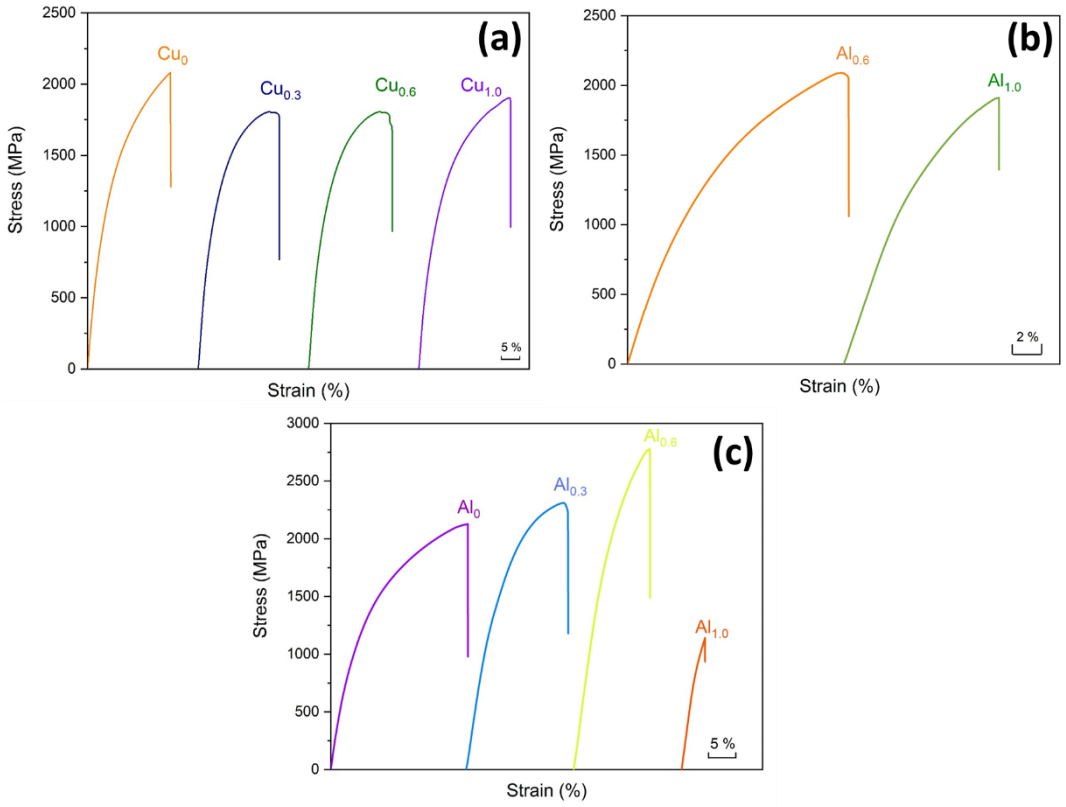

Figure 4. 21 Compressive stress-strain curves of (a) impure $FeCoCrNiCu_x$, (b) pure $FeCoCrNiAl_x$ and (c) impure $FeCoCrNiAl_x$

The results obtained from the compression test graph of the impure main alloy, $Cu_{0.3}$, $Cu_{0.6}$ and $Cu_{1.0}$ alloys are shown in Figure 4.21 (a). It is indicated that the effect of Cr_7C_3 secondary phase which is the reinforcement phase in the alloys caused significant increase in compression test results as well as hardness results. As shown in Figure 4.21 (a), all specimens fractured after a certain ductility and strength values. According to Table 4.7 which shows the approximate yield strength (σ_y), maximum compressive strength (σ_{max}) and compressive strain at fracture (ε_{comp}) values of the pure $FeCoCrNiAl_x$ and the impure $FeCoCrNiCu_x$ $FeCoCrNiAl_x$ alloys, yield strength values of the impure main alloy, $Cu_{0.3}$, $Cu_{0.6}$ and $Cu_{1.0}$ alloys are 1020, 930,925, and 945 MPa, maximum compressive strength values of them are 2125, 1805, 1806 and 1973 MPa respectively. The obtained strength values of the alloys are very close to each other due to the similarity of crystal structures and microstructures. Besides

these strength values, all alloys exhibit significant amount of ductility. The percent compressive strain at fracture for the main alloy, $Cu_{0.3}$, $Cu_{0.6}$ and $Cu_{1.0}$ are calculated as 25%, 22.1 %, 22.8 % and 25.9 %, respectively.

Table 4. 7 Yield strength (σ_y), maximum compressive strength (σ_{max}), compressive strain at fracture (ε_{comp}) values of the pure $FeCoCrNiAl_x$ and the impure $FeCoCrNiCu_x$ $FeCoCrNiAl_x$ alloys

	Alloy	**σ_y (MPa)**	**σ_{max} (MPa)**	**ε_{comp} (%)**
Pure	**$FeCoCrNiAl_{0.6}$**	1270	2090	15.4
	FeCoCrNiAl	1255	1934	10.7
Impure	**FeCoCrNi**	1020	2125	25.0
	$FeCoCrNiCu_{0.3}$	930	1805	22.1
	$FeCoCrNiCu_{0.6}$	925	1806	22.8
	FeCoCrNiCu	945	1973	25.9
	$FeCoCrNiAl_{0.3}$	1170	2310	19.0
	$FeCoCrNiAl_{0.6}$	1485	2770	14.0
	FeCoCrNiAl	-	1140	4.3

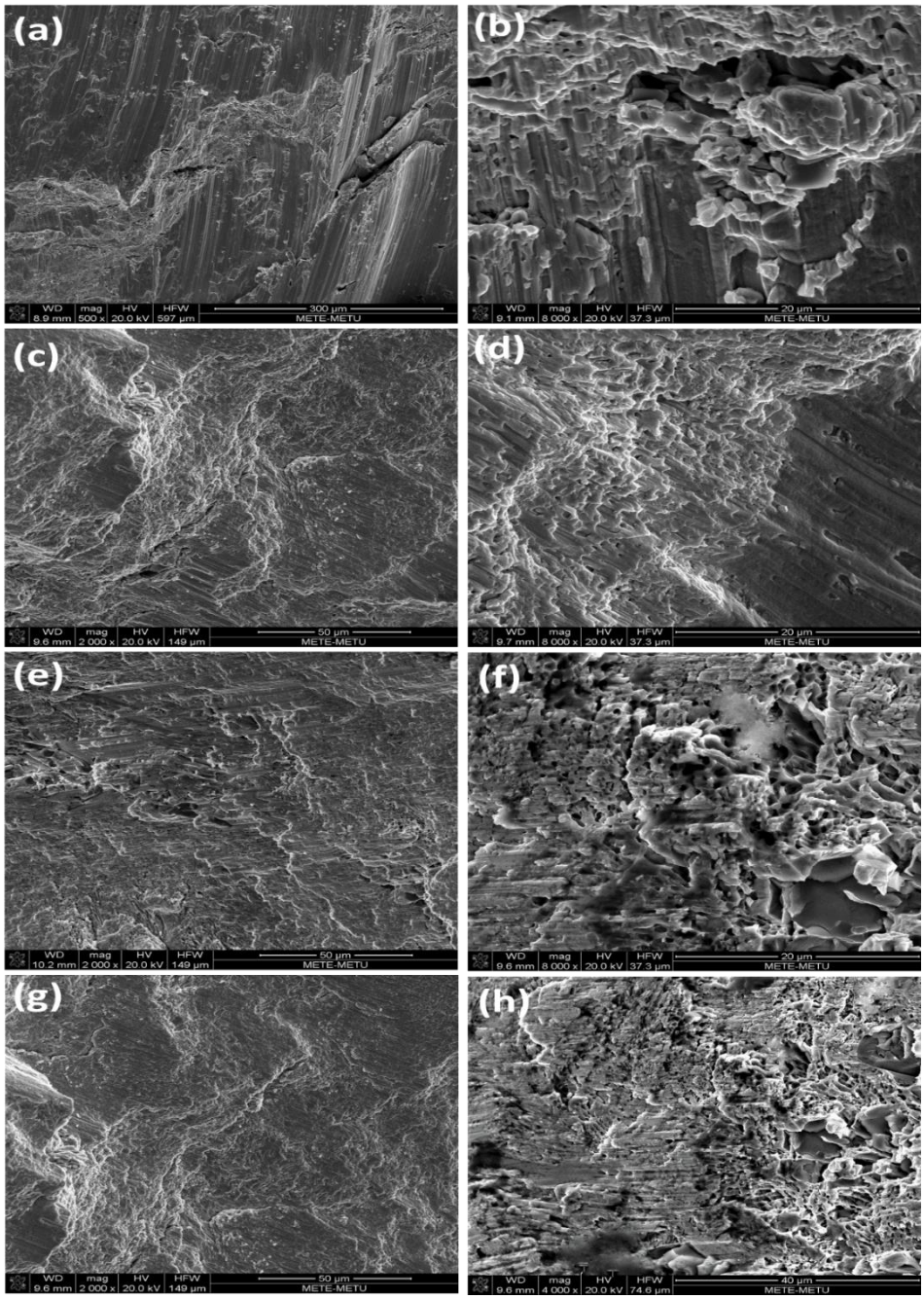

Figure 4. 22 SEM fracture analysis of a) the impure FeCoCrNi (500x), b) the impure FeCoCrNi (8000x) c) the impure $FeCoCrNiCu_{0.3}$ (2000x), d) the impure $FeCoCrNiCu_{0.3}$ (8000x), e) the impure $FeCoCrNiCu_{0.6}$ (2000x), f) the impure $FeCoCrNiCu_{0.6}$ (8000x), g) the impure $FeCoCrNiCu_{1.0}$ (2000x), h) the impure $FeCoCrNiCu_{1.0}$ (8000x) after the compression test

Fig. 4.22 shows the SEM images of the fracture surface of the impure main alloy, $Cu_{0.3}$, $Cu_{0.6}$ and $Cu_{1.0}$ specimens after compression deformation. All alloys show mixed type fracture which includes ductile and brittle behaviour. The teared dimples are evidence of plastic deformation. Cleavage facets clearly show brittle type fracture. The fracture surface formed by cleavage facets and teared dimples is called quasi-cleavage fracture.

The compression test results of the pure $Al_{0.6}$ and $Al_{1.0}$ alloys are shown in Figure 4.21 (b). Yield strength, maximum compressive strength, compressive strain at fracture values of these alloys are given in Table 4.7. According to the results, the addition of Al has a significant effect on the compression test results as well as the hardness. The mechanical properties of the pure $Al_{0.6}$ and $Al_{1.0}$ alloys have significantly improved with the emergence of the BCC phase with minor ordered BCC in their crystal structure. More specifically, the yield strengths of $Al_{0.6}$ and $Al_{1.0}$ alloys are 1270 MPa and 1255 MPa, respectively. Their maximum strengths are 2090 and 1934 MPa, respectively. It is a known fact that this amount of increase in strength has a certain negative effect on the compressive strain of the alloys. However, these values of alloys which are 15.4% for $Al_{0.6}$ alloy and 9.2% for the $Al_{1.0}$ are still remarkably high. The reasons for the better mechanical properties of the $Al_{0.6}$ alloy compared to $Al_{1.0}$ alloy can be explained as the transformation of FCC phase completely in the $Al_{0.6}$ alloy to the BCC phase in the $Al_{1.0}$ alloy, and the increase of the proportion of ordered BCC phase in the $Al_{1.0}$ alloy. As mentioned in section 4.7.2 hardness test results, since the FCC is a close packed structure, it is much easier to slide the atomic planes over each other during deformation. In addition, since the diffusion of atoms is also very limited in the ordered BCC structure, the $Al_{1.0}$ alloy becomes more resistant to plastic deformation. As seen from the compression stress-strain graph, it can be interpreted that the slope of the $Al_{1.0}$ line higher than the slope of $Al_{0.6}$ line. Besides, the $Al_{1.0}$ alloy is expected to be more resistant to elastic deformation due to the existence of hard phases.

Fig. 4.23 shows the SEM images of the fracture surface of the pure $Al_{0.6}$ and $Al_{1.0}$ after compression deformation. At low magnifications, the fracture surface of the

$Al_{0.6}$ alloy is fine granular appearance (Fig. 4.23 (a)), on the other hand the $Al_{1.0}$ surface has coarser facets appearance (Fig. 4.23 (c)). At high magnifications, $Al_{0.6}$ alloy has both brittle and ductile fracture surface (Fig. 4.23 (b)). Flat facets are evidence of brittle type fracture. Dimples of different diameters surrounding these flat facets are indicator of ductile type fracture. The formation of these fracture surfaces can be explained as follow: cracks at the interfaces of BCC and FCC phases occur as brittle type, then these cracks open and take the form of dimples by plastic deformation. $Al_{1.0}$ alloy clearly shows the characteristic properties of brittle fracture which are flat facets, angular faceted steps, river-patterns.

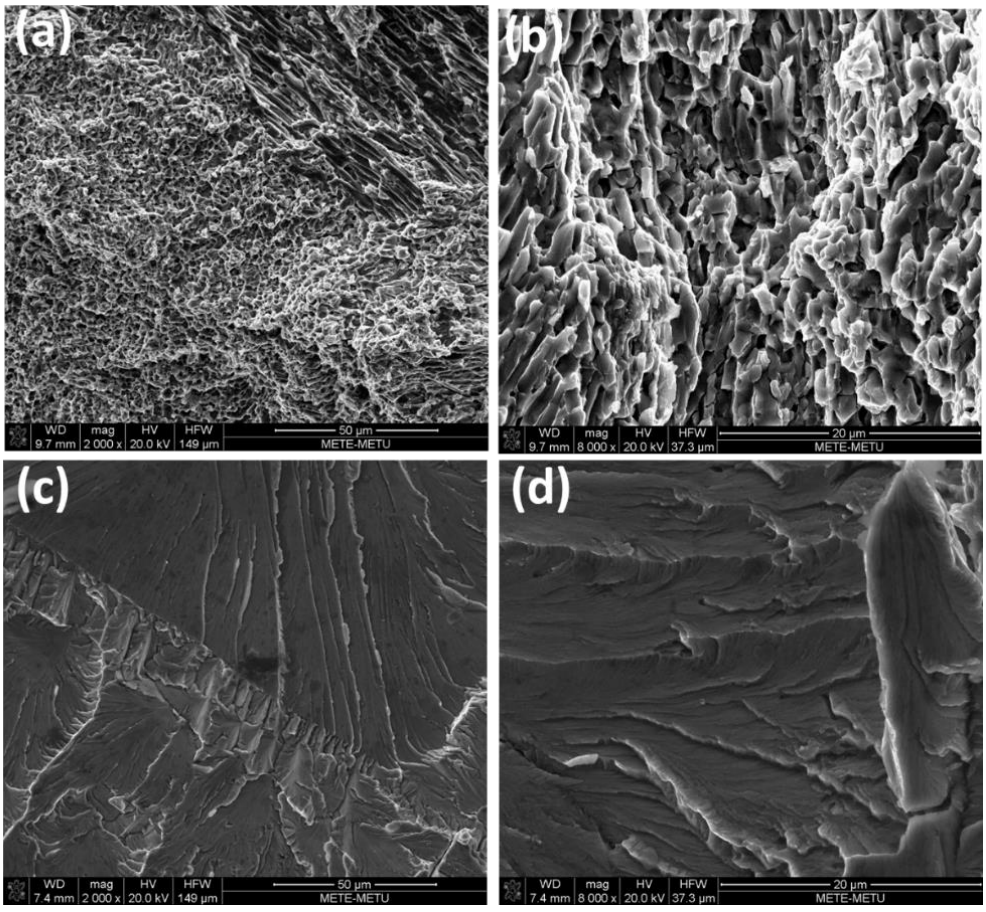

Figure 4. 23 SEM fracture analysis of a) the pure $FeCoCrNiAl_{0.6}$ (2000x), b) the pure $FeCoCrNiAl_{0.6}$ (8000x), c) the pure $FeCoCrNiAl_{1.0}$ (2000x), d) the pure $FeCoCrNiAl_{1.0}$ (8000x) after the compression test

According to the compression stress strain graph of the impure alloys containing Al shown in Figure 4.21 (c), there are several differences in mechanical properties compared to the pure alloys. It is more clearly that the yield and maximum strength of the impure $Al_{0.3}$ alloy increased considerably with the effect of Cr_7C_3 phase compared to pure one. This alloy has also remarkable ductility value calculated as 19%. When the pure and impure $Al_{0.6}$ alloys are compared, the yield and maximum strength of the impure $Al_{0.6}$ alloy, which are 1485 MPa and 2770 MPa, respectively, is further improved than the pure one. Although the compressive strain value of the impure $Al_{0.6}$ found as 14% is lost to a certain extent, it is still significant for engineering applications. Based on these results, it is assumed that the amount of FCC and BCC phases in the pure and impure alloys are the same, the Cr_7C_3 phase contributes more to the improvement of mechanical properties than ordered BCC structure. At the same time, the hardness test proves these results. When the pure and impure $Al_{1.0}$ alloys are compared, the mechanical properties of the impure $Al_{1.0}$ alloy became worse compared to the pure alloy. The compressive strain of the impure $Al_{1.0}$ alloy was found as approximately 4.3%. It can be more realistic to mention maximum compressive strength rather than yield strength because of the very low ductility value for this alloy. The maximum strength of this alloy is 1140 MPa that is very close to the yield strength of the pure $Al_{1.0}$ alloy. The reason is the crystal structure of the impure $Al_{1.0}$ crystal structure which consists of Cr_7C_3 and BCC phases. The pure alloy is composed of BCC phase with small proportion of ordered BCC. It is known that BCC phase is harder than the FCC phase, and it is also estimated that Cr_7C_3 phase is a harder than ordered BCC as mentioned above. Therefore, dislocation movement in the impure $Al_{1.0}$ alloy is severely restricted due to the combination of two hard phases. In other words, excessive hardening of the structure causes the alloy to become very brittle.

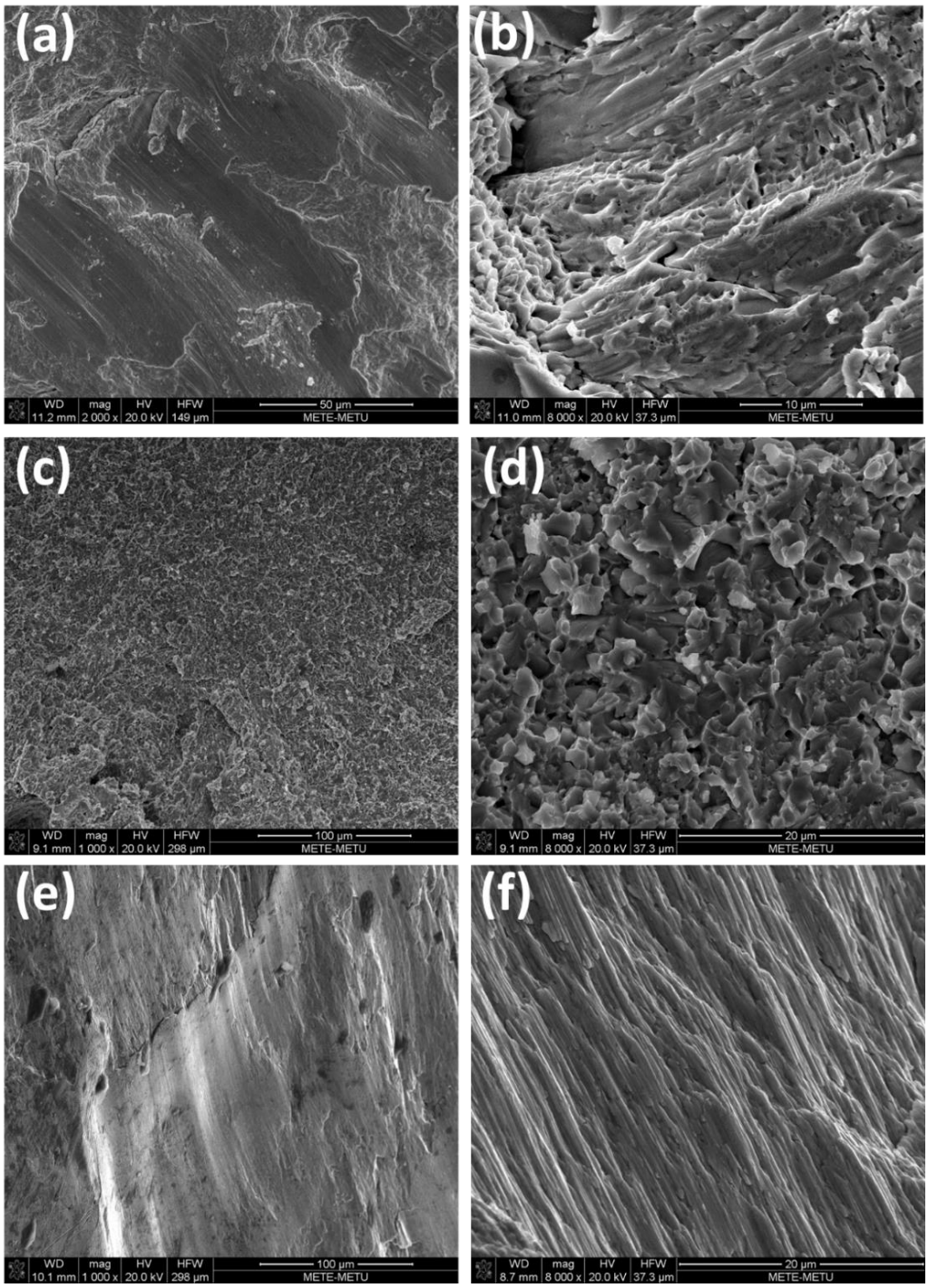

Figure 4. 24 SEM fracture analysis of a) the impure $FeCoCrNiAl_{0.3}$ (2000x), b) the impure $FeCoCrNiAl_{0.3}$ (8000x), c) the impure $FeCoCrNiAl_{0.6}$ (1000x), d) the impure $FeCoCrNiAl_{0.6}$ (8000x), e) the impure $FeCoCrNiAl_{1.0}$ (1000x), f) the impure $FeCoCrNiAl_{1.0}$ (8000x) after the compression test

Fig. 4.24 represents the SEM images of the fracture surface of the impure $Al_{0.3}$, $Al_{0.6}$ and $Al_{1.0}$ after compression deformation. $Al_{0.3}$ and $Al_{0.6}$ alloys have both brittle and ductile fracture. The dimples in $Al_{0.3}$ alloy are proof of plastic deformation. They became teared in the impure main alloy and Cu containing alloys. Cleavage surfaces are also the indication of brittle type fracture. The fracture surface of the impure $Al_{0.6}$ alloy appearance (Fig. 4.24 (c)), has a fine granular appearance as in the pure $Al_{0.6}$ alloy at low magnification. Dimples of different diameters indicate ductile type fracture, while the flat surfaces at the interfaces of these dimples indicate brittle type fracture. When the impure $Al_{1.0}$ alloy is examined, it can be stated that it undergoes plastic deformation in a relatively small proportion according to the compression stress- strain graph. However, the fracture surface of the alloy is very smooth facets and angular faceted steps that are the characteristic features of brittle type fracture.

4.8 Comparison of the impure $FeCoCrNiAl_{0.6}$ HEA and Conventional Metal Alloys

Figure 4.25 shows the comparison of room temperature yield strength vs density modulus for conventional metal alloys and CCAs. The dashed lines demonstrate the performance index for different loading conditions: uniaxial loading (slope, s = 1), beam bending, (s = 3/2), panel bending (s = 2). Materials that are above these lines can be defined as ultra-high strength alloys. In fact, all the data are below these lines due to differences in loading conditions.

In this thesis, the most promising alloy in terms of mechanical properties is the impure $FeCoCrNiAl_{0.6}$ alloy produced by the induction melting method. The structure of the impure $FeCoCrNiAl_{0.6}$ alloy consist of BCC and FCC main phases with minor Cr_7C_3 phase. The yield and maximum strength of the alloy are 1485 MPa and 2770 MPa respectively. As seen from the Figure 4.26, this alloy is located above s=1 line. It can be concluded that this alloy shows better mechanical properties as compared to Mg, Al, Ti and most of the Fe, Ni alloys and CCAs as indicated in Figure 4.25.

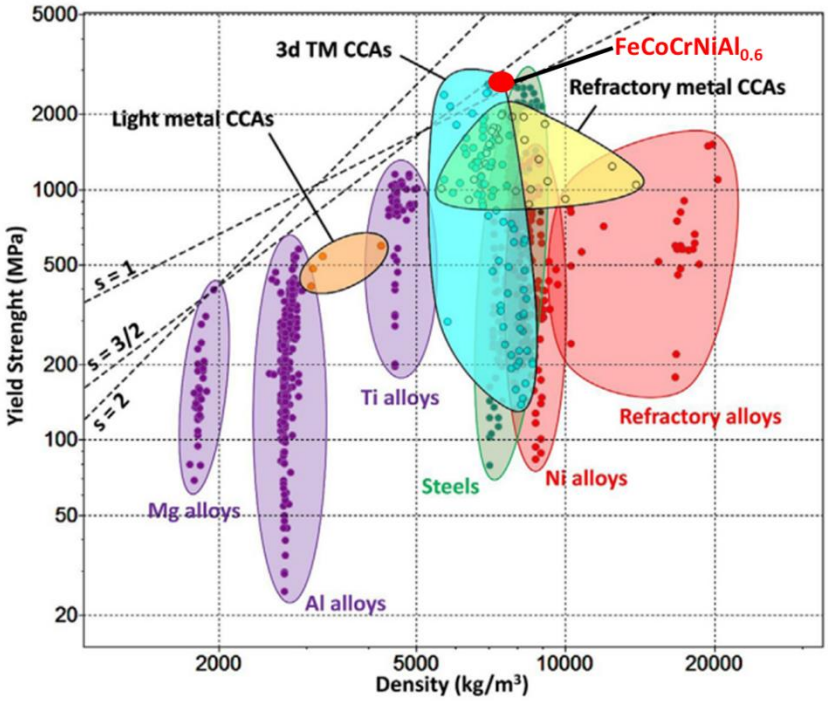

Figure 4. 25 Comparison of room temperature yield strength vs density for conventional metal alloys and CCAs. Adopted from [77]

4.9 Cost Analysis

Material cost is important as well as the structural and mechanical properties of the engineering materials. Nevertheless, material and production costs are not taken into consideration since laboratory scale production is carried out in material research studies. In this study, it is aimed that the produced impure alloys have advantages in terms of material cost in addition to having similar or better structural and mechanical properties compared to pure alloys. Table 4.8 shows the cost of 1 kilogram of each alloying element and total material cost of the pure FeCoCrNi, FeCoCrNiCu and FeCoCrNiAl for 1 kg. The prices of pure elements are taken from Alfa Aesar Chemicals [78]. Table 4.9 demonstrates the cost of 1 kilogram of each element and total material cost of the impure FeCoCrNi, FeCoCrNiCu and FeCoCrNiAl for 1 kg. The prices of impure elements were taken from different

suppliers in Turkey. As it can be seen from the tables, production of the alloys by using high purity elements brings with it a very high material cost. On the other hand, the use of impure elements reduces the cost of the alloys by more than 20 times per alloy.

Table 4. 8 Material cost of the pure FeCoCrNi, FeCoCrNiCu and FeCoCrNiAl alloys

Element (Pure)	**Cost/1 kg (€)**	**1 kg FeCoCrNi**	**1 kg FeCoCrNiCu**	**1 kg FeCoCrNiAl**
Fe (99.97%)	94.90	23.51	18.33	0.11
Co (99.9%)	522.00	136.45	106.43	10.27
Cr (99.2%)	586.00	135.13	105.42	0.31
Ni (99.95%)	253.00	65.86	51.38	2.66
Cu (99.9%)	246.00		54.09	
Al(99.99 %)	654.00			0.15
Total Cost (€)	**360.95**	**335.65**	**392.27**	

Table 4. 9 Material cost of the impure FeCoCrNi, FeCoCrNiCu and FeCoCrNiAl alloys

Element (Impure)	**Cost/1 kg (€)**	**1 kg FeCoCrNi**	**1 kg FeCoCrNiCu**	**1 kg FeCoCrNiAl**
Fe (AISI 1020)	0.49	0.08	0.09	0.11
Co (98.7%)	44.00	11.65	8.97	10.27
Cr (FeCr 71.84%Cr)	1.10	0.35	0.27	0.31
Ni (98.7%)	11.44	3.02	2.32	2.66
Cu (99.1%)	5.20		0.31	
Al(1050)	1.43			0.15
Total Cost (€)		**15.10**	**11.96**	**13.5**

CHAPTER 5

CONCLUSION & FUTURE RECOMMENDATIONS

In this study, the structural and mechanical properties of impure and pure FeCoCrNi, $FeCoCrNiCu_x$, and $FeCoCrNiAl_x$ (x: 0.3, 0.6, 1) alloys were investigated. The properties of pure and impure alloys were also compared in accordance with the amount of Al and Cu. The impure alloys were produced by induction melting method, while the pure alloys were produced by arc-melting method. The thermodynamic calculations and assumption of crystal structures of the alloys were studied by using the HEA calculator and VASP simulation program before the examination of the produced alloys. X-ray diffraction (XRD) for determining the crystal structure, transmission and scanning electron microscopy (SEM and TEM) for observing the resulting microstructures (TEM) were used. Hardness, tension and compression tests were applied for mechanical characterization of the alloys. The main points of the results can be concluded as follows:

(i) The calculated thermodynamic results indicate that the addition of Cu into FeCoCrNi main alloy decreases atomic size difference (δ) and increases ΔHmix value of the alloy. In addition, Cu increases VEC which promotes stable FCC structure. On the other hand, Al increases δ value and decreases the ΔHmix values. This element also reduces proportionately ΔSmix and VEC value of the alloy.

(ii) XRD results show that Cr_7C_3 phase is present with the main phases due to C impurities in the raw materials. The formation of Cr_7C_3 phase is proved by TEM, as well. This phase was not suppressed when the alloy was produced at a higher solidification rate.

(iii) The addition of Cu in different proportions to the main alloy had no effect on the change of crystal structure for both pure and impure alloys. On the

other hand, the addition of Al makes possible the transformation from FCC to BCC phase.

(iv) The microstructure of the impure FeCoCrNi alloy shows columnar dendrite structure which consists of dendritic and interdendritic regions. According to EDS results, the interdendritic regions are rich in Cr which means that Cr_7C_3 phase forms in that region. Otherwise, the microstructure of pure FeCoCrNi alloy is composed of columnar grains with homogeneously distributed elements.

(v) There was no significant change in the microstructure of Cu containing alloys as in the XRD results. Microstructures of pure and impure $Cu_{0.3}$, $Cu_{0.6}$ and $Cu_{1.0}$ alloys consist of dendritic structure. The addition of Al into FeCoCrNi alloy shows the evolution of the microstructures of both impure and pure alloys. The impure $Al_{0.3}$ alloy has dendritic structure. The pure $Al_{0.3}$ alloy is composed of columnar grains as in the pure FeCoCrNi alloy. The microstructure of the impure $Al_{0.6}$ alloys comprises of both dendrites, interdendrites and plate like structures. The pure $Al_{0.6}$ alloy consists of long Widmanstatten side plates formed along grain boundary regions. This is arisen from quite narrow solidification temperature range.

(vi) Tension test results at ambient and high temperature point out that the pure FeCoCrNi HEA has low yield and tension strength with very high ductility. However, there is no elongation for the impure alloy so only the tensile strength is obtained. High temperature tension test does not improve the ductility of the alloy significantly.

(vii) The addition of Cu does not have remarkable effect on the compression test results of the impure alloys. However, the addition of Al has a significant effect on the compression test results. The mechanical properties of the pure $Al_{0.6}$ and $Al_{1.0}$ alloys have been significantly improved with the emergence of the BCC phase with minor ordered BCC in their crystal structure. The highest yield and tension strength values with good ductility are obtained in the

impure $Al_{0.6}$ which shows better mechanical properties compared to Mg, Al, Ti and most of the Fe, Ni alloys. It can be concluded Cr_7C_3 phase further improves the mechanical properties of the alloys relative to the ordered BCC.

As a future study, I would recommend to implement high entropy alloys to additive manufacturing. Additive manufacturing method (AM) has recently attracted much attention due to its high production efficiency, low production cost and production of complex parts with net-shape. AM processes is an advanced manufacturing technique which uses a 3D CAD file and slides into different thicknesses [79]. AM method is completely different from conventional production methods such as arc melting and induction casting. Therefore, the effect of this production method on the mechanical, structural and chemical properties of the materials needs to be examined in detail. AM method has many different way of processing. The most popular and widespread of these is the selective laser melting (SLM) due to the fact that it is the fastest production process and many parts can be produced in one round [80]. HEAs are very suitable materials for additive manufacturing due to their composite like structure. The number of studies in which such alloys are produced and examined by additive manufacturing method have been increasing. One of the study carried out by Brif et al. [81] is that the well-known FeCoCrNi alloy was produced by SLM. Gas-atomized powders were used for production. The same alloy was produced by arc melting to compare the properties of the alloys. The obtained results indicate that has been observed that the mechanical properties of AM samples improved considerably compared to as-cast samples due to the fine microstructure of AM sample. In conclusion, AM method is expected to be a popular production method in the future due to its remarkable advantages as mentioned above.

REFERENCES

[1] J. W. Yeh *et al.*, "Nanostructured high-entropy alloys with multiple principal elements: Novel alloy design concepts and outcomes," *Adv. Eng. Mater.*, vol. 6, no. 5, pp. 299-303 2004.

[2] J. Y. He *et al.*, "A precipitation-hardened high-entropy alloy with outstanding tensile properties," *Acta Mater.*, vol. 102, pp. 187–196, 2016.

[3] B. Liu *et al.*, "Microstructure and mechanical properties of equimolar FeCoCrNi high entropy alloy prepared via powder extrusion," *Intermetallics*, vol. 75, pp. 25–30, 2016.

[4] W. R. Wang, W. L. Wang, S. C. Wang, Y. C. Tsai, C. H. Lai, and J. W. Yeh, "Effects of Al addition on the microstructure and mechanical property of Al xCoCrFeNi high-entropy alloys," *Intermetallics*, vol. 26, pp. 44–51, 2012.

[5] Y. J. Zhou, Y. Zhang, Y. L. Wang, and G. L. Chen, "Solid solution alloys of $AlCoCrFeNiTi_x$ with excellent room-temperature mechanical properties," *Appl. Phys. Lett.*, vol. 90, no. 18, 2007.

[6] C. J. Tong *et al.*, "Mechanical performance of the AlxCoCrCuFeNi high-entropy alloy system with multiprincipal elements," *Metall. Mater. Trans. A Phys. Metall. Mater. Sci.*, vol. 36, no. 5, pp. 1263–1271, 2005.

[7] A. Takeuchi and A. Inoue, "Calculations of mixing enthalpy and mismatch entropy for ternary amorphous alloys," *Mater. Trans. JIM*, vol. 41, no. 11, pp. 1372–1378, 2000.

[8] A. Inoue, "Stabilization of metallic supercooled liquid and bulk amorphous alloys," *Acta Mater.*, 2000.

[9] A. Inoue, K. Ohtera, K. Kita, and T. Masumoto, "New Amorphous Mg-Ce-Ni

Alloys with High Strength and Good Ductility : Condensed Matter," *Jpn. J. Appl. Phys.*, vol. 27, no. 12, p. L2248, 1988.

[10] A. Inoue, N. Nishiyama, and T. Matsuda, "Preparation of bulk glassy $Pd_{40}Ni_{10}Cu_{30}P_{20}$ alloy of 40 mm in diameter by water quenching," *Materials Transactions, JIM*, vol. 37, no. 2. pp. 181–184, 1996.

[11] A. Inoue, T. Zhang, and T. Masumoto, "Zr-Al-Ni Amorphous Alloys with High Glass Transition Temperature and Significant Supercooled Liquid Region," *Materials Transactions, JIM*, vol. 31, no. 3. pp. 177–183, 1990.

[12] A. Peker and W. L. Johnson, "A highly processable metallic glass: $Zr_{41.2}Ti_{13.8}Cu_{12.5}Ni_{10.0}Be_{22.5}$," *Appl. Phys. Lett.*, vol. 63, no. 17, pp. 2342–2344, 1993.

[13] A. Inoue, A., Zhang, T., Itoi, T. and Takeuchi, "New Fe–Co–Ni–Zr–B amorphous alloys with wide supercooled liquid regions and good soft magnetic properties," *Mater. Trans. JIM*, vol. 38, no. 4, pp. 359–362, 1997.

[14] A. Inoue and J. S. Gook, "Fe-based ferromagnetic glassy alloys with wide supercooled liquid region," *Materials Transactions, JIM*, vol. 36, no. 9. pp. 1180–1183, 1995.

[15] D. B. Miracle and O. N. Senkov, "A critical review of high entropy alloys and related concepts," *Acta Mater.*, vol. 122, pp. 448–511, 2017.

[16] Y. Zhang *et al.*, "Microstructures and properties of high-entropy alloys," *Prog. Mater. Sci.*, vol. 61, no. September 2013, pp. 1–93, 2014.

[17] K.-H. Huang and J. W. Yeh, "A study on the multicomponent alloy systems containing equal-mole elements," National Tsing Hua University, 1996.

[18] M. H. Tsai and J. W. Yeh, "High-entropy alloys: A critical review," *Mater. Res. Lett.*, vol. 2, no. 3, pp. 107–123, 2014.

[19] B. Cantor, I. T. H. Chang, P. Knight, and A. J. B. Vincent, "Microstructural development in equiatomic multicomponent alloys," *Mater. Sci. Eng. A*, vol. 375–377, no. 1-2 SPEC. ISS., pp. 213–218, 2004.

[20] D.R. Gaskell, “Introduction to the Thermodynamics of Materials,” *London, UK.:T aylor and Francis*, 4th ed., pp. 89-92, 2003

[21] B. S. Murty, J. W. Yeh, S. Ranganathan, and P. P. Bhattacharjee, “High-entropy alloys: basic concepts,” *High-Entropy Alloys*, pp. 13–30, 2019.

[22] J. W. Yeh, “Alloy design strategies and future trends in high-entropy alloys,” *Jom*, vol. 65, no. 12, pp. 1759–1771, 2013.

[23] W. F. Smith, “*Structure and properties of engineering alloys,* ” *McGraw-Hill*, pp. 125-126, 1993.

[24] J.-W. Yeh, “Recent progress in high-entropy alloys,” *Ann. Chim. Sci. des Mater.*, vol. 31, no. 6, pp. 633–648, 2006.

[25] B.D. Cullity and S.R. Stock, “Elements of X-Ray Diffraction,” *Upper Saddle River: NJ: Prentice-Hall Inc.*, 3rd ed., pp. 57-63, 2001.

[26] R.E. Reed-Hill and R. Abbaschian, “Physical Metallurgy Principles, ” *Boston: MA: PWS Publishing Company,* 4th ed., pp. 261-267, 2008.

[27] M. F. Del Grosso, G. Bozzolo, and H. O. Mosca, “Determination of the transition to the high entropy regime for alloys of refractory elements,” *J. Alloys Compd.*, vol. 534, pp. 25–31, 2012.

[28] O. N. Senkov, G. B. Wilks, D. B. Miracle, C. P. Chuang, and P. K. Liaw, “Refractory high-entropy alloys,” *Intermetallics*, vol. 18, no. 9, pp. 1758–1765, 2010.

[29] C. Ng, S. Guo, J. Luan, S. Shi, and C. T. Liu, “Entropy-driven phase stability and slow diffusion kinetics in an $Al_{0.5}$CoCrCuFeNi high entropy alloy,” *Intermetallics*, vol. 31, pp. 165–172, 2012.

[30] C. J. Tong *et al.*, “Microstructure characterization of AlxCoCrCuFeNi high-entropy alloy system with multiprincipal elements,” *Metall. Mater. Trans. A Phys. Metall. Mater. Sci.*, vol. 36, no. 4, pp. 881–893, 2005.

[31] and X. Z. Anmin, L. I., "'Thermodynamic analysis of the simple microstructure of AlCrFeNiCu high-entropy alloy with multi-principal elements.,'" *Acta Metall. Sin. (English Lett.*, vol. 22, no. 3, pp. 219–224, 2009.

[32] K. Y. Tsai, M. H. Tsai, and J. W. Yeh, "Sluggish diffusion in Co-Cr-Fe-Mn-Ni high-entropy alloys," *Acta Mater.*, vol. 61, no. 13, pp. 4887–4897, 2013.

[33] J. W. Yeh, S. Y. Chang, Y. Der Hong, S. K. Chen, and S. J. Lin, "Anomalous decrease in X-ray diffraction intensities of Cu-Ni-Al-Co-Cr-Fe-Si alloy systems with multi-principal elements," *Mater. Chem. Phys.*, vol. 103, no. 1, pp. 41–46, 2007.

[34] W. H. Liu, Y. Wu, J. Y. He, T. G. Nieh, and Z. P. Lu, "Grain growth and the Hall-Petch relationship in a high-entropy FeCrNiCoMn alloy," *Scr. Mater.*, vol. 68, no. 7, pp. 526–529, 2013.

[35] B. Arons, "A Review of The Cocktail Party Effect," *J. Am. Voice I/O Soc.*, vol. 12, pp. 35–50, 1992.

[36] S. Ranganathan, "Alloyed pleasures: Multimetallic cocktails," *Curr. Sci.*, vol. 85, no. 10, pp. 1404–1406, 2003.

[37] M. R. Chen, S. J. Lin, J. W. Yeh, S. K. Chen, Y. S. Huang, and M. H. Chuang, "Effect of vanadium addition on the microstructure, hardness, and wear resistance of $Al_{0.5}$CoCrCuFeNi high-entropy alloy," *Metall. Mater. Trans. A Phys. Metall. Mater. Sci.*, vol. 37, no. 5, pp. 1363–1369, 2006.

[38] P.-K. Huang, J.-W. Yeh, T.-T. Shun, and S.-K. Chen, "Multi-Principal-Element Alloys with Improved Oxidation and Wear Resistance for Thermal Spray Coating," *Adv. Eng. Mater.*, vol. 6, no. 12, pp. 74–78, 2004.

[39] J. Yeh, S. Chen, J. Gan, S. Lin, and T. Chin, "Communications: Formation of Simple Crystal Structures in Cu-Co-Ni-Cr-Al-Fe-Ti-V Alloys with Multiprincipal Metallic Elements," vol. 35, no. August 2004, pp. 2533–2536, 2010.

[40] W. Hume-Rothery, “Factors affecting the stability of metallic phases, ” In: P. S. Rudman, J. Stringer and R. I. Jaffee, (Eds.), Phase Stability in Metals and Alloys, *New York: McGraw-Hill,* pp. 3-23, 1967.

[41] J. Smith, W.F., Hashemi, and F.P Moreno, “ Foundation of Materials Science and Engineering,” *Mcgraw-Hill Publishing*, pp. 310-313, 2006.

[42] Y. Zhang, Y. J. Zhou, J. P. Lin, G. L. Chen, and P. K. Liaw, “Solid-solution phase formation rules for multi-component alloys,” *Adv. Eng. Mater.*, vol. 10, no. 6, pp. 534–538, 2008.

[43] and F. R. D. B. Miedema, A. R., P. F. De Chatel, “Cohesion in alloys—fundamentals of a semi-empirical model.,” *Phys. B+ c*, vol. 100, no. 1, pp. 1–28, 1980.

[44] Y. Zhang *et al.*, “Guidelines in predicting phase formation of high-entropy alloys,” *MRS Commun.*, vol. 4, no. 2, pp. 57–62, 2014.

[45] S. Guo, Q. Hu, C. Ng, and C. T. Liu, “More than entropy in high-entropy alloys: Forming solid solutions or amorphous phase,” *Intermetallics*, vol. 41, pp. 96–103, 2013.

[46] S. Guo and C. T. Liu, “Phase stability in high entropy alloys: Formation of solid-solution phase or amorphous phase,” *Prog. Nat. Sci. Mater. Int.*, vol. 21, no. 6, pp. 433–446, 2011.

[47] M. H. Chuang, M. H. Tsai, W. R. Wang, S. J. Lin, and J. W. Yeh, “Microstructure and wear behavior of $Al_xCo_{1.5}CrFeNi_{1.5}Ti_y$ high-entropy alloys,” *Acta Mater.*, vol. 59, no. 16, pp. 6308–6317, 2011.

[48] M. H. Tsai *et al.*, “Significant hardening due to the formation of a sigma phase matrix in a high entropy alloy,” *Intermetallics*, vol. 33, pp. 81–86, 2013.

[49] S. T. Chen *et al.*, “Microstructure and properties of age-hardenable $Al_xCrFe_{1.5}MnNi_{0.5}$ alloys,” *Mater. Sci. Eng. A*, vol. 527, no. 21–22, pp. 5818–5825, 2010.

[50] C. Hsu, J. Yeh, S. Chen, and T. Shun, “Wear Resistance and High-Temperature Compression Strength of Fcc CuCoNiCrAl alloy with boron addition” *Metall. Mater. Transcations A*, vol. 35A, no. May, pp. 1465–1469, 2004.

[51] S. Guo, C. Ng, J. Lu, and C. T. Liu, “Effect of valence electron concentration on stability of fcc or bcc phase in high entropy alloys,” *J. Appl. Phys.*, vol. 109, no. 10, 2011.

[52] B. Ren, Z. X. Liu, D. M. Li, L. Shi, B. Cai, and M. X. Wang, “Effect of elemental interaction on microstructure of CuCrFeNiMn high entropy alloy system,” *J. Alloys Compd.*, vol. 493, no. 1–2, pp. 148–153, 2010.

[53] L. H. Wen, H. C. Kou, J. S. Li, H. Chang, X. Y. Xue, and L. Zhou, “Effect of aging temperature on microstructure and properties of AlCoCrCuFeNi high-entropy alloy,” *Intermetallics*, vol. 17, no. 4, pp. 266–269, 2009.

[54] P. Hohenberg and W. Kohn, “Gas, Inhomogeneous Electron,” *Phys. Rev. B*, vol. 136, no. 864, 1964.

[55] K. C. Hass and W. F. Schneider, “First-principles molecular dynamics simulations of H_2O on α-Al2O3 (0001),” *J. Phys. Chem. B*, vol. 104, no. 23, pp. 5527–5540, 2000.

[56] G. Kresse, “Ab initio molecular dynamics for liquid metals,” *J. Non. Cryst. Solids*, vol. 192–193, pp. 222–229, 1995.

[57] L. Calderín, D. J. González, L. E. González, and J. M. López, “Structural, dynamic, and electronic properties of liquid tin: An ab initio molecular dynamics study,” *J. Chem. Phys.*, vol. 129, no. 19, 2008.

[58] J. P. Perdew, K. Burke, and M. Ernzerhof, “Generalized gradient approximation made simple,” *Phys. Rev. Lett.*, vol. 77, no. 18, pp. 3865–3868, 1996.

[59] M. Gao and D. Alman, “Searching for Next Single-Phase High-Entropy Alloy

Compositions," *Entropy*, vol. 15, no. 12, pp. 4504–4519, 2013.

[60] C. Zhang, F. Zhang, S. Chen, and W. Cao, "Computational thermodynamics aided high-entropy alloy design," *Jom*, vol. 64, no. 7, pp. 839–845, 2012.

[61] L. Vitos, I. A. Abrikosov, and B. Johansson, "Anisotropic lattice distortions in random alloys from first-principles theory," *Phys. Rev. Lett.*, vol. 87, no. 15, pp. 156401-156401–4, 2001.

[62] M. Calvo-Dahlborg *et al.*, "Interplay of electronic, structural and magnetic properties as the driving feature of high-entropy CoCrFeNiPd alloys," *J. Phys. D. Appl. Phys.*, vol. 50, no. 18, 2017.

[63] S. Singh, N. Wanderka, B. S. Murty, U. Glatzel, and J. Banhart, "Decomposition in multi-component AlCoCrCuFeNi high-entropy alloy," *Acta Mater.*, vol. 59, no. 1, pp. 182–190, 2011.

[64] C. Suryanarayana, "Mechanical alloying and milling," *Prog. Mater. Sci.*, vol. 46, no. 1–2, pp. 1–184, 2001.

[65] S.Y. Chang et al. "Mechanical properties, deformation behaviors and interface adhesion of (AlCrTaTiZr)Nx multi-component coatings," *Surface and Coatings Technology*, vol. 204, no. 20, pp. 3307-3314, 2010.

[66] C. W. Tsai, M. H. Tsai, J. W. Yeh, and C. C. Yang, "Effect of temperature on mechanical properties of $Al_{0.5}$CoCrCuFeNi wrought alloy," *J. Alloys Compd.*, vol. 490, no. 1–2, pp. 160–165, 2010.

[67] C. Y. Hsu, W. R. Wang, W. Y. Tang, S. K. Chen, and J. W. Yeh, "Microstructure and mechanical properties of new $AlCo_xCrFeMo_{0.5}Ni$ high-entropy alloys," *Adv. Eng. Mater.*, vol. 12, no. 1–2, pp. 44–49, 2010.

[68] J. I. Hyun, K. H. Kong, K. C. Kim, W. T. Kim, and D. H. Kim, "Microstructural Evolution in CuCrFeNi, CuCrFeNiMn, and CuCrFeNiMnAl High Entropy Alloys," *Appl. Microsc.*, vol. 45, no. 1, pp. 9–15, 2015.

[69] Lihl, F., and H. Ebel. "WB Pearson, a Handbook of lattice spacings and structures of metals and alloys." (1967).

[70] Y. F. Kao, T. J. Chen, S. K. Chen, and J. W. Yeh, “Microstructure and mechanical property of as-cast, -homogenized, and -deformed $Al_xCoCrFeNi$ ($0 \leq x \leq 2$) high-entropy alloys,” *J. Alloys Compd.*, vol. 488, no. 1, pp. 57–64, 2009.

[71] C.J. Tong et al. "Microstructure characterization of $Al_xCoCrCuFeNi$ high-entropy alloy system with multiprincipal elements." *Metallurgical and Materials Transactions A*, vol. 36, no. 4, pp. 881-893, 2005.

[72] S. Guo, C. Ng, J. Lu, and C. T. Liu, “Effect of valence electron concentration on stability of fcc or bcc phase in high entropy alloys,” Journal of Applied Physics, vol. 109, no. 10, 2011.

[73] Y.J. Hsu, W.C. Chiang, and J.K. Wu, "Corrosion behavior of $FeCoNiCrCu_x$ high-entropy alloys in 3.5% sodium chloride solution," *Materials Chemistry and Physics*, vol. 92, no. 1, pp. 112-117, 2005.

[74] Zhang, S-L., and Z. Zhang. "Metal silicides in advanced complementary metal-oxide-semiconductor (CMOS) technology," *Metallic Films for Electronic, Optical and Magnetic Applications*, pp 244-301, 2014.

[75] A. Takeuchi, and A. Inoue, "Calculations of mixing enthalpy and mismatch entropy for ternary amorphous alloys," *Materials transactions*, vol. 41, no. 11, pp. 1372-1378, 2000.

[76] S.R. Shatynski, "The thermochemistry of transition metal carbides," *Oxidation of Metals*, vol. 13, no. 2, pp. 105-118, 1979.

[77] S. Gorsse, D. B. Miracle, and O. N. Senkov, “Mapping the world of complex concentrated alloys,” Acta Materialia, vol. 135, pp. 177–187, 2017.

[78] Alfa Easer by Thermo Fisher Scientific Adopted January 10, 2020 from https://www.alfa.com/en/

[79] A.Dehghanghadikolaei et al., "Additive manufacturing methods: a brief overview," *J. Sci. Eng. Res* 5, pp. 123-131, 2018.

[80] M. Agarwala et al., "Direct selective laser sintering of metals," *Rapid Prototyping Journal,* vol. 1, no. 1, pp. 26-36, 1995.

[81] B. Yevgeni, M. Thomas, and I. Todd. "The use of high-entropy alloys in additive manufacturing," *Scripta Materialia*, vol. 99, pp. 93-96, 2015.

APPENDICES

A. Software for Calculation of Thermodynamic properties of HEAs

Python based software is developed by Res. Assist. Doğuhan Sarıtürk to calculate thermodynamic data of the selected HEAs. The citation details and doi number of the software as given below:

Doğuhan Sarıtürk. (2019, December 20). HEACalculator (Version v.0.1-alpha).

Zenodo. http://doi.org/10.5281/zenodo.3590319